

# Investigation of 2D Materials using Low Energy Electron Microscopy (LEEM)

Hao Yin

Information

Band / Volume 115

ISBN 978-3-95806-848-3







Forschungszentrum Jülich GmbH  
Peter Grünberg Institut (PGI)  
Quantum Nanoscience (PGI-3)

# **Investigation of 2D Materials using Low Energy Electron Microscopy (LEEM)**

Hao Yin

Schriften des Forschungszentrums Jülich  
Reihe Information / Information

Band / Volume 115

ISSN 1866-1777

ISBN 978-3-95806-848-3

Bibliografische Information der Deutschen Nationalbibliothek.  
Die Deutsche Nationalbibliothek verzeichnet diese Publikation in der  
Deutschen Nationalbibliografie; detaillierte Bibliografische Daten  
sind im Internet über <http://dnb.d-nb.de> abrufbar.

Herausgeber  
und Vertrieb:           Forschungszentrum Jülich GmbH  
                                Zentralbibliothek, Verlag  
                                52425 Jülich  
                                Tel.: +49 2461 61-5368  
                                Fax: +49 2461 61-6103  
                                **zb-publikation@fz-juelich.de**  
                                **[www.fz-juelich.de/zb](http://www.fz-juelich.de/zb)**

Umschlaggestaltung:   Grafische Medien, Forschungszentrum Jülich GmbH

Druck:                    Grafische Medien, Forschungszentrum Jülich GmbH

Copyright:             Forschungszentrum Jülich 2025

Schriften des Forschungszentrums Jülich  
Reihe Information / Information, Band / Volume 115

D 82 (Diss. RWTH Aachen University, 2025)

ISSN 1866-1777  
ISBN 978-3-95806-848-3

Vollständig frei verfügbar über das Publikationsportal des Forschungszentrums Jülich (JuSER)  
unter [www.fz-juelich.de/zb/openaccess](http://www.fz-juelich.de/zb/openaccess).



This is an Open Access publication distributed under the terms of the [Creative Commons Attribution License 4.0](https://creativecommons.org/licenses/by/4.0/),  
which permits unrestricted use, distribution, and reproduction in any medium, provided the original work is properly cited.

## Eidesstattliche Erklärung

### Declaration of Authorship

I, Hao Yin

declare that this thesis and the work presented in it are my own and has been generated by me as the result of my own original research.

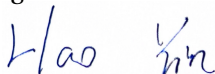
Hiermit erkläre ich an Eides statt / I do solemnly swear that:

1. This work was done wholly or mainly while in candidature for the doctoral degree at this faculty and university;
2. Where any part of this thesis has previously been submitted for a degree or any other qualification at this university or any other institution, this has been clearly stated;
3. Where I have consulted the published work of others or myself, this is always clearly attributed;
4. Where I have quoted from the work of others or myself, the source is always given. This thesis is entirely my own work, with the exception of such quotations;
5. I have acknowledged all major sources of assistance;
6. Where the thesis is based on work done by myself jointly with others, I have made clear exactly what was done by others and what I have contributed myself;
7. Parts of this work have been published, as the listed reference below  
H. Yin, M. Hutter, C. Wagner, F. S. Tautz, F. C. Bocquet, and C. Kumpf, "Epitaxial growth of mono- and (twisted) multilayer graphene on SiC(0001)", link:  
<https://doi.org/10.1103/PhysRevMaterials.9.044003>.

date

*July 10, 2025*

signature





# Abstract

Low-energy electron microscopy (LEEM) is a versatile and powerful surface science tool for imaging, structural analysis and the study of kinetic surface processes such as molecular island growth, thin film growth and surface reconstruction. It uses electrons with kinetic energies below a few hundred electronvolts, often below 10 eV. In this thesis, LEEM serves as the main technique to support our research efforts in fabricating 30°-twisted bilayer graphene (TBG) and in studying the deposition and degradation behavior of a cyclic, tire-shaped molecules on a metal crystal.

The first two topics of this thesis build on previous work from our group that demonstrated the epitaxial growth of unconventionally oriented monolayer graphene on a 6H-SiC(0001) substrate. In the first topic, LEEM and other investigation methods were used to characterize the morphology and electronic properties of such unconventionally oriented monolayer graphene. The effect of the preparation temperature on the resulting graphene sample was highlighted. In the second topic, we achieved and studied bilayer stacking and twist configurations of graphene by hydrogen intercalation of the carbon buffer layer, an intrinsic component between the epitaxial graphene and the SiC substrate. Hydrogen atoms were successfully introduced to decouple the buffer layer from the substrate. The buffer layer was transformed into a true graphene layer with distinct  $\pi$ -band properties. This intercalation process was carried out in a step-wise manner, with LEEM being used to study each step. The deintercalation process was monitored in situ and in real time. This provided deeper insights into the mechanisms of hydrogen intercalation and deintercalation.

In the third topic of the thesis, the deposition behavior of a carbon-based cyclic aromatic molecule, [6]-cycloparaphenylenes, is investigated using LEEM in addition to pristine 2D graphene layers. Interestingly, our observations contradict



## **Abstract**

---

previous results obtained by scanning tunneling microscopy. This provides new insights into the deposition behavior of this type of molecules on surfaces.

## Zusammenfassung

Die niederenergetische Elektronenmikroskopie (LEEM), die Elektronen mit kinetischen Energien unter einigen hundert Elektronenvolt, oft sogar unter 10 eV, verwendet, ist ein vielseitiges und leistungsfähiges Werkzeug der Oberflächenwissenschaft für Bildgebung, Strukturanalyse und das Studium dynamischer Oberflächenprozesse wie dem Wachstum von Molekülinseln, dünnen Filmen und Oberflächenrekonstruktionen. In dieser Arbeit dient LEEM als Hauptmethode für unsere Forschungsbemühungen zur Herstellung von 30°-verdrehtem zweilagigem Graphen (TBG) sowie zur Untersuchung des Adsorptions- und Desorptionsverhaltens eines zyklischen, reifenförmigen Moleküls auf einem Metallkristall.

Die ersten beiden Themen dieser Arbeit bauen auf früheren Arbeiten unserer Gruppe auf, die das epitaktische Wachstum von unkonventionell orientiertem Monolagen-Graphen auf einem 6H-SiC(0001)-Substrat demonstrieren. Im ersten Thema wurden LEEM und andere Untersuchungsmethoden eingesetzt, um die Morphologie und die elektronischen Eigenschaften dieses unkonventionell orientierten Monolagen-Graphens zu charakterisieren, wobei der Einfluss der Herstellungstemperatur auf die resultierende Graphenprobe hervorgehoben wird.

Im zweiten Thema haben wir die Herstellung von zweilagigem Graphen durch Wasserstoffinterkalation unter der Kohlenstoffpufferschicht, einer intrinsischen Komponente zwischen dem epitaktischen Graphen und dem SiC-Substrat, erreicht und untersucht. Wasserstoffatome wurden erfolgreich interkaliert, um die Pufferschicht vom Substrat zu entkoppeln und sie in eine echte Graphenschicht mit charakteristischen  $\pi$ -Band-Eigenschaften zu verwandeln, was zusammen mit der darüber liegenden ersten Graphen Lage zu einem (verdrehen) Bilagensystem führt. Dieser Interkalationsprozess wurde schrittweise durchgeführt,

## **Zusammenfassung**

---

wobei jede Stufe mit LEEM untersucht wurde. Der Deinterkalationsprozess wurde ebenfalls in Echtzeit überwacht, was tiefere Einblicke in die Mechanismen der Wasserstoff-Interkalation und -Deinterkalation ermöglichte.

Zusätzlich zu reinen zweidimensionalen Graphenschichten untersucht das dritte Thema der Dissertation das Ablagerungsverhalten eines kohlenstoffbasierten, zyklischen, aromatischen Moleküls, [6]-Cycloparaphenylene, unter Verwendung von LEEM. Interessanterweise widersprachen unsere Beobachtungen früheren Ergebnissen, die mit der Rastertunnelmikroskopie gewonnen wurden, und lieferten neue Einblicke in das Ablagerungsverhalten von Molekülen auf Oberflächen.

## List of Acronyms

**AC-SPELEEM** Aberration-Corrected Spectroscopic Photoemission and Low-Energy Electron Microscopy

**ARPES** Angle-Resolved Photo Emission Spectroscopy

**BF-LEEM** Bright Field Low Energy Electron Microscopy

**BPRs** Biphenylene Ribbons

**CNTs** Carbon Nanotubes

**CVD** Chemical Vapor Deposition

**DF-LEEM** Dark Field Low Energy Electron Microscopy

**EMLG** Epitaxial Monolayer Graphene

**FoV** Field of View

**h-BN** Hexagonal Boron Nitride

**HOMO** The Highest Occupied Molecule Orbital

**LEED** Low Energy Electron Diffraction

**LEEM** Low Energy Electron Microscopy

**LUMO** The Lowest Unoccupied Molecule Orbital

**LPPs** Linear Oligoparaphenylenes

**MEM** Mirror Electron Microscopy

## List of Acronyms

---

***n*-CPPs** [*n*]-Cycloparaphenylenes

**PASG** Polymer Assisted Sublimation Growth

**PPP** Polyparaphenylene

**PT** Photoemission Tomography

**PTCDA** 3,4,9,10-Perylene Tetracarboxylic Dianhydride

**QFMLG** Quasi-freestanding monolayer graphene

**RT** Room Temperature

**SERS** Surface-enhanced Raman Spectroscopy

**SPA-LEED** Spot Profile Analysis of Low Energy Electron Diffraction

**SPLEEM** Spin Polarized Low Energy Electron Microscopy

**SPM** Scanning Probe Microscopy

**STM** Scanning Tunneling Microscopy

**TBG** Twisted Bilayer Graphene

**TEEM** Thermoionic Emission Electron Microscopy

**THF** Tetrahydrofuran

**THz** Terahertz

**TMDCs** Transition Metal Dichalcogenides

**XPEEM** X-ray Photoemission Electron Microscopy

**XPS** X-ray Photoelectron Spectroscopy

**XRD** X-ray Diffraction

**ZLG** Zeroth-Layer Graphene

# Contents

<b>Abstract (English/Deutsch)</b>	<b>i</b>
<b>List of Acronyms</b>	<b>v</b>
<b>Introduction</b>	<b>1</b>
<b>1 Theoretical Background</b>	<b>5</b>
1.1 Epitaxial Graphene on SiC . . . . .	5
1.2 Hydrogen Intercalation of Epitaxial Graphene . . . . .	11
1.3 Twisted Bilayer Graphene (TBG) . . . . .	13
1.4 Cycloparaphenylenes (CPPs) . . . . .	18
<b>2 Experimental Techniques</b>	<b>23</b>
2.1 Introduction to LEEM . . . . .	23
2.1.1 Experimental Setup . . . . .	23
2.1.2 Contrast mechanisms in LEEM imaging . . . . .	28
2.1.3 Bright Field and Dark Field LEEM . . . . .	29
2.1.4 LEEM- <i>IV</i> Measurements . . . . .	29
2.1.5 Clustering Algorithm <i>K-means</i> . . . . .	32
2.2 LEED . . . . .	34
2.3 PEEM . . . . .	37
<b>3 0°-Rotated Monolayer Epitaxial Graphene</b>	<b>39</b>
3.1 Sample Preparation . . . . .	40
3.2 Homogeneity and Electronic Structure . . . . .	41
3.3 Surface Morphology of the low-T sample . . . . .	44
3.4 Surface Morphology of the high-T sample . . . . .	52
	vii



## Contents

---

3.5 Conclusion . . . . .	61
<b>4 30°-TBG via Hydrogen Intercalation</b>	<b>63</b>
4.1 Sample Preparation . . . . .	64
4.2 Pristine Surface before Intercalation . . . . .	64
4.3 Intercalation of the Layers in Three Steps . . . . .	66
4.4 Deintercalation of 30°-TBG . . . . .	73
4.5 Conclusion . . . . .	79
<b>5 [6]-CPP on Cu(111)</b>	<b>81</b>
5.1 Deposition . . . . .	81
5.2 Warming-up to RT (25 °C) . . . . .	84
5.3 Annealing to 180°C . . . . .	90
5.4 Summary . . . . .	96
<b>6 Summary and Outlook</b>	<b>99</b>
<b>A <i>K-means</i> Codes for the Pixel-by-Pixel Analysis</b>	<b>105</b>
 <b>Bibliography</b>	 <b>124</b>
<b>List of Figures</b>	<b>125</b>
<b>Acknowledgements</b>	<b>135</b>
<b>Curriculum Vitae</b>	<b>137</b>

# Introduction

The term "interfaces" in the context of physical science refers to the structures and dynamics present at the boundary between two phases, which together form a heterogeneous system. The importance of interfaces in a number of practical fields cannot be overstated, including but not limited to those of applied nanotechnology, semiconductor fabrication, nano-structure self-assembly, fuel cells, and catalysis. Another closely related concept that frequently arises in this context is that of two-dimensional (2D) materials, namely crystalline solids comprising a single or few atomic layers. Due to the distinctive anisotropy exhibited in their optical and charge-transport characteristics, these compounds offer considerable promise for the next generation of electronic devices, especially as active electroluminescent materials and transistor interlayers. The family of two-dimensional (2D) materials has undergone significant expansion over two decades of research. Prominent examples of 2D materials include graphene, hexagonal boron nitride (h-BN), and transition metal dichalcogenides (TMDCs).

The development of novel characterization techniques is a key factor in the advancement of knowledge in the field of surface science and two-dimensional materials. Investigations typically encompass a range of subjects, including surface reconstructions, epitaxy, electronic states, phonons and plasmons, spintronics, tunneling phenomena, and other related topics. A variety of experimental techniques have been developed for the purpose of exploring these properties. Among the most frequently employed techniques are angle-resolved photoemission spectroscopy (ARPES), photoelectron tomography (PT), x-ray photoelectron spectroscopy (XPS), scanning probe microscopy (SPM), low-energy electron diffraction (LEED), (surface) x-ray diffraction (XRD/SXRD), electron

## Introduction

---

microscopy, and surface-enhanced Raman spectroscopy (SERS).

In this study, we employ a LEED-based technique—namely, low-energy electron microscopy (LEEM)—for exploring the morphology, structure, and kinetics of surfaces. LEEM operates by employing low-energetic electrons that penetrate a surface to a depth of only a few atomic layers. This results in the acquisition of exclusively two-dimensional information. LEEM images are formed by electrons that undergo elastic backscattering on surfaces, namely interactions that do not result in energy loss. The wavelength of the low-energy electrons is on the order of a few Å, which is comparable to the typical atomic separation in solids. Consequently, when these electrons interact with a crystalline surface, they undergo diffraction effects whereby the relatively strong diffraction cross section between electrons and matter result in a high surface sensitivity. Furthermore, the method is in most cases non-destructive, which is particularly beneficial for studying fragile systems such as organic molecules on surfaces. Moreover, LEEM offers a unique opportunity to observe surfaces over vast temporal and spatial scales. This is enabled by the high reflectivity of low-energy electrons and by the full-field imaging capability. Another important advantage of the technique is the ability to conduct in-situ observations in real time, which is of great significance for surface kinetics studies, as e.g. the growth of islands or layers, the formation or transition of phases, etc..

The development of the LEEM technique involved the contributions of numerous pioneers over a period of approximately six decades, beginning with the initial implementation of classic electron diffraction experiments by Davisson and Germer [7]. Ernst Bauer, who rejected the prevailing notion that the resolution limit was a consequence of chromatic aberration in the objective lens, published the first compelling LEEM image in 1985 together with Teliëps [8]. He was pioneering the development of the technology and its applications. The LEEM instrument in our laboratory was provided by Elmitec Elektronenmikroskopie GmbH, a company founded by Bauer in 1995, which is currently the foremost producer of LEEM and PEEM systems worldwide. Over time, LEEM has undergone significant advancements, leading to the emergence of its fifth generation. These developments include the introduction of novel techniques such as spin-polarized LEEM (SPLEEM), x-ray photoemission electron microscopy

(XPEEM), thermionic emission electron microscopy (TEEM), and mirror electron microscopy (MEM), among others. Another important step forward was the development of an aberration corrector for the LEEM instrument, which was pushed by Bauer and others, and improved the resolution of the technique by almost one order of magnitude, to values below 2nm.

A category of techniques closely related to LEEM encompasses those that may be performed using a low-energy electron microscope. The oldest of these techniques is low-energy electron diffraction (LEED), which provides supplementary data regarding reciprocal space. Furthermore, LEEM's full-field imaging capability enables variations, such as photoemission electron microscopy (PEEM), where photoemitted electrons are used for imaging instead of reflected electrons. These complementary methods facilitate structural investigations of surfaces and two-dimensional materials, enabling observations of phenomena such as phase transitions, thin film growth, etching, adsorption, reactions, segregation, sublimation, and strain relief. In recent years, numerous studies employing LEEM have been published by our group. These studies have included in-situ investigations of the (co-) adsorption of diverse molecules on metals [9–11], as well as on molecule-graphene hybrid systems [12]. The topic of two-dimensional (2D) materials has also been the subject of our numerous studies. The dendritic growth of h-BN on Cu(111) was the subject of an investigation reported in Ref. [13]. The domain structure and adsorption sites of h-BN on Ni(111) were topics in Ref. [14], and the growth behavior on Cu(110) was investigated in Ref. [15].

In this work, we will discuss several topics with LEEM being the primary characterization method. These include the morphology of unconventionally oriented epitaxial graphene on SiC, twisted bilayer graphene achieved via hydrogen intercalation, and the deposition behavior of a carbon-based aromatic molecule on a Cu crystal. The two graphene-related chapters make intensive use of the LEEM-*IV* technique. LEEM-*IV* allows to determine the number of decoupled graphene layers on the substrate. This layer counting is an important aspect in analyzing the bilayer and multilayer growth of graphene. We apply this technique with highest spatial resolution, by analyzing the LEEM images pixel-by-pixel. The initial chapter will furnish background information and recent developments

## **Introduction**

---

pertaining to these three topics. Subsequently, an overview of the technical specifications of our LEEM apparatus and related techniques will be provided. In the final analysis, each of the three research topics will be discussed in detail in chapters 3 to 5.

# 1 Theoretical Background

In this work, we will explore three topics studied using the LEEM technique: unconventional oriented ( $0^\circ$ -rotated) epitaxial graphene,  $30^\circ$ -twisted bilayer graphene (TBG) formed through hydrogen intercalation, and [6]-Cycloparaphenylene (CPP) on Cu(111). This chapter provides essential background information, including the current state of research and the theoretical foundations related to these topics.

Fullerenes, carbon nanotubes, carbon-based supramolecules and other advanced nanomaterials all share a common foundation: they are derived from the unique structural architecture of their core component, which is the planar (flat) graphene layer with its hexagonal honeycomb structure [16–18]. These  $\pi$ -conjugated systems exhibit remarkable electronic, mechanical, and chemical properties, but their inherent characteristics ultimately trace back to the pristine graphene sheets. In the first two sections, we will discuss the preparation, properties, and tunability of the 2D material "graphene" in its various forms, such as monolayer, bilayer, and intriguing twisted bilayer configurations.

## 1.1 Epitaxial Graphene on SiC

Graphene, a single layer of graphite, is composed solely of carbon atoms arranged in a honeycomb pattern, offering exceptional structural stability. When Geim and Novoselov published their groundbreaking work on exfoliated graphene



## Chapter 1. Theoretical Background

---

sheets in 2004 [19], they inaugurated a new research field that has been rapidly and continuously expanding ever since. Even before graphene was actually realized, numerous hypothetical predictions about the material had been proposed. Graphene is a prime candidate for advanced applications due to its remarkable electrical, optical, mechanical, and thermal properties [20–26]. In a single layer of graphene, each carbon atom forms bonds with three neighboring carbon atoms through  $sp^2$  hybridization. Its exceptional electronic properties stem from its unique band structure, characterized by linear dispersion near the Dirac points [21, 25, 27–29].

Various methods for producing graphene have been developed, including micro-mechanical exfoliation, chemical vapor deposition (CVD), carbon segregation from bulk metal [30, 31], and epitaxial growth on various polytypes of SiC. Each of these methods yields graphene with distinct structural and electronic properties. Micro-mechanical exfoliation, first demonstrated by Novoselov *et al.* in 2004 [19], produces graphene flakes of limited sub-millimeter size, making it hard to be competent for large-scale industrial applications. This is different when graphene is grown epitaxially by CVD on substrates such as Ir, Cu, Ni, or cold wall systems [32–35]. The properties of the resulting graphene layer are significantly affected by various growth conditions, including preparation temperatures, catalytic substrates, pressures, etc..

The thermal decomposition of hexagonal polytypes of SiC is an effective method for producing large-scale, high-quality graphene films, suitable for electronic and circuit applications. This epitaxial growth process relies on the thermal decomposition of the SiC substrate at a temperature around 1250 °C, at which the silicon atoms have much higher mobility than that of carbon, therefore, silicon atoms preferentially sublime from the surface of the SiC, leaving behind carbon atoms that form graphene layers [36]. A remarkable advantage of this method is that the graphene growth process is catalyst-free, resulting in carbon-based structures, such as epitaxial graphene and carbon nanotubes, that are of high purity and uniformity. However, the epitaxial growth of graphene layers on the SiC surface in the vacuum is not a self-limiting process, which means that the growth rates on different areas are different resulting in domains with a different number of graphene layers. To achieve wafer-scale graphene

layers with uniform thickness through controlled thermal decomposition, Virojanadara *et al.* first introduced the annealing of the 6H-SiC(0001) surface in an argon atmosphere at 1 atm and 2000 °C [28]. The argon environment significantly reduces the sublimation rate of silicon atoms at a high temperature, which are scattered back to the surface by the collision with Ar atoms, allowing for precise control over the thickness of the graphene films [37, 38]. For further improvement of the quality and homogeneity of epitaxial graphene layers on SiC, a technique, so-called polymer-assisted sublimation growth (PASG), is proposed, thereby the sublimation process is enhanced by the use of a pre-deposited polymer adsorbate on the SiC substrate, serving as an additional carbon source, which effectively mitigates step bunching on the substrate [39–41]. Even on SiC substrates with high miscuts, high-quality graphene can be achieved when the appropriate polymer concentration is applied [42].

The standard process for growing epitaxial graphene layers on a SiC substrate typically begins with a  $(3 \times 3)$  Si-rich reconstruction. This step is crucial because the atomic arrangement of the SiC surface has a direct impact on the subsequent growth of the heterostructure and the performance of SiC-based electronic devices. Extensive research concerning on the preparation of stable surfaces has been conducted for SiC. On an unreconstructed (Si-terminated) SiC surface, each Si atom has one dangling bond. To achieve surface stability, it is necessary to reduce the number of dangling bonds, which can be accomplished by saturating the surface with foreign adatoms or by altering the compositional Si:C ratio. Both approaches typically result in surface reconstructions [43].

Annealing the Si-rich  $(3 \times 3)$  reconstructed 6H-SiC(0001) surface in vacuum at 1000 °C leads to the evaporation of Si atoms and hence to the formation of a  $(\sqrt{3} \times \sqrt{3}) R30^\circ$  reconstruction consisting of  $1/3$  of a monolayer of Si adatoms on the substrate [44]. Fig. 1.1 displays two LEED patterns obtained from a Si-rich 6H-SiC(0001) surface with  $(3 \times 3)$  and  $(\sqrt{3} \times \sqrt{3}) R30^\circ$  reconstructions, which are measured at 100 eV. The diffraction spots of the substrate are marked by red circles.

When annealing is continued at temperatures above 1100 °C, a  $(6\sqrt{3} \times 6\sqrt{3}) R30^\circ$  reconstructed carbon layer begins to form, covering the SiC surface. This layer,

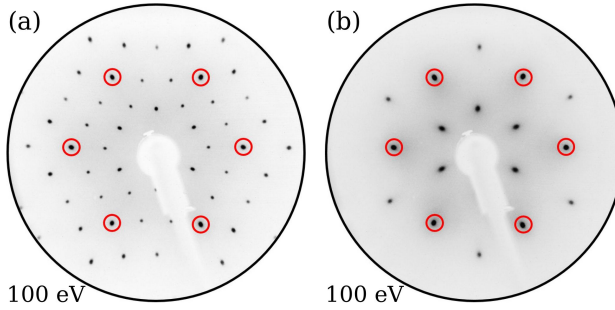


Figure 1.1: LEED patterns obtained from a 6H-SiC(0001) surface with Si-rich (a)  $(3 \times 3)$  and (b)  $(\sqrt{3} \times \sqrt{3}) R30^\circ$  reconstruction. The LEED energy is 100 eV, and the diffraction spots of the substrate are marked by red circles.

known as "zeroth-layer graphene" (ZLG- $R30^\circ$ ) or the "buffer layer", emerges due to the difference in lattice parameters between graphene ( $2.46 \text{ \AA}$ ) and the 6H-SiC(0001) substrate ( $3.08 \text{ \AA}$ ) [1].

A schematic representation of the  $(6\sqrt{3} \times 6\sqrt{3}) R30^\circ$  reconstruction in carbon buffer layer (ZLG) on 6H-SiC(0001) is given as STM-resolved atomic arrangement in Fig. 1.2 (a) with a tunneling voltage of 0.2 V [1]. The colored dots represent the resolvable charge densities, which are considered to represent atomic positions. The red colored dots depict the clearest contrast with four dots in one group, and are arranged in a diamond shape. They are repeated only with  $(6\sqrt{3} \times 6\sqrt{3}) R30^\circ$  periodicity. The  $(6\sqrt{3} \times 6\sqrt{3}) R30^\circ$  grid can be easily identified with an unit cell indicated by blue solid lines, which has a side length of  $32 \text{ \AA}$  as indicated in the panel [1]. It needs to be noted that this sketch does not represent the complete atomic structure which is still unresolved nowadays, and the  $(6 \times 6)$  grid of charge densities can not be resolved at such a small bias voltage, which is possible at higher voltages of over 1.7 V. The green dashed lines mark an unit cell of the  $(6 \times 6)$  grid, though some positions of charge density are invisible in Fig. 1.2 (a).

The measured LEED pattern of an epitaxial ZLG- $R30^\circ$  sample is depicted in Fig. 1.2 (b), in which the unit cell vectors of the substrate SiC and epitaxial graphene are indicted by black and red colored arrows, respectively. At this stage, real epitaxial graphene layer is not present on the surface since the ZLG still has

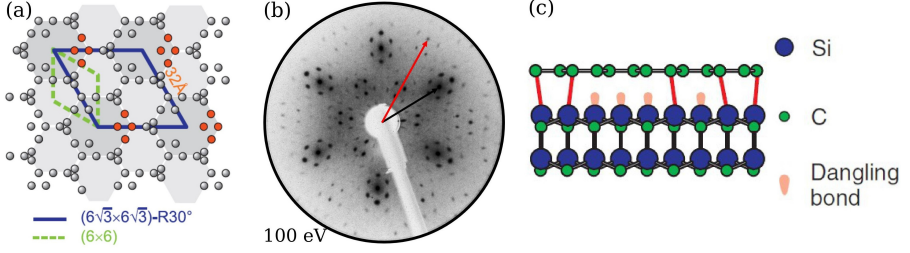


Figure 1.2: (a) Schematic representation of the atomic arrangement in a carbon buffer layer (ZLG) on a 6H-SiC(0001) surface, adapted from an STM image with a bias voltage of 0.2 V [1]. The colored dots represent resolvable charge densities, which are considered to represent the atomic positions. The red dots that arrange in a diamond shape mark the clearest contrast, and are repeated only with  $(6\sqrt{3} \times 6\sqrt{3})$  R30° periodicity. (b) Measured LEED pattern from a ZLG graphene sample. The LEED energy is 100 eV. The unit cell vectors of the substrate SiC and epitaxial graphene are marked by black and red colored arrows, respectively. (c) Sketched side view model of the  $(6\sqrt{3} \times 6\sqrt{3})$  R30° reconstructed ZLG [2].

covalent bonds to the substrate. Hence, the intensity of diffraction spot marked by the red arrow remains relatively weak. The six strong spots surrounding each substrate spots belong to the  $(6 \times 6)$  grid, which originates from a nanomesh with a quasi-honeycomb structure [29]. Other visible spots with low intensity in panel (b) are located on the  $6\sqrt{3}$  grid. As the formation of graphene proceeds, the intensity of these spots will diminish and eventually disappear, while the intensity of the graphene spots will increase. Fig. 1.2 (c) shows a sketched side view model of the  $(6\sqrt{3} \times 6\sqrt{3})$  R30°-reconstructed ZLG [2]. The ZLG consists of only carbon atoms arranged in a honeycomb structure similar to graphene. However, it is not considered a true "graphene layer" because approximately 30% of these carbon atoms remain covalently bonded to the underlying Si atoms of the substrate. This bonding inhibits the formation of  $\pi$  bands with linear dispersion within the layer [2].

By further increasing the annealing temperature to around 1300 °C, a "new ZLG" grows just below the "current ZLG", and pushes the "current ZLG" up to form a complete graphene layer with a 30° rotation with respect to the substrate lattice [29]. Fig. 1.3 presents the measured (a) and sketched (b) LEED patterns from an

## Chapter 1. Theoretical Background

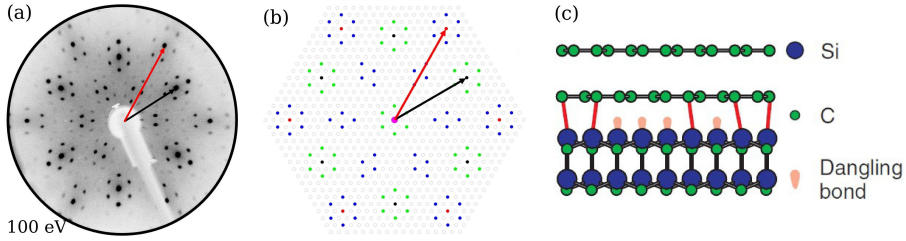


Figure 1.3: (a) Measured and (b) Sketched LEED patterns of an epitaxial monolayer graphene sample. The LEED energy is 100 eV. The unit cell vectors of the substrate SiC and epitaxial graphene are marked by black and red colored arrows, respectively. In (b), the  $6\sqrt{3}$  grid is represented by hollow spots. The substrate SiC spots are highlighted with black color,  $G-R30^\circ$  with red color, visible  $(6 \times 6)$  with green color, and visible  $6\sqrt{3}$  spots with blue color. (c) Sketched side view model of the epitaxial monolayer graphene [2].

epitaxial monolayer graphene sample. The LEED pattern was obtained at an electron energy of 100 eV. The reciprocal unit cell vectors of the substrate SiC and epitaxial graphene are marked by black and red colored arrows, respectively. It is apparent that after the formation of a complete layer, the spot intensity of the graphene is much stronger than that shown in Fig. 1.2 (b). These spots show a  $30^\circ$  difference in the azimuthal direction relative to the substrate spots, reflecting the  $30^\circ$  crystalline orientation. The visible spots of the  $6\sqrt{3}$  grid around the  $G-R30^\circ$  spots are highlighted by blue color. The satellite spots surrounding the substrate spots correspond to the visible spots of the  $(6 \times 6)$  grid and are marked in green color, which also lie on the  $6\sqrt{3}$  grid, as shown in panel (b). Fig. 1.2 (c) displays a side view model of the epitaxial monolayer graphene [2]. The graphene layer is located above the ZLG and suspended by Van der Waals force. In the next section, we are going to discuss hydrogen intercalation of the ZLG on SiC by introducing a hydrogen atomic layer between the ZLG and the substrate. In a such way, the ZLG can also turn into a real graphene layer with  $\pi$  features.

### 1.2 Hydrogen Intercalation of Epitaxial Graphene

The charge transport properties of graphene have been extensively studied since its initial electronic characterization [45], revealing a high carrier mobility due to the low effective mass of the electrons [21, 46]. Gaining insights into the factors that limit charge mobility in graphene is crucial for future technological applications. The high quality and two-dimensional nature of epitaxial graphene on SiC make it an ideal system for investigating graphene's transport properties. Epitaxial monolayer graphene (EMLG) exhibits intrinsic n-doping, and its charge carrier show an undesired temperature dependence due to electron-phonon scattering, which are attributed to the influence of the ZLG- $R30^\circ$  layer [47–52].

Recently, many research groups have investigated the sheet resistance and the influence of scattering centers on the charge transport of epitaxial graphene at the nanometer scale. This includes studies on single substrate steps [53, 54] and transitions between domains with different numbers of stacking layers [55, 56]. Sinterhauf *et al.* revealed local inhomogeneities on nanometer-scale in the sheet resistance of the epitaxial monolayer graphene, which are influenced by both substrate termination and the distance between the graphene layer and the substrate [57]. Variations in this distance affect the interface states, with larger distances resulting in reduced resistance. This is attributed to the buckling of the ZLG, due to residual covalent bonding between the ZLG and the substrate [58, 59]. Therefore, achieving uniform spacing between the epitaxial graphene layer and the substrate is essential for the development and implementation of nanometer sized devices.

To address the issues caused by the ZLG- $R30^\circ$  layer mentioned above, a potential solution is to decouple it from the substrate by introducing specific atomic species between the ZLG- $R30^\circ$  layer and the substrate. This insertion of atoms can break the bonds and saturate the dangling bonds of the substrate's terminating Si atomic layer. As a result, the ZLG- $R30^\circ$  layer becomes spatially and chemically decoupled from the substrate, transforming into a quasi-freestanding graphene layer. This process is commonly referred to as the intercalation.

Over the past decade, significant efforts have been made to decouple graphene



## Chapter 1. Theoretical Background

---

layers from their substrates by intercalation. Various elements, including H, Au, Ge, Li, Sb, Bi, Si, Cu, Pb, and etc., have been explored as intercalation species. These elements have been shown to penetrate the graphene layers and ultimately reach the interface between the ZLG and the SiC substrate [2, 60–68]. In addition to spatial decoupling, intercalation also alters the electronic properties of graphene. For example, Ge intercalation can result in either n- or p-type doping of the quasi-freestanding monolayer graphene (QFMLG), depending on the amount of Ge present [61]. Pb intercalation can significantly increase graphene's work function and switch its charge carrier type from electrons to holes by suppressing electron transfer from the substrate [65]. Furthermore, 2D superconductivity has been observed in Ca-intercalated bilayer graphene, although in this case, the Ca atoms are intercalated between the two graphene layers rather than between the ZLG and substrate [69]. This highlights the broad range of electronic phenomena that can be tuned through intercalation.

Hydrogen is a promising candidate for intercalation of the ZLG, enabling the formation of an ultra-flat QFMLG with a highly uniform electronic density at the interface. Sforzini *et al.* experimentally determined the corrugation and buckling of hydrogen-intercalated QFMLG to be as small as 0.02 Å, along with its adsorption height on the substrate, possibly allowing for a significant enhancement in transistor performance following hydrogen intercalation [70]. Hence, QFMLG clearly has a higher electronic applicability than the epitaxial monolayer graphene [71]. Moreover, the QFMLG exhibits a lower doping level than the EMLG, with the QFMLG slightly p-doped while the EMLG strongly n-doped [2, 52, 72].

Compared to other intercalation species, hydrogen offers greater flexibility, as its intercalation is reversible by annealing [2, 72, 73]. Hydrogen can saturate most of the terminating Si atoms directly beneath the ZLG- $R30^\circ$  layer, ensuring large-scale homogeneity. In contrast, intercalation with noble metals may leave excess materials on the graphene surface that do not participate in Si atom saturation, potentially impacting the electronic properties of the intercalated graphene. This issue is avoided by using hydrogen, as any residual hydrogen on the graphene surface can be easily removed by degassing.

However, in practical hydrogen intercalation experiments, achieving complete saturation of all Si atoms with hydrogen is challenging, leading to hydrogen deficiencies [72, 74]. These deficiencies act as scattering centers, potentially reducing charge mobility in the QFMLG layer. Therefore, a thorough understanding of the hydrogen intercalation mechanism is crucial. Although various techniques, including theoretical studies, have been employed to interpret the intercalation process and the properties of the resulting products [70, 73, 75–81], many aspects remain contentious. The precise location and mechanism about how hydrogen atoms enter the interface between the ZLG and the substrate are still not fully understood. For instance, Watcharinyanon *et al.* investigated hydrogen-intercalated graphene using STM and suggested that hydrogen atoms penetrate through the graphene and ZLG [82]. However, this claim contradicts theoretical calculations [83, 84]. Sakakobara *et al.* reported that the hydrogen intercalation initiates locally and simultaneously on the terraces, not at the step edges, suggesting that the hydrogen can penetrate the ZLG. They attributed this to ZLG's intrinsic defects [81]. Additionally, the factors influencing the stability of hydrogen-intercalated samples are not yet clear, as some studies report stability lasting several months [2], while others indicate stability of only a few days [78].

Currently, most of the hydrogen intercalation investigations focus on the conventional epitaxial graphene, which commonly results in the QFMLG or aligned bi-layer graphene with an AB-stacking (Bernal) [2, 77, 82, 85]. Since  $0^\circ$ -rotated epitaxial monolayer graphene with a high quality can be achieved [6], which will be discussed in the next section, hydrogen intercalation can be a promising approach towards large scale  $30^\circ$ -twisted bilayer graphene (TBG) with very precise angle control and reproducibility.

### 1.3 Twisted Bilayer Graphene (TBG)

Plenty of theoretical predictions and experimental observations have revealed novel and exotic properties in graphene. Perhaps the most intriguing aspect is that its electronic properties can be tuned through proximity effects without altering its geometric structure. A prime example of this is graphene-based twistrionics, where twisted bi- and multilayers form specific Moiré superlattices

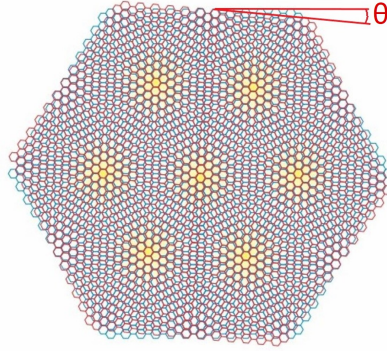


Figure 1.4: Moiré pattern formed by overlapping and rotating two honeycomb lattices [3]. Highlighted in yellow are the repeating regions where the hexagons in the two sheets nearly align.

[86–95]. Twisted bilayer graphene (TBG) with various twist angles has revealed a range of intriguing properties, including unconventional intrinsic superconductivity, a tunable band gap, strong interlayer coupling, and the quantum Hall effect, etc. [91, 96–100].

A schematic representation of a quasi-periodic structure (Moiré Lattice), formed by overlapping two monolayer graphene-like sheets with a small rotating angle  $\theta$ , is depicted in Fig. 1.4. In the graphene-based twisted bilayer system, and in an ideal scenario, where the graphene sheets are undistorted, the structure of the sheets almost matches at some positions (centers), with increasing misalignment toward the edges. The resulting moiré pattern has a unit cell much larger than the graphene lattice constant. The alternating aligned and misaligned stacking order within the moiré superlattice and the variation in the unit cell size can be achieved simply by adjusting the angle between the two graphene sheets, making superlattice modulation possible. Strong correlations between charge carriers in the two graphene sheets after the formation of a moiré lattice hinder their free movement.

The only and decisive parameter affecting the properties of twisted bilayer graphene (TBG) is the twist angle between the graphene sheets. Notably, the excellent work by Cao *et al.* revealed the intrinsic unconventional superconduc-

### 1.3 Twisted Bilayer Graphene (TBG)

---

tivity in TBG with a "magic angle" [97]. It was discovered that at a magic angle of  $1.1^\circ$ , a flat electronic band structure emerges near the Fermi energy. These flat bands, arising from strong correlations between charge carriers, allow for the emergence of gate-tunable superconducting and correlated insulating phases in graphene-based devices. Moreover, the family of the magic angles is getting larger with more efforts done by different researchers, for example, remarkable strong interlayer coupling and charge correlations are also observed in TBG with rotation angles of  $0.93^\circ$ ,  $1.27^\circ$ , and  $30^\circ$  [98, 101, 102].

For small twist angles, the interlayer coupling weakens as the twist increases, leading the bilayer film to act more like two independent monolayers within a certain range [87, 88]. However, at the maximum twist angle of  $30^\circ$ , symmetry considerations result in a significant resurgence of interaction. The first theoretic prediction of TBG quasicrystal is the algorithmic construction done by Stampfli, with two ideal hexagonal grids rotated by  $30^\circ$  with respect to each other [103]. Strong interactions between electrons in the  $30^\circ$ -TBG leads to the speculation of some intriguing phenomena, including mirrored Dirac cones, nearly flat bands, and dodecagonal quasicrystallinity [98, 104, 105]. Theoretical calculations of the electronic band structure on freestanding  $30^\circ$ -TBG was first proposed by Moon *et al.*. Twelve-fold symmetric resonant states with quantized angular momentum are presented and localized in a finite-size geometry in the electronic spectrum, and nearly flat bands are expected in a wide energy range of 0.3 eV [105].

A common method for producing TBG with a specific twisted angle is the conventional micro-mechanical exfoliation (tear and stack) technique [99]. However, this approach has inherent limitations, particularly in terms of precise angle control and reproducibility. This issue is especially pronounced for TBG samples with a large twisted angle of  $30^\circ$ , which demand extremely high orientation accuracy, since even a slight deviation can destroy their quasi-crystalline features [105]. Additionally, the bilayer graphene produced using this technique is limited to a scale of only tens of square micrometers, making it unsuitable for large-scale industrial applications. In monolayer graphene, charge carrier mobility is primarily constrained by impurities. However, in TBG, variations in the regional twist angle become a crucial factor influencing the electronic properties of devices. Achieving uniform angle control across the entire TBG is

## Chapter 1. Theoretical Background

---

essential to ensure consistent and reproducible properties in different devices.

An alternative way to produce TBG is applying epitaxial growth of graphene on suitable substrates. In terms of larger and well-ordered samples, this is much more promising than the "tear and stack" method. Obviously, for achieving epitaxial TBG, one has to find ways to grow graphene in different orientations.

Graphene layers can naturally grow on a Pt (111) surface as carbon atoms diffuse out of the substrate, indicating that the Pt (111) substrate also serves as an internal carbon source [30, 31]. It has been found that the crystallographic orientation of graphene produced through carbon atom segregation can be controlled by adjusting the annealing temperature. Specifically, annealing at around 1200 °C results in graphene layers rotated by 30° relative to the substrate, while annealing at approximately 1600 °C produces graphene with a 0° rotation [98]. Therefore, achieving 30°-TBG on a Pt(111) substrate becomes possible by operating stepped annealing at different temperature. However, the TBG that is grown in this way has limited size and yield.

Chemical vapor deposition (CVD) is widely used to produce single-layer and bilayer graphene on various transition metal substrates, which play the role of catalysts [106]. The discovery of exclusive formation of 0°-rotated bilayer graphene and 30°-rotated TBG on a Cu(111) surface has introduced the potential for precise control of stacking angles using the CVD method [107–110]. Pezzini *et al.* quantitatively demonstrated the capabilities of this method [111]. They conducted low-pressure CVD on high-purity Cu foils in a cold-wall reactor, resulting in isolated hexagonal graphene domains with a bilayer configuration on the surface, exhibiting two distinct layer orientations. Among these domains, 59% showed AB-stacking (0° rotation), while 41% were twisted by 30°. Additionally, a notable portion of monolayer graphene domains coexisted on the surface.

Other CVD preparations on Cu related substrate are also reported. For instance, epitaxial growth via CVD on Cu-Ni alloys enables modulation of the mono-/bilayer ratio on the surface, achieving over 90% uniform bilayer graphene coverage by controlling the Ni concentration and the cooling profile during CVD [112, 113], which in turn increases the yield of TBG. Small-angle bilayer

### 1.3 Twisted Bilayer Graphene (TBG)

---

graphene with a rotation of  $3^\circ$  to  $5^\circ$  has been observed as the predominant product on atomic-stepped Cu(311) and Cu(110) surfaces [114]. These findings suggest that fine-tuning the stacking angle of bilayer graphene could be further refined by optimizing the surface of the Cu catalyst. Most recently, Ma *et al.* reported wafer-scale growth of  $30^\circ$ -TBG on a  $\text{Cu}_{0.75}\text{Ni}_{0.25}$  alloy [115]. In this process, the first nucleation layer of graphene is deposited on  $\text{Cu}_{0.75}\text{Ni}_{0.25}$  (111) with the same orientation as the substrate, while the second graphene layer forms with a  $30^\circ$  rotation relative to the first layer. It is claimed that the  $30^\circ$  rotation is attributed to the combined influence of the Cu/Ni single crystal and the first graphene layer.

Epitaxial graphene growth on SiC has proven to be a highly effective method. As discussed above, thermal decomposition of the topmost few layers of SiC in an ultra-high vacuum (UHV) can produce graphene layers with a  $30^\circ$  rotation relative to the substrate lattice, which is generally considered the conventional orientation for epitaxial graphene on SiC. Ahn *et al.* proposed an approach to achieve  $30^\circ$ -rotated twisted bilayer graphene (TBG) by first growing a hexagonal boron nitride (h-BN) layer on 4H-SiC(0001) [104]. In this method, the SiC crystal is annealed in a borazine atmosphere at  $1050^\circ\text{C}$ , resulting in an h-BN layer aligned with the bulk lattice (i.e.,  $0^\circ$ -rotated). Upon subsequent annealing at a higher temperature ( $1600^\circ\text{C}$ ), the h-BN layer carbonizes and transforms into graphene, maintaining its orientation, thereby producing a graphene layer oriented  $0^\circ$  with respect to the substrate. Bocquet *et al.* [6] demonstrated that this unconventional orientation of the graphene layer can also be achieved through a one-step process. By annealing the 6H-SiC(0001) surface in a borazine atmosphere at temperatures above  $1300^\circ\text{C}$ , they directly obtained the  $0^\circ$ -oriented graphene with a better crystalline quality. In this case, the borazine molecules appear to act as surfactants on the heated SiC surface, promoting the formation of graphene in the unconventional  $0^\circ$  orientation during the thermal decomposition process.

These reports offer a new idea to prepare twisted bilayer graphene (TBG). Growing a graphene layer in its conventional  $30^\circ$  orientation underneath the  $0^\circ$  oriented layer would result in a TBG with exactly  $30^\circ$  twist angle. However, conventional epitaxial growth of graphene through the thermal decomposition

## Chapter 1. Theoretical Background

---

of SiC is not a self-limiting process. This becomes particularly challenging once the surface is already covered by a monolayer of graphene, making it difficult to ensure uniform growth of the second layer. The hydrogen intercalation of the ZLG could be the another option. In this work we studied both the epitaxial growth of 0°-rotated monolayer graphene on a 6H-SiC(0001) surface (**Chapter 3**), and the hydrogen intercalation of the underlying ZLG (**Chapter 4**) using LEEM technique.

Moreover, by manipulating graphene's structural architecture, such as folding or rolling of its flat 2D sheet, various graphene derivatives can be created. In the following section, we will explore a unique tire-shaped molecule composed exclusively of benzene rings arranged in a cyclic structure.

### 1.4 Cycloparaphenylenes (CPPs)

Hoop-shaped  $[n]$ -Cycloparaphenylenes ( $[n]$ -CPPs) have attracted paramount attentions of chemists due to their unique cyclic structure and  $\pi$ -conjugation in azimuthal direction, which have great potential in the electronic, optical, and supramolecule architectural applications [4, 5, 116–127].  $[n]$ -CPPs denote the cyclic construction of the smallest structural unit paraphenylene (PP) with  $n$ , the number of the PPs in a cycle.

For a decade, many efforts have been spent on synthesizing CPPs with various numbers  $n$ . Although all  $[n]$ -CPPs molecules have a rather simple geometric structure in common, their synthesis is still challenging due to the significant distortion of the phenylene rings, which imposes a high strain energy on the molecules [4]. The strain energy increases with the decrease of the number  $n$  and the molecule diameter, and smaller CPP molecules embody considerably high strain energy [119]. Nowadays, the synthesis of CPPs with  $n$  in the range from 5 to 20 have been reported. [5]-CPPs is the smallest molecules with 119  $kcal\ mol^{-1}$  strain energy [4, 117, 118, 120–123].

$[n]$ -CPPs exhibit some intriguing size-dependent properties. Much higher molecular conductance at a relative short transport distance is observed on CPPs in comparison to the linear oligoparaphenylenes (LPPs) (a standard linear

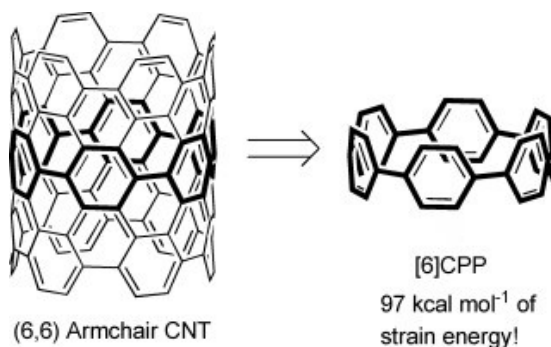


Figure 1.5: [6]-CPP, the shortest-possible subunit of a (6,6) CNT [4].

conjugation), and the size-dependent conductance within the CPPs family enables the large charge transport modulation, which can be potentially applied in the single molecule and organic devices [124]. With decreasing  $n$ , the LUMO and HOMO energies of the CPP molecules decrease and increase, respectively, which causes a smaller HOMO/LUMO gap for smaller CPP molecules and corresponding lower oxidation potential [120, 121]. The fluorescence spectra of CPPs is also strongly impacted by their size: the smaller the CPP molecules, the larger the measured Stokes shift, which can be attributed to the released strain energy in the excited states [117, 121, 128]. Moreover, it is found that the CPPs become non-fluorescent when  $n \leq 6$ .

Aside size controlling, a lot of ingenious work has also been reported to achieve tuning properties of the CPP molecules. Tarabayashi *et al.* are able to synthesize Möbius-ring shaped CPPs by alkene insertion [127]. [6]-CPPs can become fluorescent when their centrosymmetry is broken, and it is realized by nitrile-substitution of one benzene subunit to form a meta-connection [125]. As introduced in the last paragraph, the CPPs become easier to be oxidized with decreasing sizes because of the lowering HOMO/LUMO gap. However, it is also possible to negatively charge the CPPs, especially, for some small CPPs. Spisak *et al.* proposed the controlled reduction of [6]-CPPs with alkali metals in Tetrahydrofuran (THF), and successfully obtained the first mono- and dianions of [6]-CPPs [5].

In this work, we focus on the [6]-CPP molecule, one of the smallest members



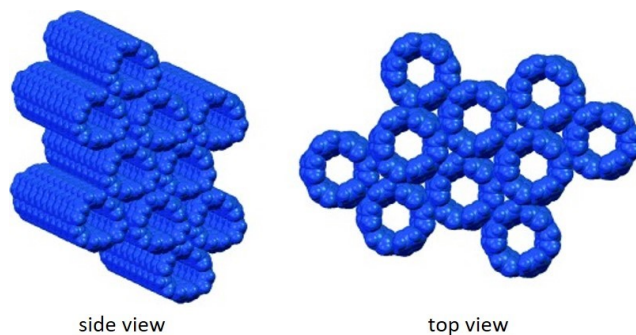


Figure 1.6: Packing structure of [6]-CPPs in the crystalline state, which is condensed from a dichloromethane solution [4].

of the CPP family, with its configuration depicted in Fig. 1.5. In chemistry, the carbon atoms of a benzene ring are numbered from 1 to 6. In [6]-CPP, phenylene rings are connected in a 1,4-linkage, meaning they are joined through the carbons at positions 1 and 4, resulting in a linear and cyclic arrangement of the rings. Consequently, a single [6]-CPP molecule can be viewed as the shortest subunit of armchair carbon nanotubes (CNTs). The C-C bonds in [6]-CPP are nearly equivalent, preserving the benzenoid structure, despite the benzene rings are extensively bent as a consequence of its small geometry.

The packing structure of [6]-CPPs in crystalline state is fascinating. The molecules are packed distinctly depending on their crystallization medium, either from a dichloromethane solution or in a solvent-free manner. When condensed from a solution, the molecules are aligned linearly, and stacked like cylinders. Fig. 1.6 depicts the side view and top view of the packing structure model. The molecules are assembled perfectly from the bottom-up, which probably paves a new way towards (6,6) armchair carbon nanotubes. However, the tire-like configuration of the [6]-CPP molecule with a hollow center facilitates the encapsulation of disordered solvent molecules in the central cavity when the crystal grows from solutions.

A planar and tight packing of the [6]-CPP molecules can be formed when the crystallization originates from an unsolved polymorph [5]. A direct deposition from a polymorph on a substrate achieves solvent exclusion. Molecules are

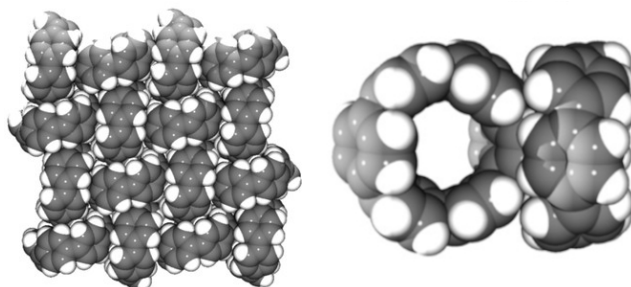


Figure 1.7: Space-filling model for the herringbone-shaped packing of molecules, along with the side view of two inserted [6]-CPP molecules [5].

standing like tires on the surface and arranged in a herringbone pattern, shown as the space-filling model in the left panel of Fig. 1.7. Interestingly, a small part of a molecule fills in the central cavity of the neighboring molecule which minimizes the empty internal space and leads to a tighter packing. The side view of two inserted [6]-CPP molecules is shown in the right panel of Fig. 1.7.

Our interest in the [6]-CPP molecules was inspired by the work of Prof. Dr. Michael Gottfried's group at the Philipps-Universität Marburg, particularly, their investigation about the evolution behavior of the [6]-CPP molecules deposited on a Cu (111) substrate at varying temperature, which has been schematically interpreted in Fig. 1.8. The STM images reveal various structures formed by the molecular precursors on the surface. It was found that the [6]-CPP molecules can be deposited on a Cu (111) substrate, and form an ordered herringbone pattern at RT around 25 °C. In a surface-catalytic process, the opening of the molecular rings takes place at around 130 °C. The on-surface ring-opening leads to the polymerization of ultra long polyparaphenylene (PPP) at around 180 °C. A higher annealing temperature at 230 °C triggers stronger interaction of PPP chains with the substrate. As a consequence, polybenzynes chains are formed. When the temperature reaches 330 °C, the product of [6]-biphenylene ribbons (BPRs) is observed on the surface of the substrate. Moreover, when the annealing temperature is even higher, the diameter of obtained BPRs will be larger. In this work we have tried to observe these processes in situ using LEEM, with moderate success. The results are shown in **Chapter 5**.

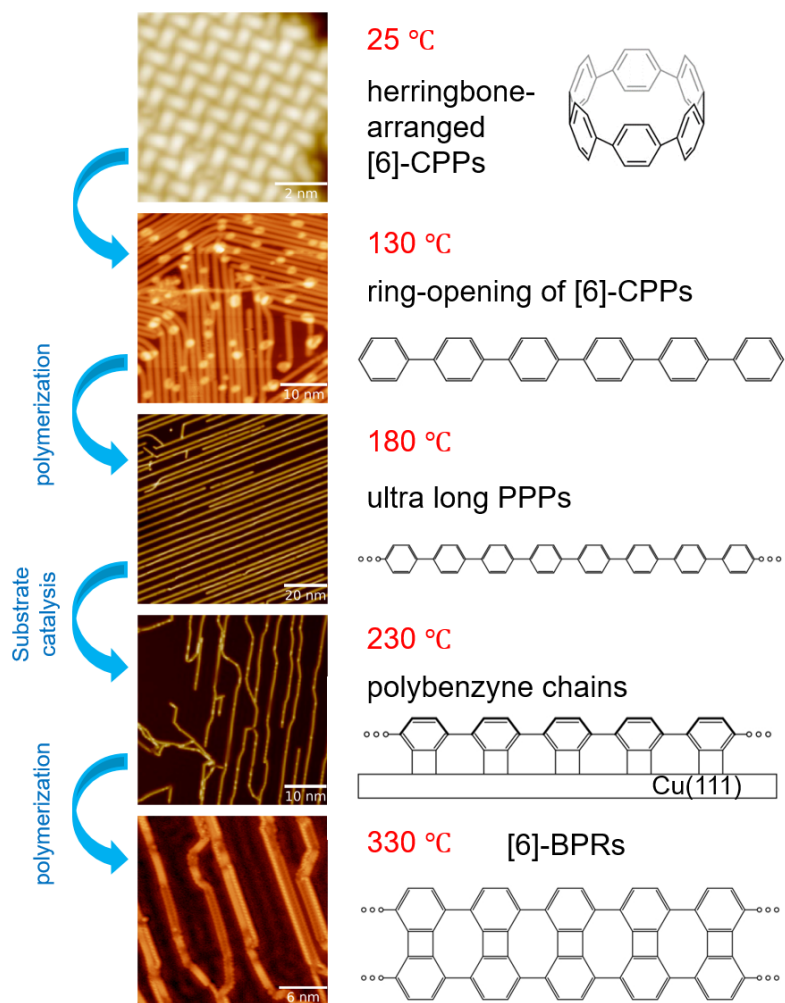


Figure 1.8: Polymerization of biphenylene ribbons (BPRs) with [6]-CPP molecules as precursors on a Cu(111) surface. STM images are from Prof. Dr. Gottfried's group, Marburg.

## 2 Experimental Techniques

### 2.1 Introduction to LEEM

Low energy electron microscopy (LEEM) is a powerful technique for examining atomically clean surfaces, nanostructures, the growth of the first monolayers in molecular thin films, and the formation and transition of phases etc.. Due to the low-energy interactions between electrons and matter, LEEM provides surface-sensitive and non-destructive measurements (even for radiation sensitive materials like, e.g., organic molecules), allowing detailed insights into the morphology and structural features of planar two-dimensional surfaces.

#### 2.1.1 Experimental Setup

The LEEM instrument in our lab is an aberration-corrected spectroscopic photoemission and low-energy electron microscope (AC-SPELEEM 3) provided by Elmitec Elektronenmikroskopie GmbH. Fig. 2.1 presents an image of the LEEM setup. The green lines and arrows represent the electron path and movement direction within the instrument, while the orange lines illustrate the path within the mirror column when aberration correction is active. Typically, the instrument operates with a resolution of 10 nm. The system comprises three main sub-units: the ultrahigh vacuum (UHV) system, the electron optic system, and the imaging and detection system. Detailed information about the first two units will be discussed in the following sections.

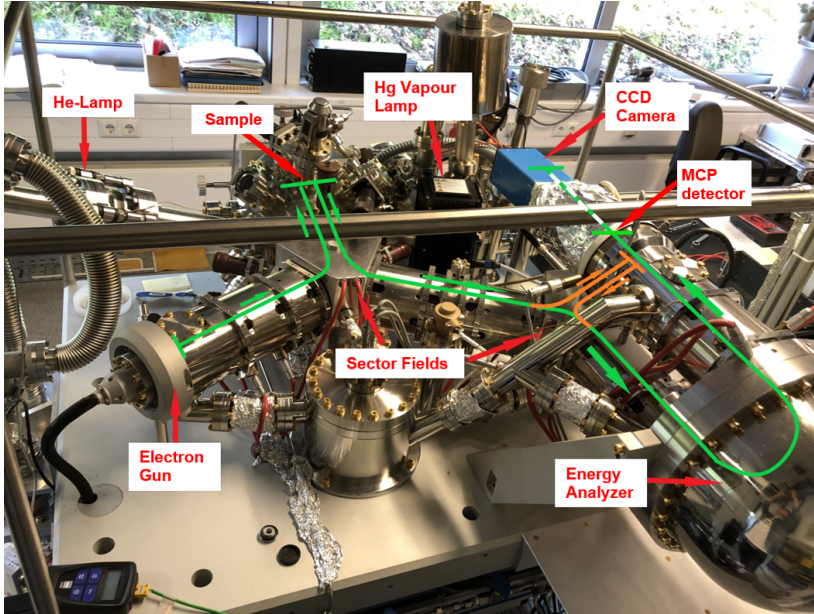


Figure 2.1: Elmitec AC-SPELEEM 3 in our lab.

### Ultrahigh Vacuum (UHV) System

It took nearly 60 years from Davisson and Germer's classical diffraction experiment [7] to the first publication of LEEM surface imaging by Telieps and Bauer [8]. One important reason was the lack of ultrahigh vacuum (UHV) systems and effective surface cleaning methods at that time [129]. UHV working conditions are essential for LEEM because they significantly reduce electron scattering caused by gas atoms or molecules, and prevent the samples from contamination in the chamber. A schematic illustration of the pumping system of the LEEM instrument is shown in Fig. 2.2. The UHV section, highlighted in green, includes the preparation chamber (PC), the main chamber (MC), and the column system (CL) for the path of the electron beam. Typically, the pressure in the main chamber is maintained at a base level of  $10^{-10}$  mbar, while during deposition or surface exposure, it can reach a maximum of  $10^{-7}$  mbar. For safety, the chambers are usually separated by manual valves to prevent cross-contamination in case of a leak in any specific chamber. During LEEM operation, a high voltage

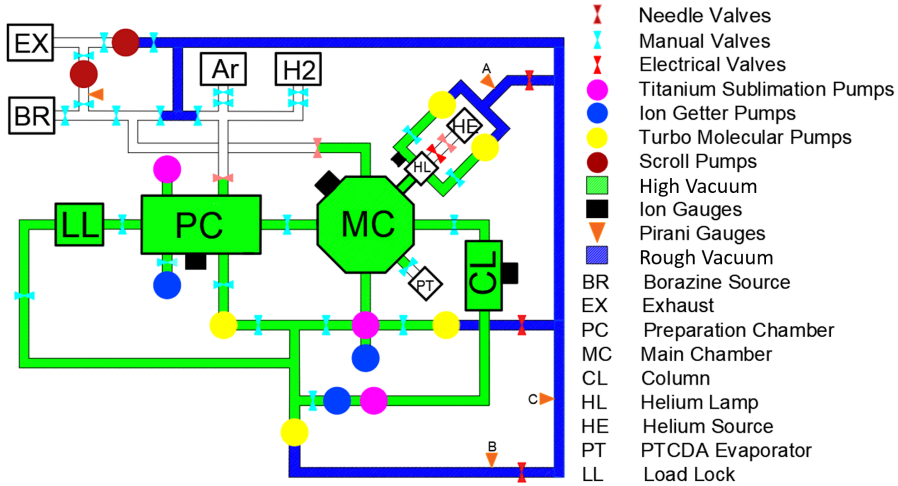


Figure 2.2: Schematic representation of the pumping system of the AC-SPELEEM.

system of 20 kV is applied to control the electron kinetic energy. To protect the electronics, an interlock system is essential. If the pressure in any chamber exceeds the set threshold, the high voltage system will automatically shut down. Additionally, three electromagnetic valves, normally powered on, are positioned between the pre-vacuum and UHV sections. In the event of a power failure, these valves automatically close to isolate the UHV section, while backup batteries keep the turbo-molecular pumps running temporarily. This system ensures the UHV's integrity is maintained as much as possible.

### Electron Optic System

In LEEM, low-energy electrons are used as probes to investigate the sample surface. Electromagnetic lenses are involved to guide these electrons. Figure 2.3 illustrates the schematic electron optics of the LEEM instrument in our lab. A Schottky field emitter is selected as the electron source due to the high energy coherence of the emitted electrons. Initially, the electrons are accelerated to a kinetic energy of 20 keV by an electric field. The electron beam then passes through three condenser lenses (CL1, CL2, CL3), which focus the beam. To achieve normal incidence on the sample surface, the electron beam is deflected

## Chapter 2. Experimental Techniques

by  $60^\circ$  by the magnetic sector field 1 (Sect 1). The illuminated area of the sample can be controlled by inserting an illumination aperture (IA) of varying sizes, located within sector field 1.

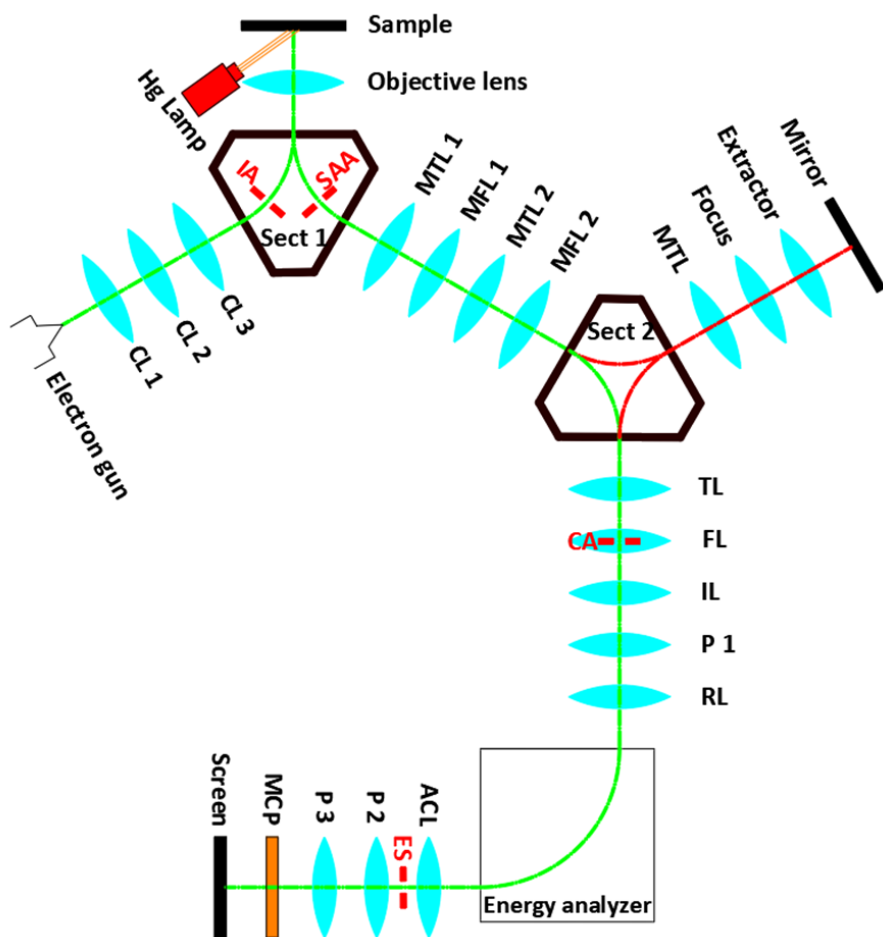


Figure 2.3: Schematic representation of electron optics of the AC-SPELEEM. The green and red lines represent the electron pathway. The electromagnetic lenses are depicted in blue convex icons.

Before reaching the sample surface, the electron beam must pass through an essential lens called the objective lens, which focuses the beam onto the sur-

face and produces LEEM images at various focus conditions, including focus, underfocus, and overfocus. The resolution of a LEEM instrument is primarily constrained by the spherical and chromatic aberrations of the objective lens. Additionally, an electric field with a potential difference of  $-20 \text{ kV} + U_{start}$  is applied between the objective lens and the sample to decelerate the electrons. This allows the electrons to reach the surface with a well-defined energy of  $e \times U_{start}$ , where  $U_{start}$  is known as the "Start Voltage". After interacting with the sample surface, the reflected or diffracted electrons are re-accelerated by the same electric field, regaining their original kinetic energy of 20 keV. Consequently, the electrons maintain a kinetic energy of 20 keV throughout the entire electron optics, except during their interaction with the sample surface, and on the pathway through the energy analyzer.

The magnetic sector field is used to separate the reflected electron beam from the incoming electron beam originating from the illumination column. Both beams are deflected by  $60^\circ$  in opposite directions. The reflected beam then passes through the intermediate optics, which consists of two mirror transfer lenses (MTL 1, MTL 2) and two mirror field lenses (MFL 1, MFL 2). Afterwards, the electron beam reaches sector field 2 (Sect 2), where it can either be directly deflected into the imaging column or first pass through the correction mirror column. The correction mirror column compensates for the spherical and chromatic aberrations of the objective lens using several electrodes with specific shapes and electric potentials. This correction enhances the spatial resolution of the AC-SPELEEM to become better than 2nm, and increases the transmission of the microscope by a factor of approximate 8. However, since the alignment of the corrector is complicated and time-consuming, it is only used for experiments for which resolution is crucial.

The imaging column consists of five lenses: transfer lens (TL), focus lens (FL), intermediate lens (IL), first projector lens (P1) and retardation lens (RL). These lenses are used for projection of electrons. By introducing a contrast aperture (CA) in the diffraction plane, a specific diffraction electron beam is allowed to pass and form subsequent images in dark field mode of LEEM, which will be introduced later.



## Chapter 2. Experimental Techniques

---

The instrument is equipped with a hemispherical energy analyzer, allowing for spectroscopic investigations, such as constant energy mapping in angle-resolved photoemission spectroscopy (ARPES). After passing through the energy analyzer, the electron beam enters the projector column, where it passes through an acceleration lens (ACL), an energy slit (ES), and two projector lenses (P2, P3). Finally, the electrons reach a micro-channel plate (MCP) and strike the high-resolution fluorescent screen, with the resulting images captured by a CCD camera.

By inserting specific apertures and changing the focal lengths of the specific lenses, AC-SPELEEM can realize the switch between bright field LEEM (BF-LEEM) mode, dark field LEEM (DF-LEEM) mode, and low energy electron diffraction (LEED) mode. These operating methods will be discussed in more detail in the following.

### 2.1.2 Contrast mechanisms in LEEM imaging

In LEEM imaging, two primary contrast mechanisms are present: amplitude contrast and phase contrast. Amplitude contrast arises from variations in local electron reflectivity, which depends on both the species and the electron energy. Contrast appears when different materials, or the same material with varying reconstructions, are present on the surface. Additionally, by adjusting the kinetic energy of the electrons, the reflectivity in the same area can change due to the surface's electronic structure. This characteristic is further explored through a spectroscopic technique known as LEEM-*IV*, which will be discussed in detail later.

Another important contrast mechanism is phase contrast, e.g., originating from the interference of electron waves reflected from flat terraces on both sides of an atomic step. This interference results from the phase shift caused by differences in the path length of the electron waves. As a result, step edges become visible due to the destructive interference of the reflected electrons, revealing the surface contours. Since the wavelength of low energy electrons in LEEM is comparable to atomic distances, in this case to the height of atomic steps, varying the electron energy allows detection of a wide range of step heights

[130].

### 2.1.3 Bright Field and Dark Field LEEM

In normal LEEM mode, the contrast aperture is not involved in the electron optics, allowing all diffraction beams to contribute to the imaging. However, by introducing a contrast aperture at the focal plane, a specific diffraction beam can be selected while the other beams are blocked, highlighting surface domains or regions responsible for the formation of that particular beam.

In bright field mode, as illustrated in Fig. 2.4 (a), the incident electron beam hits the sample surface perpendicularly, and all diffracted beams are blocked by the contrast aperture except for the (00) main beam (black-colored), which travels along the optical axis. The electrons in the (00) beam interact with the surface without any parallel momentum transfer, as they arrive and leave perpendicularly. Compared to normal LEEM imaging, images obtained in bright field mode have improved resolution due to reduced spherical aberration from the magnetic lenses.

In dark field mode, a non-(00) beam is selected to pass through the contrast aperture, as shown in Fig. 2.4 (b). From the perspective of spherical aberration, it is undesirable for the electrons applied for LEEM imaging to travel off the optical axis of the lenses. Additionally, positioning the contrast aperture over a large range in a UHV environment without causing pressure fluctuations is challenging. To solve this issue, one solution is to tilt the incident electron beam, as depicted in Fig. 2.4 (b). This allows the non-(00) diffraction beam to leave the sample surface along the normal direction and pass through the contrast aperture. By selecting which electron beam passes the aperture, DF-LEEM images show only surface domains with specific crystalline orientations, and reveal their structural distribution across the sample surface.

### 2.1.4 LEEM-IV Measurements

A LEEM-IV measurement (Intensity vs. Voltage ( $U_{start}$ , i.e., electron energy)) is a spectroscopic extension of the LEEM technique, widely used to study the

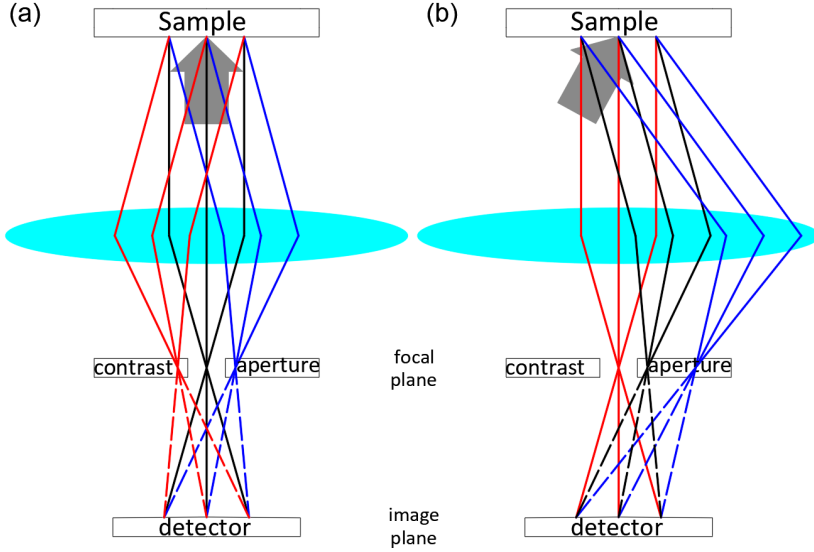


Figure 2.4: Electron beam pathway in bright field mode (a) and dark field mode (b). Gray arrow represents the incident beams. Red, black and blue lines represent the pathway of diffracted electrons.

electronic and geometric structures as well as the chemical components on the surfaces.

In a LEEM-*IV* measurement, the local electron reflectivity is recorded as a function of electron energy. The electron reflectivity on the surfaces is not only species-related, but depends on many aspects, as, e.g., the geometric and electronic structure. This means that the reflectivity can vary on the same material with different crystal orientations, or on the same crystal surface but with different reconstructions, since they have locally different electronic band structures. The *IV* curves are extracted as the fingerprint of specific structures owing to their inherent connection with the electronic band structures [131–136].

In graphene-related research, LEEM-*IV* measurements are commonly used to determine the number of graphene layers in a stack [28, 37, 38, 137, 138]. Specifically, for epitaxial graphene, it has been shown that the number of stacking layers corresponds to the number of minima in the *IV* curve within the energy

range of 0 to 7 eV, since quantized oscillations of the electron reflectivity occur in this range [2, 38, 137, 138]. These oscillations in reflected electron intensity arise from interference effects between electron beams reflected at different interfaces within the graphene stack. This phenomenon can also be interpreted as the splitting of the interlayer band of graphite into discrete levels in few-layer graphene [138]. Furthermore, it should be pointed out that in the LEEM-*IV* measurements to interpret the stacking configuration of epitaxial graphene layers on a SiC, the ZLG does not contribute to the oscillations in the *IV* spectra, as it remains electronically coupled to the substrate.

The LEEM-*IV* data is a three dimensional image stack consisting of the intensity  $I$  as a function of the direct space coordinates  $x$  and  $y$  and the electron energy ( $e \times U_{start}$ ). Conventionally, the LEEM-*IV* spectra are extracted by selecting an area on the surface (i.e., a certain  $x, y$  range) that is homogeneously filled by a specific structure, and integrating the intensity of pixels within the selected area. This is performed for images recorded at different electron energy. A curve presenting integrated intensity with respect to the energy can be obtained.

The essential shortcoming of the method is the manual selection of the area that shall be integrated, which sometimes is difficult and prone to errors, in particular when the homogeneous areas are very small. Moreover, the effect coming from the borders between different structures are systematically ignored owing to their extremely low dimension that are difficult to be perceived.

In this work, we applied an alternative way of data analysis which lifts those shortcomings, and on top allows a semi-automatized identification of areas on the surface having similar *IV* signatures. *IV* curves are extracted from the data cube on a pixel-by-pixel basis, such that each plotted curve corresponds to one pixel position (with coordinates  $x, y$ ) in the LEEM image. This approach enables a more systematic and efficient analysis of LEEM-*IV* data while reducing the potential for manual errors. The next step is to group the extracted spectra according to their similarities. Afterwards, a false-color image can be generated based on the grouping results, which represents distribution of different structures on the surface distinguished by their *IV* curves, i.e., by their electronic properties. Similar approaches are reported in Refs. [139, 140], however, in

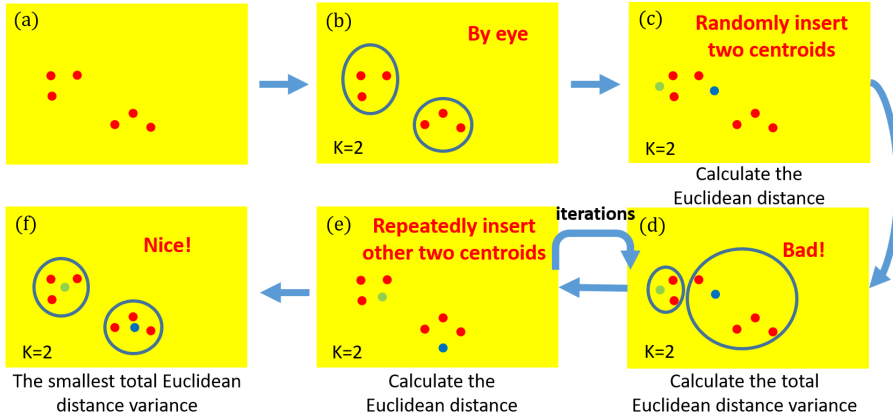


Figure 2.5: Schematic interpretation of the clustering principle of  $K$ -means.

contrast to their data processing methods, here the data is pre-processed as little as possible in our case, and therefore, it is less prone to artifacts.

Pixel-by-pixel analysis of LEEM- $IV$  data typically results in an extensive dataset, often containing hundreds of thousands of curves, making manual clustering impracticable. To streamline this process, clustering algorithms must be employed. In our case, we use the well-known  $K$ -means algorithm [141].

### 2.1.5 Clustering Algorithm $K$ -means

The  $K$ -means is a popular clustering algorithm used for grouping data points into  $K$  clusters based on their similarities, with the only predefined parameter being the desired number of clusters,  $K$ . It has been widely applied in data processing, market analysis, risk evaluation, image recognition and processing, etc. [142–145].  $K$ -means is based on calculating of distances between the data points in the Euclidean space, and minimizes the variances within each cluster (squared Euclidean distances, also known as within-cluster sum of square (WCSS)) through iterations.

A simplified clustering experiment is illustrated in Fig. 2.5, using six data points to explain the working principle of the  $K$ -means algorithm. Six red spots are

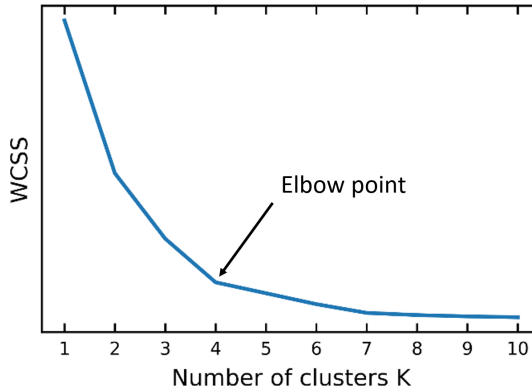


Figure 2.6: Elbow method for determining the  $K$  value of  $K$ -means, in which WCSS with respect to the number of clusters  $K$  is plotted.

presented in Fig. 2.5 (a). Apparently, they can be visually clustered into two groups, with three of them in each group. While there are more sophisticated methods for determining the optimal value of " $K$ ", which will be discussed later, in this example,  $K$  is set to 2.

The algorithm initially places two centroids randomly, representing the centers of the two clusters, see panel (c), colored in green and blue, respectively. The algorithm will calculate and compare the Euclidean distances between each data point with respect to the two centroids, assigning each data point to the cluster whose centroid is closer. The clustering result of this step is shown in Fig. 2.5 (d), where the leftmost two points are assigned to the first cluster with the green centroid, and others to the second cluster with the blue centroid.

To evaluate the clustering result, the algorithm compares the total variation within the clusters and iteratively refines the positions of the centroids. Obviously, the result shown in panel (d) is not the most ideal case. Since  $K$ -means did not see the best clustering so far, the algorithm will continue moving the centroids towards positions with smaller calculated total variances, as shown in panel (e). After many iterations, the algorithm will be able to find the optimal positions of the two centroids that minimize the total within-cluster sum of squares (WCSS), as depicted in Fig. 2.5 (f).

## Chapter 2. Experimental Techniques

---

Obviously, the method strongly depends on the preset number  $K$ , and the larger the chosen number  $K$  is, the smaller the total within variance of clustering. However, finding the optimal number of clusters,  $K$ , is a crucial step to ensure that the clustering results are meaningful and effective. One common method for determining the appropriate  $K$  value is the "Elbow" method. An example of the Elbow plot (randomly generated) is shown in Fig. 2.6, where the WCSS is plotted against different  $K$  values. The plot shows a significant reduction in WCSS at  $K = 4$ , after which the decrease in WCSS becomes less pronounced. Therefore,  $K = 4$  represents the "Elbow point", and is the appropriate choice for the clustering experiment.

It is important to note that the method for determining the  $K$  value should be tailored and adapted to the specific problem at hand. In our case, the  $K$ -means algorithm is used to streamline data processing by clustering over a few ten thousand  $IV$  spectra into a manageable number of groups. From the experimental perspective, it is logical to set  $K$  equal to the number of distinct phases or structures anticipated in the sample. However, this approach often does not produce satisfactory results. Instead, it is more effective to use a substantially higher value for  $K$  and generate a manageable number of curve groups. These groups can then be refined by merging those with very similar (average)  $IV$  curves. Overall,  $K$ -means proves to be a valuable tool for processing LEEM- $IV$  data, offering significant time savings and improved clustering accuracy.

## 2.2 LEED

The contrasts in LEEM images cannot be understood without understanding the corresponding low energy electron diffraction (LEED) pattern of the sample. LEED is the most commonly used methods to obtain periodic information about crystalline solids or surfaces, which effectively convert a system's translation symmetry into a detectable diffraction pattern in reciprocal space. Due to the short inelastic mean free path (IMFP) of low-energy electrons within solids, the probing electrons are confined to the first few atomic layers of the surface. The combined measurement of LEED and LEEM hence gives simultaneous information of the sample in real and reciprocal space.

The reciprocal space is a mathematic interpretation of the periodically arranged real space through the Fourier transform, which converts the translational symmetry of the system into spatial frequencies. In a three-dimensional reciprocal space, any lattice vector can be given by

$$\bar{G}_{hkl} = h\bar{b}_1 + k\bar{b}_2 + l\bar{b}_3 \quad (2.1)$$

with integers  $(h, k, l)$  being the Miller indices, and  $\bar{b}_i$  the primitive translation vectors for the given Bravais lattice. To adapt to a two-dimensional problem like the solid surfaces, the equation 2.1 can be simplified with two components as  $\bar{G}_{hk} = h\bar{b}_1 + k\bar{b}_2$ .

The reciprocal lattice defined as the normal vectors of the family of parallel lattice planes of the given direct Bravais lattice. The mathematic definition of the primitive translation vectors  $b_i$  in reciprocal space is listed as following

$$\bar{b}_1 = 2\pi \frac{\bar{a}_2 \times \bar{n}}{A}, \quad \bar{b}_2 = 2\pi \frac{\bar{n} \times \bar{a}_1}{A}, \quad A = \bar{a}_1 \cdot \bar{a}_2 \times \bar{n} \quad (2.2)$$

where  $\bar{a}_1$  and  $\bar{a}_2$  are the primitive translation vectors of the real space, and  $\bar{n}$  the unit vector normal to the surface.

For any elastic scattering of low energy electrons on a 2D lattice, the process must obey the conservation law for both energy and momentum [146]. Therefore, the energy conservation can be given as

$$\bar{K}^2 = \bar{K}'^2 \quad (2.3)$$

with  $\bar{K}$  being the incident wave vector, and  $\bar{K}'$  the emerging wave vector.

The momentum conservation can be given as

$$\bar{K}' = \bar{K} + \bar{G}_{hk} \quad (2.4)$$

The reciprocal spots in three-dimensional space are transformed into infinite diffraction rods which are perpendicular to the sample surface plane in a two-



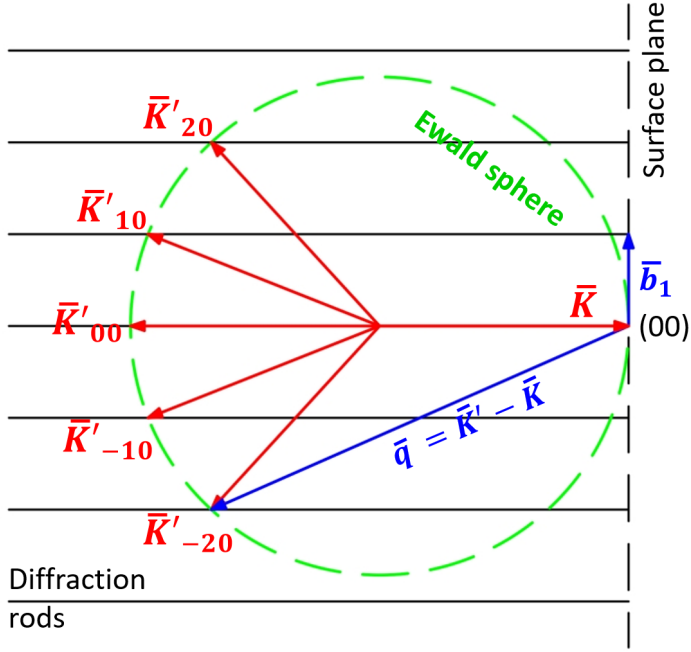


Figure 2.7: Construction of an Ewald sphere in reciprocal space.  $\bar{b}_1$  is the translation vector of a 2D reciprocal lattice. Momentum transfer  $q = \bar{K}'_{hk} - \bar{K}$ , with  $\bar{K}'_{hk}$  the emerging wave vector, and  $\bar{K}$  the incident wave vector.

dimensional problem. Fig. 2.7 displays the construction of an Ewald sphere to represent those equations (2.1-4). Constructive interference of electrons occurs where the Ewald sphere intersects the diffraction rods. At these intersection points, the in-plane momentum transfer  $\bar{q}_{\parallel}$  of the electrons equals a multiple of translation vector  $\bar{b}_1$  of the two-dimensional reciprocal lattice.

The operation in LEED mode of the LEEM instrument is achieved by projecting the diffraction plane onto the detector instead of the imaging plane. Additionally, an illumination aperture (IA) is needed to enhance the coherence of the electron beams and prevent the diffraction spots from becoming too intense. By using a small illumination aperture, a region as small as  $2\mu\text{m}^2$  on the surface can be illuminated by the electron beam, allowing for localized investigation via LEED. This technique is known as  $\mu\text{LEED}$ .

## 2.3 PEEM

The LEEM technique can be further expanded by utilizing different sources of low-energy electrons for imaging, such as photoemitted electrons, a method known as photon emission electron microscopy (PEEM). In our lab, we have two UV light sources available: a 100 W mercury (Hg) arc lamp from LOT-Oriel Group Europe and a Helium (He) gas discharge lamp, the HIS 14 HD, from Focus GmbH.

Mercury lamps emit light at several distinct wavelengths due to various electronic transitions in mercury atoms. One of the most common wavelengths is 254 nm, which corresponds to approximately 4.89 eV of energy. In our setup, the mercury lamp is typically combined with the PTCDA (3,4,9,10-Perylene Tetracarboxylic Dianhydride)/Ag(111) system for aligning the electron optics. Since PEEM mode does not require the illumination column, the alignment of the intermediate and imaging columns can be performed independently, and the illumination column is adjusted later, reducing the complexity of the process. The PEEM contrast in the the PTCDA/Ag system arises from the difference in the work functions of the Ag(111) surface (around 4.4 eV) and the PTCDA molecules (which range between 5 and 5.5 eV, depending on factors like surface cleanliness, molecular arrangement, and substrate interaction) [147–149]. As a result, photoelectrons are excited and can only be collected from the bare Ag surface, since their work function from the PTCDA islands is larger than their kinetic energy.

### ARPES (Angle-Resolved Photoemission Spectroscopy)

Photoelectrons can be captured from a surface, and projected either to an imaging plane (real space) or diffraction plane (reciprocal space). A more advanced version of PEEM can be achieved by using higher-energy photons for excitation, such as the FOCUS He lamp in our case, which emits photons with an energy of 21.2 eV. Additionally, our LEEM instrument is equipped with a hemi-spherical energy analyser. Owing to the almost 180° acceptance angle for electrons, the angular distribution of photoelectrons can be measured by switching from real-space imaging to reciprocal-space diffraction, similar to what ARPES does. This

## Chapter 2. Experimental Techniques

---

enables efficient constant-energy band structure mapping of a selected area on the surface. Since the selected area can be as small as a few squared micrometers, this technique is also referred to as  $\mu$ ARPES [150].

## 3 0°-Rotated Monolayer Epitaxial Graphene

**Chapter 3 and 4** report the successful growth of wafer-scale 30°-TBG on a 6H-SiC(0001) surface through epitaxial growth followed by hydrogen intercalation. The first of the two chapters focuses on the LEEM study of 0°-rotated epitaxial graphene on SiC, and the second addresses the 30°-TBG formed consistently across the entire sample after hydrogen intercalation.

In this chapter, we discuss the structure and morphology of graphene layers on 6H-SiC(0001) surface after the epitaxial surfactant-mediated growth [6], and how they are affected by the annealing temperature. In particular, results from two samples that were prepared at only slightly different temperatures (1330 °C and 1380 °C), but show fundamentally different morphologies, are presented. In the following discussion, graphene layers that are 0°-rotated relative to the substrate lattice is referred to as  $G-R0^\circ$ , and those that are 30°-rotated as  $G-R30^\circ$ . At the lower temperature, a homogeneous  $G-R0^\circ$  layer forms on the ZLG- $R30^\circ$ , whereas at the higher temperature, the ZLG- $R30^\circ$  decouples from the substrate. Although this decoupling is generally desirable for the development of TBG, since the ZLG is 30°-rotated relative to the substrate, forming a  $G-R30^\circ$  layer beneath the  $G-R0^\circ$  layer, it occurs inhomogeneously, leading to a surface with multilayer regions that vary in the number of layers.

The data and results presented in this chapter have been published in the paper: H. Yin, M. Hutter, C. Wagner, F. S. Tautz, F. C. Bocquet, and C. Kumpf, "Epitaxial growth of mono- and (twisted) multilayer graphene on SiC(0001)",

link: <https://doi.org/10.1103/PhysRevMaterials.9.044003>.

This work was conducted as part of the collaborative research center SFB 1083 "Structure and Dynamics of Internal Interfaces". My specific contributions included performing and analyzing LEED, LEEM, and LEEM-IV experiments. Sample preparation and ARPES measurements were carried out by Mr. Mark Hutter.

### 3.1 Sample Preparation

N-doped 6H-SiC(0001) wafers, purchased from SITUS Technicals GmbH, Germany, were used to prepare the samples discussed here. A schematic overview of the sample preparation using the surfactant-mediated growth method is shown in Fig. 3.1. Initially, the samples were degassed in UHV at 880 °C for 30 min. Then, the annealing temperature was increased to 1050 °C, with an external flux of Si atoms for another 30 min, leading to Si-rich reconstruction on the surface with a  $(\sqrt{3} \times \sqrt{3})R30^\circ$  pattern. Subsequent annealing at a lower temperature of 880 °C (also with external Si-atom supply) for another 30 min resulted in a Si-rich  $(3 \times 3)$  reconstruction on the surface. The presence of excess Si atoms on the SiC(0001) surface significantly reduces the evaporation rate of thermally decomposed Si atoms from the substrate, enhancing the uniformity of the graphene layer grown in the next step.

G-R0° was achieved by annealing the sample at a higher temperature in a borazine atmosphere with a partial pressure of  $1.5 \times 10^{-6}$  mbar for 30 min. The final annealing temperature was the only difference in the preparation of the various samples discussed in this work. Specifically, one sample, referred to as "low-T" in the following, was annealed at 1330 °C, while the other, "high-T" sample, was annealed at 1380 °C. LEED measurements were conducted to assess the sample quality after each preparation step. Following this, ARPES measurements were carried out in a UHV chamber directly connected to the preparation chamber. After completing the preparation, LEED, and ARPES measurements, the samples were transported through air to the LEEM instrument. Once in the LEEM chamber, the samples were reintroduced to UHV and outgassed at

### 3.2 Homogeneity and Electronic Structure

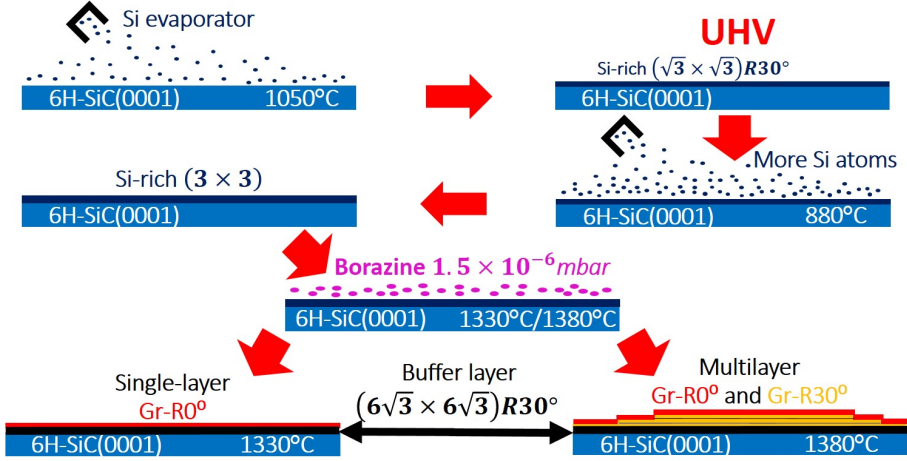


Figure 3.1: Schematic interpretation of the sample preparation via the surfactant-mediated growth method [6].

approximately 900 °C to remove any contaminants acquired during transport. LEED, performed by operating the LEEM instrument in diffraction mode, was used to confirm the good air-stability of the samples.

### 3.2 Homogeneity and Electronic Structure

A comparison of the two graphene samples in terms of surface homogeneity and electronic structure is illustrated in Fig. 3.2. Panels (a) and (d) of Fig. 3.2 show BF-LEEM images of the two surfaces, captured at 1.66 eV with a FoV of 30  $\mu\text{m}$ . The surface morphologies depicted are representative of areas extending over 200  $\mu\text{m}$  for both samples. It is evident that the surface of the low-T sample is more homogeneous compared to the high-T sample. In panel (a), parallel lines running across the FoV correspond to step edges, which separate the surface terraces of the SiC substrate and result from the combined effects of surface miscut and step bunching behavior [41, 151, 152]. Only a few defects, appearing as dark spots, are visible. In contrast, the high-T sample surface is more inhomogeneous, with numerous small structures changing in their brightness on a sub- $\mu\text{m}$  length scale. The step edges are still visible as faint

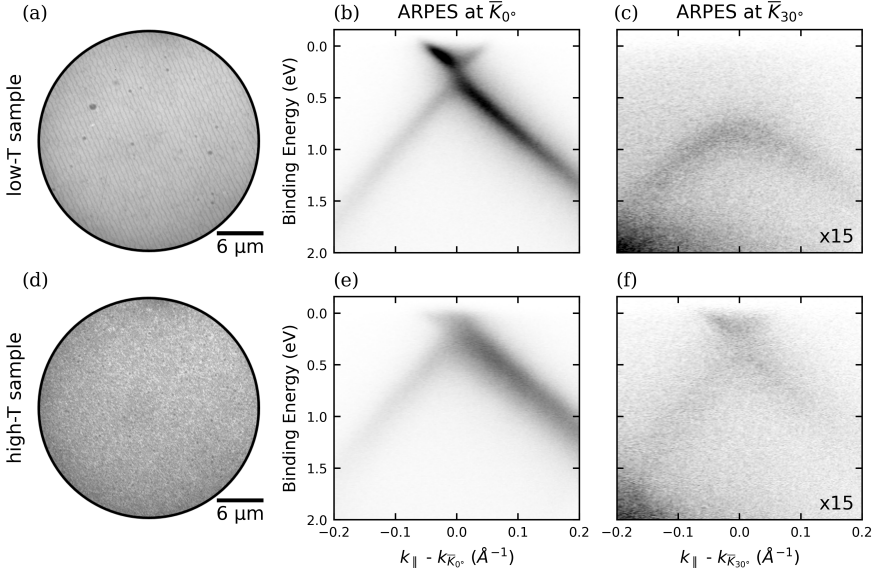


Figure 3.2: (a) BF-LEEM image captured from the low-T sample at the electron energy of 1.66 eV with a FoV of 30  $\mu\text{m}$ . (b) and (c) ARPES energy distribution maps (EDM) measured from the low-T sample along the  $\bar{\Gamma}\bar{K}$  direction close to the  $\bar{K}$  point of G- $R0^\circ$  and G- $R30^\circ$ , respectively. (d-f) Same as the (a-c) but for the high-T sample. The band intensity in (c) and (f) is enhanced by a factor of 15.

parallel lines but are more discontinuous and denser than on the low-T sample. Additionally, the high-T sample has a greater number of defects, which are also smaller than for the low-T sample.

The surface electronic band structure of the two samples is investigated with the ARPES technique, which also yields insight into the quality and orientation of the graphene layers. Fig. 3.2 (b) and (c) are energy distribution maps (EDMs) recorded from the low-T sample surface in the  $\bar{\Gamma}\bar{K}$  direction close to the  $\bar{K}$  point of G- $R0^\circ$  and G- $R30^\circ$  in the momentum space. The characteristic Dirac cone of the graphene is clearly visible in the panel (b), where the  $\bar{K}$  point of G- $R0^\circ$  is expected. The Dirac cone is shifted to a higher binding energy indicating that the surface is slightly n-doped. In panel (c), which displays the energy band around the  $\bar{K}$  point of G- $R30^\circ$  (rotated by  $30^\circ$  relative to the EDM in Fig. 3.2(b)),

### 3.2 Homogeneity and Electronic Structure

---

the Dirac cone is not observed. Instead, the band observed at approximately 1 eV binding energy corresponds to the  $G-R0^\circ$  band near its M-point. It should be noted that this band is very weak, with its intensity scaled up by a factor of 15 compared to Fig. 3.2 (b).

Fig. 3.2 (e) and (f) display the same measurements as in panels (b) and (c), but for the high-T sample. In panel (e), a Dirac cone is also visible at the  $\bar{K}_0^\circ$  position, suggesting that the high-T sample may be less n-doped than the low-T sample, as its Dirac cone is shifted slightly higher in energy. A Dirac cone is clearly observed at the  $\bar{K}_{30}^\circ$  position, indicating a significant coverage of  $G-R30^\circ$  on the surface. However, the intensity of the Dirac cone at the  $\bar{K}_{30}^\circ$  position is noticeably lower than at  $\bar{K}_0^\circ$ . This might indicate a smaller coverage of  $G-R30^\circ$  than of  $G-R0^\circ$ , but we certainly also expect the intensity shielding of photoemission from the  $G-R30^\circ$  by the  $G-R0^\circ$  layer, which is plausible, given that the epitaxial growth of graphene on the SiC surface is a bottom-up process, where  $G-R0^\circ$  forms first as the top layer, followed by the growth of  $G-R30^\circ$  layers starting from the underlying ZLG- $R30^\circ$ .

We can thus conclude that the low-T sample consists of  $G-R0^\circ$ , but no  $G-R30^\circ$ . We note that below the  $G-R0^\circ$ , a ZLG- $R30^\circ$  layer—covalently bound to the SiC substrate—must be present according to the surfactant-mediated growth mechanism of  $G-R0^\circ$  that has been studied in detail before [6]. Since this mechanism is self-limiting, we can also conclude that there is only one  $G-R0^\circ$  layer present on the low-T sample, although the data in Fig. 3.2 (b-c) do not allow to distinguish between one or more layers. Regarding the high-T sample, we conclude that  $G-R30^\circ$  is present below the  $G-R0^\circ$ , although the data discussed up to this point do not allow us to quantify this coverage (less than one layer, a single layer or even more than one layer, all presumably on a covalently bonded ZLG- $R30^\circ$  layer). In this respect, the morphology of the high-T sample turns out to be revealing (see below). Indeed, the most notable difference between the two samples is their morphology. This is already obvious from the LEEM images shown in Fig. 3.2 (a) and (d), but DF-LEEM and LEEM- $IV$  studies reveal many more details, as we discuss in the following two sections.



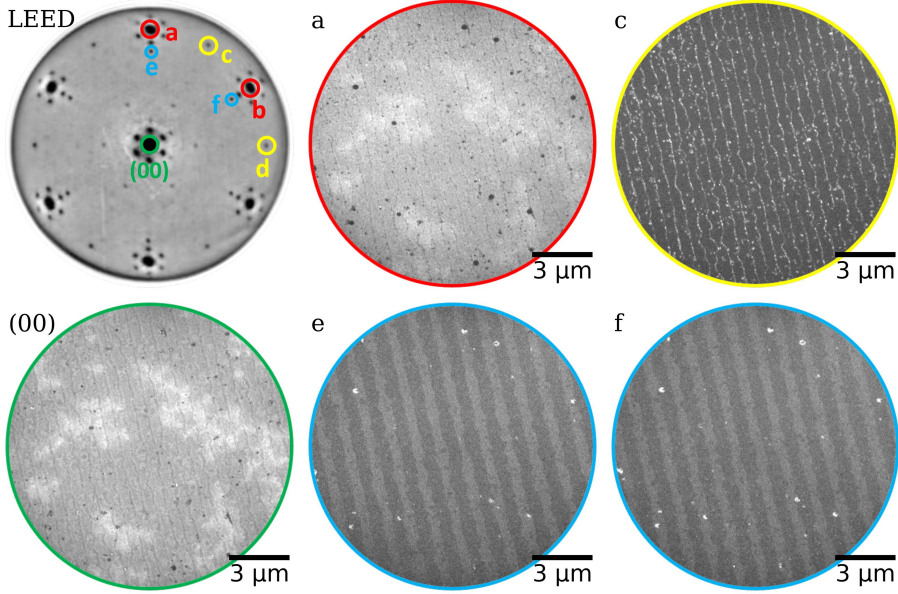


Figure 3.3: LEED pattern of the low-T sample, and corresponding bright-field (BF) LEEM image, labeled  $(00)$ , and dark field (DF) LEEM images, labeled  $a$ ,  $c$ ,  $e$ , and  $f$ . The labels of the LEEM images correspond to the diffraction spots marked in the LEED pattern. All LEEM images were obtained at an electron energy (start energy) of 55 eV.

### 3.3 Surface Morphology of the low-T sample

Fig. 3.3 shows the LEED pattern and several LEEM images obtained from the low-T sample surface. These were captured at an electron energy of 55 eV, with all LEEM images having a FoV of  $15\ \mu\text{m}$ . The LEED pattern contains diffraction spots from the substrate (two of which are highlighted by cyan circles and labeled as  $e$  and  $f$ ) and from G- $R0^\circ$  (highlighted by red circles and labeled as  $a$  and  $b$ ). The spots of these two structures are only radially displaced with respect to each other, indicating that the corresponding lattices are aligned (both have  $0^\circ$  orientation). A third set of diffraction spots, (two of them) marked by yellow circles and labeled as  $c$  and  $d$ , is rotated  $30^\circ$  relative to the substrate spots, with the same vector length as the G- $R0^\circ$  diffraction spots. Since ARPES measurements clearly reveals no G- $R30^\circ$  on the surface, this intensity must originate from the

### 3.3 Surface Morphology of the low-T sample

---

ZLG- $R30^\circ$ . Other visible spots likely arise from either the ZLG- $R30^\circ$ , which has a  $(6\sqrt{3} \times 6\sqrt{3}) R30^\circ$  reconstruction, or from multiple scattering effects [6].

Besides the LEED pattern, five LEEM images are shown in Fig. 3.3. The label in the top-left corner of each LEEM image corresponds to in the same way marked diffraction spots in the LEED pattern. The LEEM image labeled  $(00)$  is a BF-LEEM image that was captured from the main spot. This BF-LEEM image was taken at 55 eV, a much higher energy than the BF-LEEM image in Fig. 3.2 (a). At this energy, an additional brightness contrast, appearing in dendritic shapes, becomes visible. They appear only at specific electron energies and are not caused by multilayer formation, as revealed by the LEEM- $IV$  measurements discussed below.

The other four images in Fig. 3.3 are DF-LEEM images obtained from the different diffraction spots labeled in the LEED pattern. Images based on spots  $a$  or  $b$  (as well as  $c$  or  $d$ ) are pair-wise identical, as expected due to the six-fold symmetry of single-layer graphene. We hence show the DF-LEEM images for spots  $a$  and  $c$  only. The most intriguing aspect is the striking similarity between images  $(00)$  and  $a$  (including the dendrites), both of which are uniformly bright across the FoV, apart from a few thin dark lines and tiny spots. Considering also the image  $c$ , which is homogeneously dark, except for some bright lines and spots, it becomes evident that the surface is predominantly covered by G- $R0^\circ$ , while ZLG- $R30^\circ$  is only visible at small defects and possibly the step edges. This observation is consistent with the expectation that ZLG- $R30^\circ$  lies beneath the G- $R0^\circ$  layer. Additionally, the resemblance between images  $(00)$  and  $c$ , especially in terms of the dendritic brightness contrast, confirms that this contrast is unrelated to any rotation of the graphene layer.

DF-LEEM images originate from the substrate spots ( $e$  and  $f$ ) are not identical (as the cases for the graphene spots  $a$  and  $b$ , as well as  $c$  and  $d$ ), since the substrate SiC only shows three-fold symmetry. Instead, we observe bright and dark stripes in both images and a contrast inversion between  $e$  and  $f$ . The observation comes from the collective effect of substrate symmetry and step bunching behavior upon annealing [41, 151, 152]. As a result, the neighboring terraces are mirror-symmetric in their surface termination, which together with the three-fold

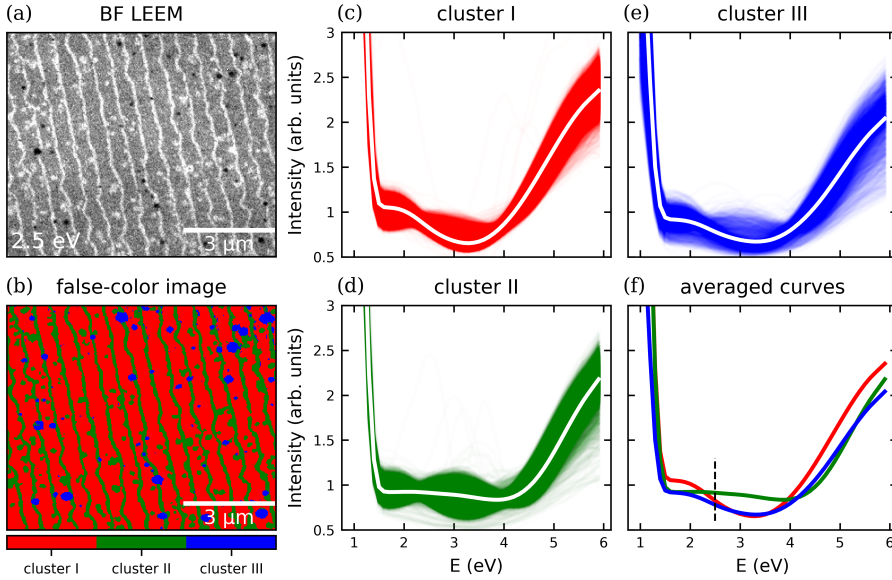


Figure 3.4: (a) Bright-field (BF) LEEM image of the low-T sample, recorded at 2.5 eV. LEEM-IV data (0 to 5.9 eV) have been recorded for this surface area ( $300 \times 250$  pixels) pixel-by-pixel and analyzed using the *K-means* algorithm (with  $K = 3$ ) described in the text. (b) False-color image representing the result of clustering the LEEM-IV data. (c-e) All LEEM-IV spectra belonging to each of the three clusters. Individual spectra are plotted with a transparency of 0.01. The white curves represent the average of all spectra in the respective cluster. (f) For clarity, the average curves from panels (c-e) are plotted in one diagram in their corresponding color. The dashed black line marks the energy at which the BF-LEEM image in panel (a) was recorded.

symmetry of the substrate produces the observed contrast inversion in the DF-LEEM images upon  $60^\circ$  rotation.

It has been demonstrated that, in the specific case of epitaxial graphene, the number of stacking layers corresponds to the number of minima observed in the IV spectra within the energy range of 0 to 7 eV [2, 38, 137, 138, 153]. LEEM-IV analysis was performed on the surface of the low-T sample, where BF-LEEM images were continuously captured over the energy range from 0 to 5.9 eV, with increments of 0.1 eV, i.e., at 60 different energies. A small region of  $9.0 \times 7.5 \mu\text{m}^2$

### 3.3 Surface Morphology of the low-T sample

---

is selected for the LEEM-*IV* analysis. One representative image taken at 2.5 eV is shown in Fig. 3.4 (a). At this energy, the terrace areas look quite uniform, and step edges have brighter contrast. Some defects that appear as bright and dark spots are also visible in the image.

LEEM-*IV* data is usually obtained by integrating the LEEM intensity within a user-defined homogeneous area, and the integrated intensity with respect to the energy is plotted. In such a way, one spectrum for each relevant area is obtained. For cases with large homogeneous areas, this method is unambiguous and convincing. But for samples that do not have clearly defined homogeneous regions (such as the one in Fig. 3.2 (d)), the selection of homogeneous surface areas by a human is prone to introduce bias. We therefore applied a generic way of extracting and analyzing the *IV* spectra that avoids any bias and allows an objective identification of regions on the surface in which the *IV* spectra are similar. In this approach, *IV* spectra are first extracted pixel-by-pixel from the entire data stack, i.e., for each pixel one individual LEEM-*IV* curve is obtained. In our case, with data collected at a resolution of  $300 \times 250$  pixels across 60 energy steps, this results in 75.000 individual  $I(E)$  curves.

In the next step, the curves are sorted based on specific criteria that are crucial for determining the clustering outcome. Various methods were explored, including manually identifying unique features in the profiles, such as particular curvatures or the number and positions of minima and turning points, that were then used for the classification—with moderate success. However, to enable an automated, model-free, and criteria-independent clustering process, we adapted the well-established *K-means* clustering algorithm [141], which is applied for grouping vectors into a given number  $K$  of clusters, the only free parameter of the algorithm. In this approach, the LEEM-*IV* data is first transformed into a 2-dimensional array of size  $(m \times n)$ , where  $m$  represents the total number of *IV* spectra, and  $n$  represents the number of data points in one *IV* spectrum. The algorithm considers each *IV* spectrum as a vector in a  $n$ -dimensional Euclidean space, where  $n$  is the number of data points (energies) of the *IV* spectra, i.e.,  $n = 60$  in our case. The algorithm then places all vectors (*IV* spectra) into clusters so that each of them belongs to the cluster with the nearest mean. Technically, the sum of the squared Euclidean distances of all vectors to their cluster's

### Chapter 3. 0°-Rotated Monolayer Epitaxial Graphene

---

mean is minimized.

In the third and final step, the classification result was visualized by marking pixels, the spectra of which belong to the same cluster with the same color, yielding a false-color image that very descriptively shows which domain or phase is present at which location on the surface. All the clustering operations were performed by python scripts. Detailed information like the packages and procedures implemented in the clustering process will be introduced in the appendix.

For the low-T sample, Fig. 3.4 (b) displays the result of the clustering with  $K = 3$ . Fig. 3.4 (c) to (e) show the large number of spectra in each cluster as a colored bunch of highly transparent curves. The white lines represent the average of all curves in each of the clusters; they are also plotted in Fig. 3.4 (f) in the color of their cluster. Overall, we find that all spectra are rather similar, even across the three clusters. With the possible exception of cluster II (see below), the spectra have one minimum and thus reveal that the corresponding regions on the surface are covered by precisely one decoupled graphene layer [2, 38, 137, 138, 153]. A more detailed analysis of the three clusters, to which we now turn, confirms this finding.

The characteristic features of the curves in cluster I are a shoulder between  $\sim 1.5$  eV and 2.0 eV and a relatively deep minimum at  $\sim 3.2$  eV. As mentioned above, these are the typical features of monolayer graphene on SiC [2, 28, 38, 138]. The false color image in Fig. 3.4 (b) indicates that cluster I represents the dominant structure on the surface that covers the terraces almost completely (red). In contrast to clusters I and III, the averaged spectrum of cluster II is essentially flat in the wide energy range from  $\sim 1.5$  eV and  $\sim 4.0$  eV, although the individual curves show various features—and even maxima and minima—in this region. This cluster is found along the step edges on the surface (green), and at some locations on the terraces where a bright defect is visible in the BF-LEEM image in Fig. 3.4 (a). The origin of this cluster is discussed in more detail in the next paragraph. The spectra in cluster III appear to be intermediate between those of clusters I and II: There is a clear minimum at  $\sim 3.2$  eV (like cluster I), but below 2 eV and above 4 eV, its average spectrum coincides with the one of

### 3.3 Surface Morphology of the low-T sample

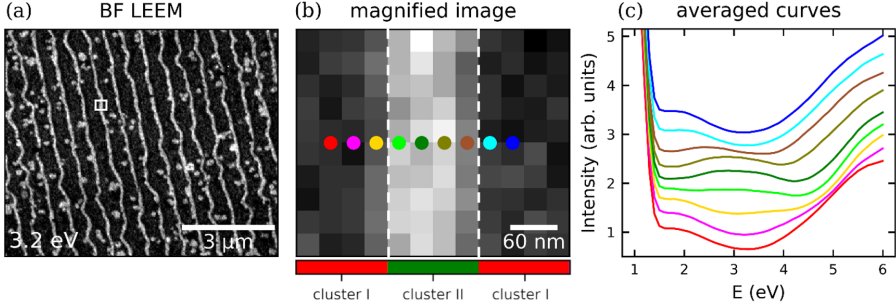


Figure 3.5: (a) Bright-field (BF) LEEM image of the same area as shown in Fig. 3.4 (a), but recorded at 3.2 eV; at this start energy, the contrast between step edges and terraces is more pronounced. (b) Magnified part of the image in panel (a), marked by a white rectangle in (a), showing a vertical step edge. The image size is  $360 \times 300 \text{ nm}^2$  ( $12 \times 10$  pixels). The colored dots mark nine columns (each containing 10 pixels) oriented parallel to the step edge. Red and green bars at the bottom of the image indicate to which cluster the pixels in the corresponding column have been assigned in the *K-means* analysis; vertical dashed white lines mark the borders between cluster I (red) and II (green). (c) Averaged LEEM-*IV* intensities from the marked columns in panel (b). Neighboring spectra are vertically displaced by 0.3. The color coding corresponds to the colored dots in panel (b).

cluster II (as shown in Fig. 3.4 (f)). The corresponding areas (blue) on the sample surface are small and match with the dark defects visible in the BF image in Fig. 3.4 (a). Note that at  $\approx 2.5 \text{ eV}$ , marked by the black dashed line in Fig. 3.4 (f), a clear contrast between all three clusters is visible. This is not the case for almost all other energies below 6 eV.

We now analyze cluster II in more detail. To this end, we trace the spectra and their changes across a step edge. Fig. 3.5 (a) displays the same surface area as Fig. 3.4 (a), but recorded at an electron energy of 3.2 eV to obtain a better contrast. Fig. 3.5 (b) shows a small section of the surface, marked in Fig. 3.5 (a) with a white rectangle. It is so strongly magnified that individual pixels appear as squares. A step edge is running through the image from top to bottom. In this area, we analyzed the change of the spectra across the step edge by averaging the pixels in the image column-wise, i.e., by summing up the intensities of 10 pixels

### Chapter 3. 0°-Rotated Monolayer Epitaxial Graphene

---

vertically. Performing this for the nine columns which are marked by colored dots in Fig. 3.5 (b), we obtained the nine spectra that are displayed in Fig. 3.5 (c). We observe a continuous change of the spectra across the step edge, from red via magenta, yellow, different shades of green, brown to cyan and blue. The first and last, red and blue, are almost identical and resemble the spectra of cluster I. In contrast, the dark green, olive and brown spectra clearly show *two* minima, one below 2 eV, the other shifting from  $\sim 4.3$  eV to  $\sim 3.8$  eV in the sequence from dark green to brown. Remarkably, these are the energies at which surfaces with *two* decoupled graphene layers exhibit their LEEM-*IV* minima (cf. Fig. 3.10 (a) below). It is clear that the superposition of spectra with one minimum at  $\sim 3.2$  eV and two minima, one to left and the other to the right, will yield the flat average spectrum that is characteristic of cluster II.

To put this finding into perspective, we note that the resolution of our microscope is better than 10 nm, while the size of one pixel in Fig. 3.5 (b) is 30 nm. Hence, our measurement is not resolution-limited in the sense that a (hypothetical) abrupt change of the *IV* curve at the step edge would be smeared out by the instrumental resolution. In other words, if the change in the spectra at the step edge was abrupt, we would see an immediate change from one column of pixels to the next; the step would appear to be only one pixel wide in the measurement. Evidently, this is not the case, we rather see a continuous change of the spectra in 4 or 5 neighboring pixel columns, i.e., on a length scale of approx. 120 nm to 150 nm. This implies that the continuous, steady change of the curve profile in Fig. 3.5 (c) must be real.

In the light of the above resolution argument, we conclude that the apparent two-layer signal in the step region in Fig. 3.5 (c) indeed indicates the local formation of bilayer graphene, i.e., a second decoupled graphene layer forms close to the SiC step edges. Having in mind that for the formation of graphene on SiC, Si atoms have to evaporate from the bulk surface, it is more plausible to assume that this process starts directly at the edge of the *upper* terrace rather than at the lower. Since the steps at the surface of a 6H-SiC(0001) crystal are rather high (three SiC bilayers, corresponding to half of the unit cell, that is 7.55 Å) evaporation of Si at the step edge is certainly favored compared to flat areas on the terraces. The lateral length-scale of this effect is in the order of 150 nm,

### 3.3 Surface Morphology of the low-T sample

---

indicating a moderate diffusion length for the Si surface species, assuming that they are desorbing at the edge of the upper terrace only. In this context it is notable that the two-layer signal in Fig. 3.5 (b) appears slightly off-centered; based on the model above, this must be towards the upper terrace. Although it is hard to say whether or not the  $G-R0^\circ$  layer overgrows the substrate steps as a continuous layer bending across the step edge, the DF-LEEM results shown above (image *a* in Fig. 3.3) clearly indicates that there is no (lateral) gap present in the  $G-R0^\circ$  layer, but the substrate steps are only visible as very faint dark lines. Hence, the  $G-R0^\circ$  is evidently present at both (upper and lower) sides right to the edge. Looking onto the surface from the top (along the incident electron beam), there is no gap detectable in the  $G-R0^\circ$  layer, making the traces of the step very faint in this DF image (Fig. 3.3 *a*). In the DF image using the  $G-R30^\circ$  reflections (Fig. 3.3 *c*), however, bright stripes are visible along the step edges, significantly wider than the faint lines in image *a*, indicating that the  $G-R30^\circ$  structure forms close to step (and only there) in addition to the already existing  $G-R0^\circ$  layer. Hence, what we observe at the step edges, is most likely the beginning of the decoupling of the ZLG- $R30^\circ$  layer, which transforms to a  $G-R30^\circ$  layer underneath the  $G-R0^\circ$  due to the formation of a new ZLG at the substrate's surface.

We finally discuss the nature of the two types of defects that are visible in the BF-LEEM image in Fig. 3.4 (a). The bright defects exhibit spectra that belong to the same cluster as those recorded at the step edges (cluster II, green). It is therefore very likely that we see a local TBG formation also at these defects, possibly induced by some contamination or structural defect in the substrate underneath the graphene layer. The dark defects were assigned to cluster III, based on the shape of their LEEM-*IV* curves, which is somewhat in between those of the typical  $G-R0^\circ$  (cluster I) and TBG (cluster II) shapes. However, since the contrast in the defects in the BF image (Fig. 3.4 (a)) is based on only one specific electron energy, and since in general clusters II and III have rather similar LEEM-*IV* curve shapes, the differentiation of the two types of defects may be exaggerated and to some extent arbitrary.

We conclude that the surface of the low-T sample is almost homogeneously covered by a uniform monolayer of  $G-R0^\circ$  (the fact that it is  $G-R0^\circ$  rather than



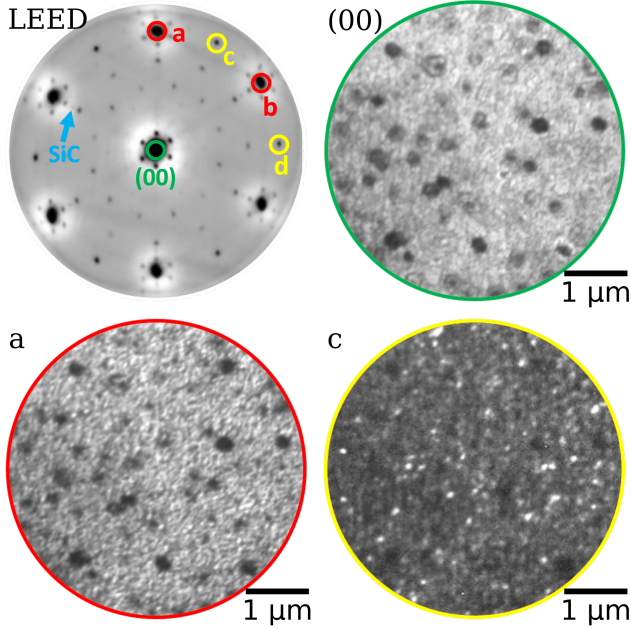


Figure 3.6: LEED pattern of the high-T sample, and corresponding bright-field (BF) LEEM image, labeled  $(00)$ , and dark field (DF) LEEM images, labeled  $a$  and  $c$ . The labels of the LEEM images correspond to the diffraction spots marked in the LEED pattern. All LEEM images were obtained at an electron energy (start energy) of 55 eV.

G- $R30^\circ$ , follows from DF-LEEM, see **Sec. 3.2**), in particular on all terraces. Along the step edges, and possibly also at some defects, we observe the beginning growth of  $30^\circ$ -TBG, indicated by DF-LEEM on the G- $R30^\circ$  reflections and the two-layer signature of the  $IV$  spectra. The length scale around the steps on which these effects can be observed, is  $\approx 150$  nm.

### 3.4 Surface Morphology of the high-T sample

We now turn to the discussion of the high-T sample. In the preparation procedure, the high-T sample was annealed to  $1380^\circ\text{C}$ ,  $50^\circ\text{C}$  higher than that of the low-T sample in the borazine atmosphere. Consequently, a completely differ-

### 3.4 Surface Morphology of the high-T sample

---

ent surface morphology was observed on the surface of high-T sample, i.e., an inhomogeneous growth of multilayer graphene.

Fig. 3.6 presents the LEED pattern, BF-LEEM image, and two DF-LEEM images obtained from the surface of the high-T sample. The diffraction spots of  $G-R0^\circ$  and  $G-R30^\circ$  (or possibly  $ZLG-R30^\circ$ ) are visible in the LEED pattern, two of the  $G-R0^\circ$  spots are marked by the red circles, while two of the  $G-R30^\circ$  by the yellow circles. Around the  $(00)$  main spot marked by a green circle, there are six satellite spots, which originate from the  $(6\sqrt{3} \times 6\sqrt{3}) R30^\circ$  reconstruction of the ZLG. At higher  $k_{||}$ , there are two additional rings of diffraction spots, and each consisting of 12 spots. A similar LEED pattern was reported by Ahn *et al.* [104], who discussed these spots as a 12-fold symmetric pattern originating from the quasi-crystalline properties of a  $30^\circ$ -TBG.

In this pattern, the intensity of the substrate SiC spots is much lower than the others. One of the substrate diffraction spots is indicated by the cyan colored arrow. DF-LEEM imaging is not possible from such low intensity of the substrate spots, which is a first hint for the presence of multiple graphene layers on the surface.

DF-LEEM images were captured from the diffraction spots of graphene, with image *a* from the  $G-R0^\circ$  spot, and image *c* from the  $G-R30^\circ$  spot. Due to the six-fold symmetry of graphene layers, only two images are shown in the Fig. 3.6, the same case as to the low-T sample. Image  $(00)$  is a BF-LEEM image, recorded using the  $(00)$  main beam. Compared to the surface of the low-T sample, all the three images reveal a much more inhomogeneous surface morphology on the high-T sample with a lot of small objects randomly distributed. The similarity between the BF-LEEM image  $(00)$  and the DF-LEEM image *a* is remarkable, indicating that the  $G-R0^\circ$  layer is present everywhere on the sample (similar to the low-T sample). The fact that image *a* is much brighter than image *c* indicates that the  $G-R0^\circ$  is the top layer, located above the  $G-R30^\circ$  and/or  $ZLG-R30^\circ$  layers (which are also present on the surface, see the LEED image in Fig. 3.6), with the exception of a few locations on the surface that appear as bright spots in image *c*. However, the overall intensity in image *c* is not zero, but at an intermediate level, therefore,  $G-R30^\circ$  and/or  $ZLG-R30^\circ$  must be present on the entire sample

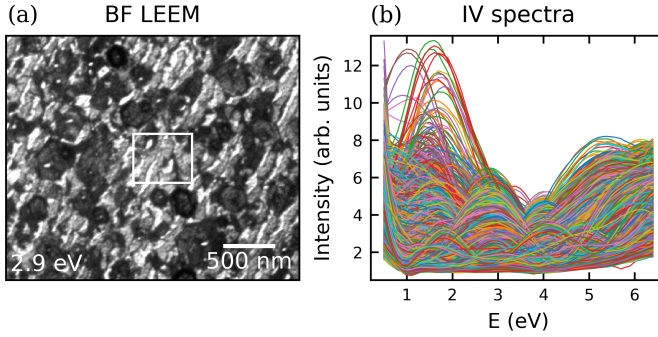


Figure 3.7: (a) Bright-field (BF) LEEM image of the high-T sample ( $\approx 3.0 \times 2.5 \mu\text{m}^2$ ,  $300 \times 250$  pixels, 2.9 eV). The white rectangle marks the area that is magnified in Fig. 3.10. (b) All LEEM-IV spectra that were recorded on the surface area imaged in panel (a). The color coding in panel (b) is arbitrary. In Fig. 3.8, these LEEM-IV spectra are clustered.

surface (in contrast to the low-T sample).

To understand the LEEM images obtained from the surface of the high-T sample, the key question is to figure out the origin of the inhomogeneities that are clearly visible in both BF- and DF-LEEM images. To achieve that, the similar pixel-by-pixel analysis of LEEM-IV spectra is performed on the high-T sample. The surface region, from where the IV spectra were extracted is shown in Fig. 3.7 (a) with an area of  $3.0 \times 2.5 \mu\text{m}^2$  ( $300 \times 250$  pixels). The total 75.000 curves are plotted in one diagram in Fig. 3.7 (b). It is obvious that the extracted spectra are divers in their contour and oscillations, in particular in the number of minima, which indicates number of graphene layers in this region. In the *K-means* analysis that follows, we therefore place great emphasis on identifying the number of minima in the spectra.

Since the number of different clusters is prior unclear, we started the *K-means* based analysis with a value of 15. However, the clustering result turns out not conclusive. In principle, *K-means* suits well for clustering curves with complex shapes, but since the algorithm defines "similar shapes" with the distance in Euclidean space that is calculated from intensity values, the curves were grouped together for an overall similar intensity, but not for the number and position

### 3.4 Surface Morphology of the high-T sample

---

of minima. Therefore, a small  $K = 15$  value fails in our case, because too many spectra with small Euclidean distances but different numbers of minima were grouped together. The issue was solved by increasing the  $K$  value to 100. A larger number of the grouped clusters results in a smaller variance within each cluster. In a such way, the impact on the clustering from a similar overall intensity of curves becomes less, while the number and position of minima of curves become decisive. After *K-means* did its job, 100 small curve bunches (or clusters) with clear numbers of oscillations and steady minima positions are generated. Subsequently, a careful manual sorting of the clusters is necessary, in order to identify groups of spectra with an identical number of minima. Those have to be grouped together manually, which, at a number of 100, is a reasonable task compared to the 75.000 single curves.

The final result of this semi-automatic analysis is shown in Fig. 3.8 (a): Five clusters with a clear number of oscillations allow an unambiguous counting of minima, and one cluster relatively flat contour. We interpret this last cluster with flat curves as regions with more than five layers, since the minima in the spectra get so shallow in this case that they cannot be resolved any more. A similar situation was reported earlier for multilayers of graphene on Pt(111), see Ref. [154]. Therefore, it is plausible that we believe those curves with a flat contour corresponding to the surface areas with a coverage of more than five graphene layers. The false-color image of the relevant surface area shown in Fig. 3.8 (c) displays the results. There is also a small fraction of the curves (6.0%) with irregular shapes that do not fit any clusters shown in Fig. 3.8 (a). They are labeled "unidentified", and represented as gray colored areas in Fig. 3.8 (c), although they in turn can be divided into four sub-clusters, see Fig. 3.11.

Before turning to a detailed discussion of the surface morphology of the high-T sample based on the false-color map in Fig. 3.8 (c), we consider an alternative to the semi-automatic, *K-means* based classification discussed above. Considering the large number of spectra, a purely manual classification according to the number of minima is clearly out of question. However, a classification on the basis of a small number of *a priori* defined criteria turned out to be successful. In the present case, these criteria are the number and the positions of the minima in the spectrum. For instance, for the decision whether a given spectrum

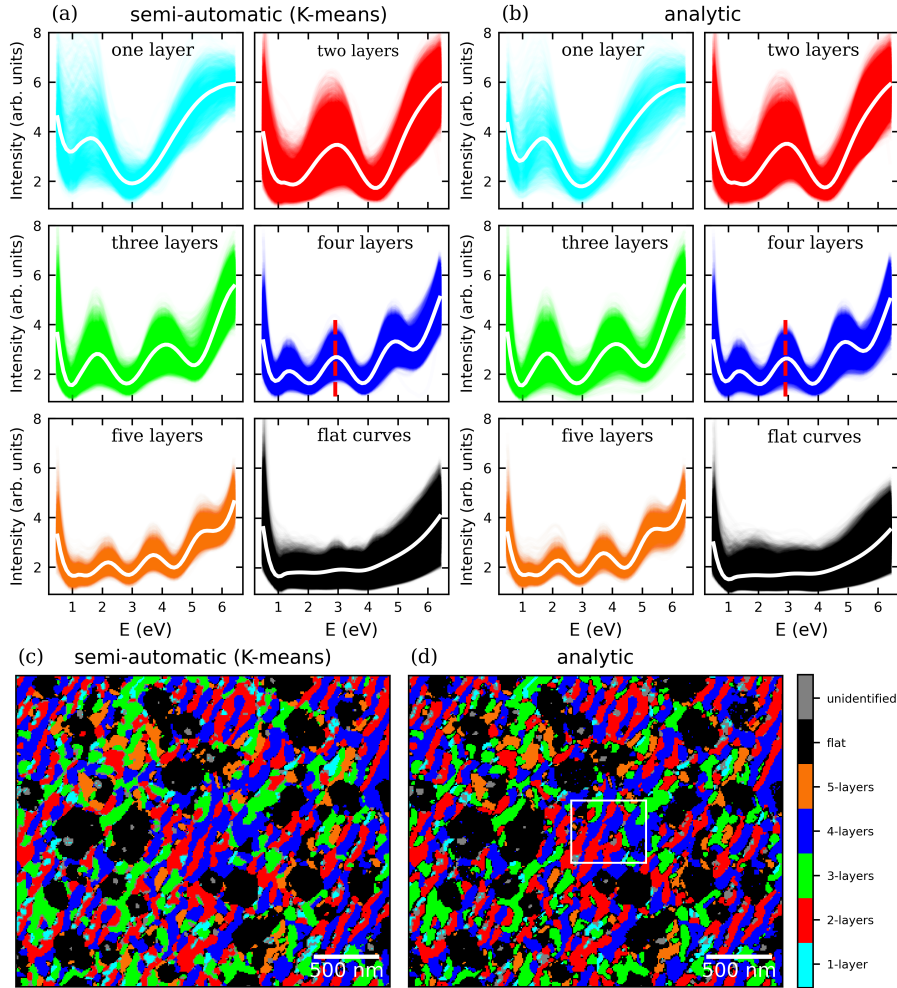


Figure 3.8: Results of the clustering of LEEM-IV spectra recorded on the high-T sample for (a,c) the semi-automatic analysis based on the *K-means* algorithm, and (b,d) an analytic classification based on *a priori* defined criteria. For more details, see main text. (a,b) Clusters of spectra for six different classes, originating from graphene stacks consisting of one, two, three, four, five and more than five layers. Individual spectra are plotted with a transparency of 0.01. The white curves represent the average of all spectra in the respective cluster. (c,d) False-color images representing the result of clustering the LEEM-IV data. The corresponding bright-field (BF) LEEM image is shown in Fig. 3.7 (a).

### 3.4 Surface Morphology of the high-T sample

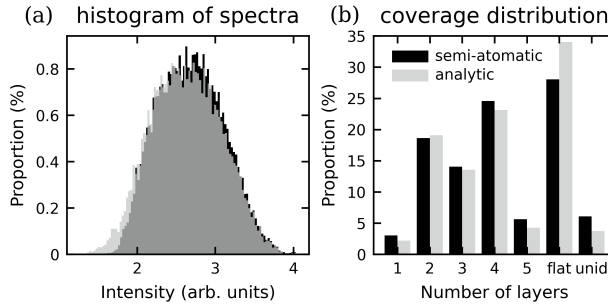


Figure 3.9: Results of the clustering of LEEM-*IV* spectra of the high-T sample for the semi-automatic (black) and the analytic method of data analysis (gray). (a) Histogram of the LEEM intensity of the four-layer clusters at a start energy of 2.9 eV, as marked by red dashed lines in Fig. 3.8 (a) and (b). The bin size on the intensity axis was 0.03. The histogram was normalized to a total area of 1. In the dark gray area the histograms of both methods overlap. (b) Proportion of the different regions (1, 2, ..., 5 layers, more than 5 layers (flat) and unidentified) of the total surface area, according to Fig. 3.8 (c) and (d).

should be assigned to the two-layers class, the code looked for (exactly) two minima, one located between 1.2 and 1.5 eV, the other between 4.0 and 4.3 eV. Evidently, this analytic mode of classifications is not prone to false assignments due to a diffuse similarity between spectra, because it relies exclusively on the relevant criteria which are clearly defined from the outset. On the other hand, the semi-automatic classification has the advantage of being model-free, but in the present case it needs a grossly exaggerated number of clusters to start with, followed by a refinement step, in which the clusters obtained by *K-means* are combined into physically meaningful classes. In the analytic classification scheme, this physical meaning is introduced *a priori* by defining physically motivated criteria. In terms of efficiency, the *K-means*-based classification turned out to be superior in the present case.

Comparing the results of the semi-automatic with the analytic approach, we observe an excellent agreement between the two, both in the clusters of spectra (Figs. 3.8 (a) and (b)) and in the false-color images in Fig. 3.8 (c) and (d). Only marginal differences appear. For example, in the clusters of spectra belonging to the one-layer and flat-curves classes, the variance varies slightly between

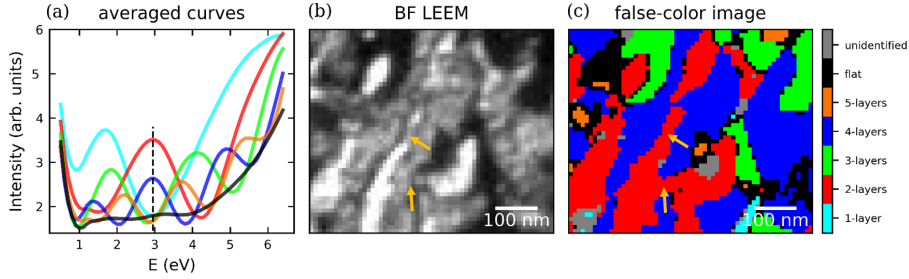


Figure 3.10: Results of the clustering (using the analytic approach) of LEEM-*IV* spectra recorded on the high-T sample: (a) Averaged spectra for each of the classes in Fig. 3.8 (b). (b) Magnification of the marked section (white rectangle) in the bright field (BF) LEEM image in Fig. 3.7 (a). (c) False-color image representing the result of the clustering of LEEM-*IV* spectra for the sample area shown in (b), also the magnified image of the region marked by a white rectangle in Fig. 3.8 (d).

Figs. 3.8 (a) and (b). However, at most energies, histograms across the clusters of spectra in each class are uni-modal symmetric, which proves an appropriate classification of the spectra in both methods. This is illustrated in Fig. 3.9 (a) for the four-layers class at 2.9 eV (red dashed line in Fig. 3.8 (b)).

Fig. 3.9 (b) illustrates the distribution of the spectra, representing the relative surface coverage of structures corresponding to the different clusters. We conclude that both methods yield comparable results, each with its own advantages and disadvantages. The semi-automatic *K-means* approach offers the advantage of being model-free, although some tuning of the first results is required to group them into physically meaningful categories. In contrast, for the analytic analysis this "physical meaning" is introduced beforehand, by defining the criteria for clustering, number and position of minima in our case. In terms of time and efficiency, the *K-means* method appears to be more advantageous.

As a cross check, we compare the LEEM-*IV* false-color maps with BF-LEEM images. In Fig. 3.10 (a) the averaged *IV* spectra of the six classes from Fig. 3.8 (b) are plotted in a single graph. The data were taken from the analytic approach, but the curves would not differ significantly if they had been taken from the semi-automatic analysis. The plot once again reveals that the amplitudes of

### 3.4 Surface Morphology of the high-T sample

---

the intensity oscillations decrease with increasing number of layers. More importantly, it also explains the contrast in the BF-LEEM images in Figs. 3.7 (a) and 3.10 (b), the latter being a magnified section of the former. At the energy at which the BF image was recorded (2.9 eV, black dashed line in Fig. 3.10 (a)), the two- and four-layer spectra have maxima, the one of the two-layer spectrum being more intense. All other curves exhibit a minimum at this energy. It is therefore clear that in the BF image the two-layer regions should appear brightest, while those with four layers should exhibit intermediate brightness and all other regions should be dark. This is precisely what is observed if we compare the false-color image from LEEM-IV (Fig. 3.10 (c)) with the BF-LEEM image (Fig. 3.10 (b)): The correspondence is almost one-to-one for these three brightness levels. Only in a few small regions (two are marked by orange arrows), mostly located between regions for which the assignment is unambiguous, the LEEM-IV analysis reveals the number of layers more clearly than the BF-LEEM contrast. This is of course due to the fact that the LEEM-IV analysis is based on a full three-dimensional data stack  $I_{x,y}(E)$ , which as such is able to yield more information than a single BF-LEEM image at one specific energy, even if this energy is well selected in terms of maximizing the contrast between different multilayer regions. We can thus conclude that Fig. 3.10 reveals overall consistency between BF-LEEM images and the clustering analysis of LEEM-IV data.

As mentioned earlier, the "unidentified" spectra in the semi-automatic clustering analysis of the high-T sample can be further categorized into four sub-clusters, which are illustrated in Fig. 3.11. Four sub-clusters are plotted individually in panel (c-f), and the corresponding false-color image is shown in panel (h). Comparing with the false-color image of Fig. 3.8 (c), it becomes evident that these "unidentified" regions are primarily located at the boundaries of areas with varying numbers of stacking layers and at the centers of the "flat curve" regions. The distributions of the individual sub-clusters are located close to each other in small groups, but the groups spread over the entire surface, as shown by the distinct, non-mixing colored pixels in panel (h). This suggests that their complex contour arises due to the boundary effects between different domains.



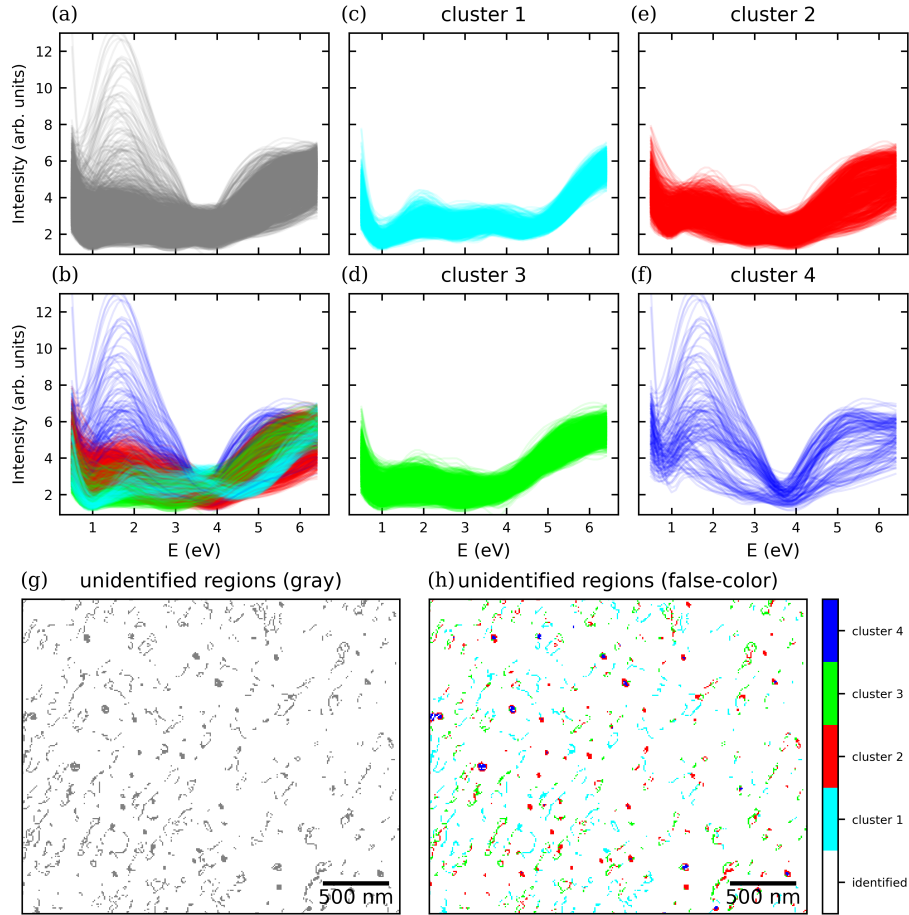


Figure 3.11: LEEM-IV spectra and false-color images of the "unidentified" regions found in the semi-automatic (*K-means*) analysis of the high-T sample (compare with Fig. 3.8). (a) All IV curves of the unidentified regions, plotted in gray with a transparency of 0.01. The unidentified regions can be divided in four clusters, as shown in (c-f), according to the shape of their IV curves. (b) Same as (a), but all curves plotted in their respective false-color as defined in (c-f). (g) and (h): Areas on the surface corresponding to unidentified regions, plotted as gray and false-colored areas, respectively. The shown surface area corresponds to Fig. 3.8 (c).

### 3.5 Conclusion

The surface morphology of two  $G-R0^\circ$  samples, prepared via the "surfactant-mediated epitaxial growth" method, was investigated using LEEM and related techniques. For an annealing temperature of  $1330^\circ\text{C}$  in borazine atmosphere, we found the formation of graphene in an unusual orientation of  $0^\circ$  on  $\text{SiC}(0001)$ ,  $G-R0^\circ$ . A central motivation of our work was the question whether or not the  $\text{ZLG-}R30^\circ$  underneath this  $G-R0^\circ$  layer can be decoupled from the surface by annealing at slightly higher temperatures,  $1380^\circ\text{C}$ , since this would result in a decoupled  $30^\circ$  twisted bilayer graphene ( $30^\circ$ -TBG).

On both surfaces, a  $0^\circ$ -rotated graphene layer, which is aligned with the  $6\text{H-SiC}(0001)$  lattice of the substrate, was observed. However, annealing in a borazine atmosphere at different temperatures resulted in distinct surface morphologies. The low-T sample, annealed at  $1330^\circ\text{C}$ , exhibited a homogeneous single-layer  $G-R0^\circ$  across the surface. While we cannot unambiguously say whether or not the  $G-R0^\circ$  layer overgrew the substrate step edges, we see clear indications for a beginning formation of a (decoupled)  $G-R30^\circ$  layer in a  $\sim 150\text{ nm}$  wide stripe along the step edge, most probably on the upper terrace. Confirmed by both the shape of the LEEM-*IV* spectra and by DF LEEM we see both  $G-R0^\circ$  and  $G-R30^\circ$  in this area. In other words, we observe the start of  $30^\circ$ -TBG growth at the step edges, already at a temperature of  $1330^\circ\text{C}$ . However, the majority of the surface area is still covered by the high-quality  $G-R0^\circ/\text{ZLG-}R30^\circ$  stack, with only a low density of point defects.

The high-quality and flat morphology of the  $G-R0^\circ/\text{ZLG-}R30^\circ$  stack suggests the possibility to grow TBG at slightly elevated temperatures at which the  $\text{ZLG-}R30^\circ$  is known to convert to  $G-R30^\circ$ . We tested this concept by annealing  $\text{SiC}(0001)$  in borazine atmosphere at  $1380^\circ\text{C}$ , i.e., only  $50^\circ\text{C}$  higher than the temperature that leads to the high-quality  $G-R0^\circ/\text{ZLG-}R30^\circ$  stack. This experiment has been partially successful. Because the uppermost layer across the complete high-T sample was still  $G-R0^\circ$ , and since all graphene layers that grow below this are of type  $G-R30^\circ$ , the complete high-T sample was indeed covered with a twisted  $G-R0^\circ/G-R30^\circ$  stack. However, the morphology of this sample was far from that of an ideal TBG stack. The high-T sample rather exhibited a patchwork of small re-

### Chapter 3. 0°-Rotated Monolayer Epitaxial Graphene

---

gions with different numbers of G- $R30^\circ$  layers below G- $R0^\circ$ . Up to five graphene layers could be identified, but there were regions on the sample which probably consisted of even more layers. In fact, this complex sample morphology posed a considerable challenge to our LEEM analysis, which we mastered by analyzing LEEM- $IV$  data pixel-by-pixel. This allowed the unambiguous identification of the number of layers on the surface, with a lateral resolution of  $\approx 10$  nm, corresponding to a single pixel in the current setup.

We thus found that, while the borazine surfactant-mediated growth of G- $R0^\circ$  graphene monolayers is a self-limiting process, this does not apply to the growth of additional G- $R30^\circ$  layers below the G- $R0^\circ$ . Even at  $1330^\circ\text{C}$ , we find traces of the beginning G- $R30^\circ$  growth at the step edges. At slightly higher temperatures  $1380^\circ\text{C}$ , G- $R30^\circ$  multilayers grow in an uncontrolled manner, producing a very complex morphology. This growth of G- $R30^\circ$  is not only influenced by temperature, but also by time. In additional experiments at similar temperatures and longer annealing times we saw the multilayer areas growing with time. In particular, in all cases multilayer regions with more than two layers started to evolve before the bilayer regions have spread all over the terraces. We therefore have to conclude that the thermal growth of high-quality TBG appears to be not possible, since the multilayer growth (with more than two graphene layers) starts before a homogeneous TBG sample can be obtained. As a consequence, we conclude that decoupling the  $30^\circ$ -rotated ZLG by intercalation with a suitable atomic species may be a better strategy to obtain TBG on SiC(0001) than simple annealing in borazine atmosphere. One obvious candidate for intercalation is hydrogen. We hence report the preparation  $30^\circ$ -TBG by hydrogen intercalation of the ZLG- $R30^\circ$ /SiC(0001) underneath G- $R0^\circ$  in the next chapter.

## 4 30°-TBG via Hydrogen Intercalation

Hydrogen intercalation of epitaxial graphene on SiC substrates has attracted significant interest over the past decade due to its ability to produce quasi-freestanding mono- and bilayer graphene with enhanced flexibility and superior electronic properties compared to conventional epitaxial graphene.

In this chapter, quasi-freestanding twisted bilayer graphene with a 30° twist angle is achieved on a 6H-SiC(0001) surface via hydrogen intercalation. The process is carried out in steps, enabling the observation and analysis of intermediate stages using low energy electron microscopy (LEEM). Initially, 0°-rotated monolayer graphene is formed on top of 30°-rotated zeroth-layer graphene (ZLG) using the surfactant-mediated epitaxial growth methods discussed in the last chapter for the low-T sample [6]. The introduction of hydrogen atoms physically and chemically decouples the ZLG from the SiC substrate, resulting in the formation of quasi-freestanding TBG. The 30° rotation and bilayer stacking configuration of the graphene layers are confirmed through LEED, LEEM-IV, and ARPES measurements after hydrogen intercalation. Moreover, the de-intercalation process of graphene sample was followed in-situ and in real time with the LEEM technique, which reveals the mechanism and behavior of the hydrogen atoms with respect to the intercalation process. In this chapter, all sample preparation, data collection and data analysis was performed by myself, except for the ARPES experiment discussed in **Sec. 4.3**, which was performed by Dr. Andrey Matetskiy, and data analysis was done by myself.

### 4.1 Sample Preparation

To perform the intercalation, a hydrogen atomic beam source (HABS 40-S-2208741) from MBE-Komponenten GmbH was directly attached to the LEEM chamber, with the cracking capillary positioned ~25 cm away from the sample, and tilted 60° with respect to the sample normal direction. This relatively long distance allows for a rather low intercalation rate, enabling the investigation of the sample surface at various intermediate stages of the intercalation process. The cracking capillary was operated at around 1740 °C, with a heating current of 12.73 A, and a water cooling of 60 l/h, which generates cracking efficiency of approximate 60%. The sample was annealed at around 640 °C in the LEEM chamber while being exposed to the external hydrogen atomic flux, with the hydrogen partial pressure in the chamber maintained at  $7.5 \times 10^{-6}$  mbar. The intercalation was carried stepwise over a total duration of 10.5 hours, and the surface investigated after 3 and 6 hours. For these intermediate investigations, and also after the end of the intercalation, the sample was cooled to room temperature. The chamber was pumped for 24 hours to reduce the hydrogen pressure, and the sample was degassed by annealing at 650 °C for 1 hour.

### 4.2 Pristine Surface before Intercalation

0°-rotated monolayer graphene was first prepared via the surfactant-mediated epitaxial growth method as discussed in the last chapter. After completing the preparation, the sample was transported through air to the LEEM instrument. In the LEEM chamber, the sample was thoroughly degassed by annealing at the temperature of 900 °C for 1 h. LEEM, LEED, and LEEM-IV measurements confirm the 0° rotation, and monolayer configuration of the graphene layer on the sample surface.

Fig. 4.1 (a) presents the LEEM image of the sample surface, which was captured at 0.66 eV. At this energy, the surface looks homogeneous, and the step edges appear as bright lines going across the field of view. The terrace areas are less bright than the step edges, and no defects are visible in the observed area. Compared to the "high-T" sample discussed in the previous chapter, the terraces

## 4.2 Pristine Surface before Intercalation

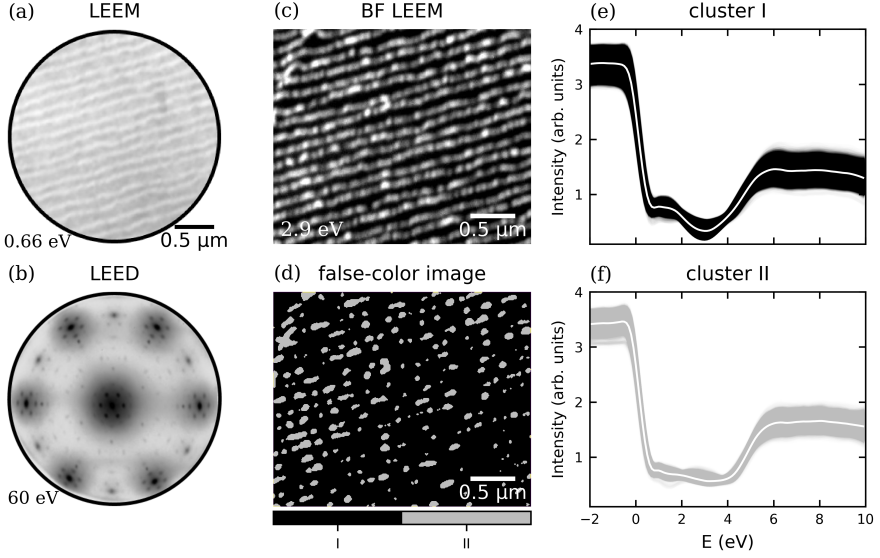


Figure 4.1: (a) LEEM image captured at 0.66 eV from the surface before intercalation. (b) LEED pattern obtained at an electron energy of 60 eV. (c) BF-LEEM image of a small area on the surface, recorded at 2.9 eV with a size  $\approx 3.0 \times 2.5 \mu\text{m}^2$  ( $300 \times 250$  pixels). LEEM-*IV* data in the energy range from  $-2$  to  $10$  eV have been recorded for the area and analyzed with the pixel-by-pixel method. (d) False-color presentation of the result of the LEEM-*IV* analysis. (e,f) Two curve clusters obtained through the pixel-by-pixel analysis. All curves are plotted with a transparency of 0.01, and the white curves in the middle represent the average of all spectra allocated to the respective cluster. Panel (b), and (c,f) share the same color codes.

on this sample are slightly narrower, as it originates from a different SiC wafer.

The LEED pattern obtained at an electron energy of 60 eV is shown in Fig. 4.1 (b). As previously discussed for the LEED pattern shown in Fig. 3.3, the diffraction spots of the  $G-R0^\circ$ ,  $G-R30^\circ$  or ZLG, and the substrate SiC can be identified, confirming the existence of  $G-R0^\circ$  on the surface. However, compared to the LEED pattern in Fig. 3.3, additional spots are visible in Fig. 4.1 (b). There are 24 spots arranged in two concentric circles, each containing 12 spots, which come from the Moiré pattern formed due to the overlapping of the top  $G-R0^\circ$  on the  $ZLG-R30^\circ$ . Those spots are also visible in Fig. 3.6 "LEED". Their appearing

## Chapter 4. 30°-TBG via Hydrogen Intercalation

---

in the pattern could be attributed to the energy difference between the LEED measurements, with one taken at 55 eV and the other at 60 eV.

We have also recorded LEEM-*IV* data within a small area of the surface in order to perform the pixel-by-pixel analysis and determine the stacking configuration of the layer(s). *IV* data were collected in the energy range from  $-2$  to  $10$  eV with an energy step of  $0.1$  eV. The BF-LEEM image of the surface area from where the *IV* data were extracted is displayed in Fig. 4.1 (c). It has a dimension of  $\approx 3.0 \times 2.5 \mu\text{m}^2$  ( $300 \times 250$  pixels). The image was taken at  $2.9$  eV, at which the terrace areas appear much darker than the step edges. Subsequently, the extracted curves are sorted into two clusters by the analytic method according to their contours (with a deep minimum located in the energy range  $2.8$  eV to  $3.1$  eV), and the clustering results are displayed as two curve bunches shown in Fig. 4.1 (e) and (f), with different color codes. All curves are plotted with a transparency of  $0.01$ . The bright line in the middle of two curve bunches represents the average of each cluster.

A spatial representation of the clustering results is given in Fig. 4.1 (d) as a false-color image, which shares the same color codes as the panel (e) and (f). A single minimum in the energy range of  $0$  to  $7$  eV of the curve bunch labeled as "cluster I" indicates the monolayer stacking configuration, corresponding to the dark terrace area in panel (c) and (d). The curve average of the "cluster II" appears relatively flat in the energy range from  $1$  to  $4$  eV, which is due to the continuously changing contours of the *IV* spectra when moving across the step edges. This effect has been discussed in detail in **Chapter 3**, in context with Fig. 3.5. The brightness interruption at the step edges is likely due to the local formation of  $30^\circ$ -TBG as discussed previously.

### 4.3 Intercalation of the Layers in Three Steps

We have investigated the sample surface after three subsequent hydrogen intercalation steps. For comparison, BF-LEEM images and LEED patterns obtained after each step are presented in Fig. 4.2. Panels (a) and (b) show results after 3 hours, (c) and (d) after 6 hours, and (e) and (f) after 10.5 hours. After 3 hours of

### 4.3 Intercalation of the Layers in Three Steps

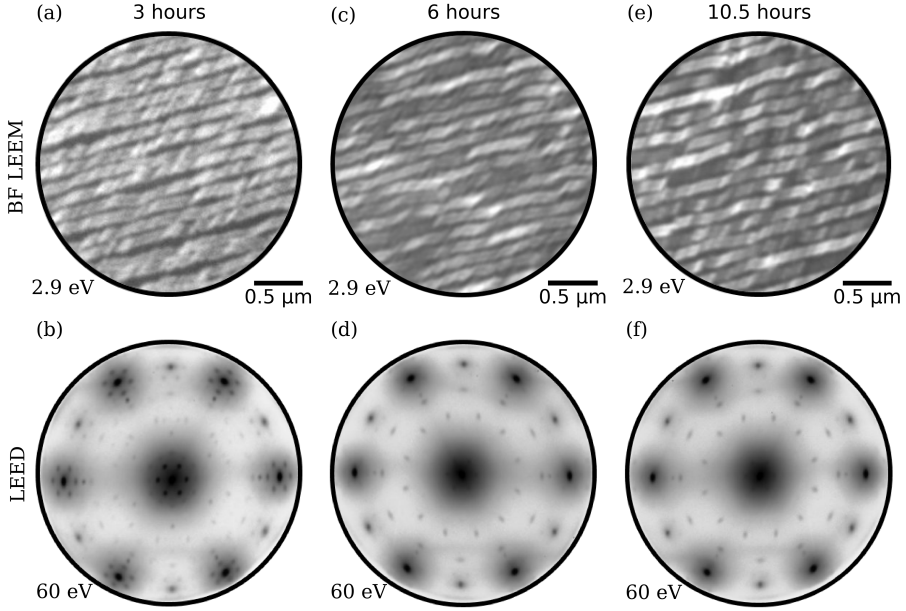


Figure 4.2: BF-LEEM images, and LEED patterns measured from the sample surface at different stages of the hydrogen intercalation, with (a,b) being after 3 hours, (c,d) being after 6 hours, and (e,f) being after 10.5 hours. All BF-LEEM images were taken at an electron energy of 2.9 eV, and all LEED patterns of 60 eV.

intercalation, we find areas with different brightness on the same terrace at an electron energy of 2.9 eV. It can clearly be seen that within a single terrace, there are bright (or gray) and dark areas, with their boundaries aligned parallel to the step edges, and the bright areas are more extensive than the dark areas. The LEED pattern obtained at this stage, shown in panel (b), presents no significant differences to the pattern before intercalation, as depicted in Fig. 4.1 (b).

To further understand the origin of the brightness contrast within the terraces, a pixel-by-pixel analysis using the semi-automatic *K-means* based approach (see **Sec. 3.4**) was performed on the LEEM-*IV* spectra obtained from the surface. The BF-LEEM image of the area from which the *IV* spectra were extracted is shown in Fig. 4.3 (a). The image covers an area of  $\approx 3.0 \times 2.5 \mu\text{m}^2$  ( $300 \times 250$  pixels) and was captured at an electron energy of 2.9 eV, corresponding to the minimum of the *IV* spectra extracted from the monolayer graphene. The



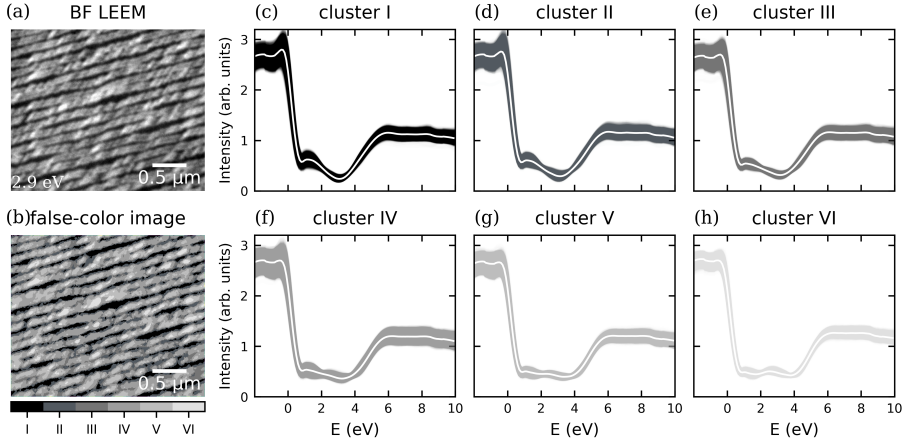


Figure 4.3: (a) BF-LEEM image of a small area on the surface after 3 hours of intercalation, recorded at 2.9 eV with a size  $\approx 3.0 \times 2.5 \mu\text{m}^2$  ( $300 \times 250$  pixels). LEEM-IV data in the energy range from  $-2$  to  $10$  eV have been recorded for the area and analyzed with the pixel-by-pixel method. (b) False-color presentation of the result of the LEEM-IV analysis. (c-h) Six curve clusters obtained through the pixel-by-pixel analysis. All curves are plotted with a transparency of 0.01, and the white curves in the middle represent the average of all spectra allocated to the respective cluster. Panel (b), and (c-h) share the same color codes.

IV spectra were grouped into six clusters based on their contours, which are displayed in Fig. 4.3 (c-h). The transparency of the curves was set to 0.01, with the averaged curve for each cluster plotted as a white line in the middle of each group. Although the contours of the extracted curves show a continuous variation, they were subjectively sorted into six clusters to quantitatively represent this gradual change, without any specific physical meaning. The spatial distribution of the clustering results is shown in panel (b) as a false-color image, using the same color coding as the curve clusters in panels (c) to (h).

The IV spectra in "cluster I" correspond to the darkest areas seen in both Fig. 4.3 (a) and (b). These curves still conserve the characteristic single minimum around 2.9 eV, typical for monolayer graphene. This is also the case for the curves in "cluster II", "cluster III", and even "cluster IV", but a continuous change is observed across the clusters, with the minimum valley becoming shal-

### 4.3 Intercalation of the Layers in Three Steps

---

lower. While cluster V contains rather flat curves, in "cluster VI", the curves begin to show a maximum around 2.9 eV, which aligns with the *IV* curve features of bilayer graphene and corresponds to the brightest areas both in the BF-LEEM and false-color images. Hence, the change of the curve shape is a indication for the (beginning) formation of a graphene bilayer, which can only be realized by the decoupling of the 30°-rotated ZLG from the substrate. The fact that the curve shapes change continuously suggest that, at least on the lengths scale of our resolution limit, this process occurs continuously and the brighter areas in the BF-LEEM image indicate a higher level of intercalation, which we interpret as an increasing hydrogen concentration beneath the ZLG. The length scale on which this "fractional intercalation" occurs, is smaller than our instrumental resolution of 10 nm. Furthermore, we cannot unambiguously decide whether or not the intercalation has already started at the darkest areas visible in the LEEM image, since it is not known at which intercalation level a change in the LEEM image intensity is detectable.

The findings also enable a principal understanding on the mechanism of the hydrogen intercalation. The parallel boundaries between areas with different brightness suggest that hydrogen infiltrates beneath the ZLG from discontinuous parts of the graphene layer, such as step edges and defects. Evidently, the hydrogen concentration is higher at step edges, and the hydrogen atoms most likely diffuse from the higher side of a step edge to the lower side of the next step edge. The parallel boundaries between the regions of different brightness also indicate the high quality of the top G- $R0^\circ$  layer achieved by the surfactant-mediated method [6]. This is evidenced by the absence of strong contrast in the direction parallel to the step edges within the terraces, which would otherwise suggest the presence of domain boundaries in the graphene layer within the terraces. The results also explain the similarity between the LEED patterns in Fig. 4.2 (b) and Fig. 4.1 (b). This is because the LEED pattern after intercalation was obtained from many different regions, while most of them still retain the bonding between the ZLG and the substrate.

The current investigation reveals that 3 hours of intercalation are insufficient to achieve 30°-TBG on the surface. Therefore, we have extended the intercalation treatment by another three hours at the same conditions. The BF-LEEM image

## Chapter 4. 30°-TBG via Hydrogen Intercalation

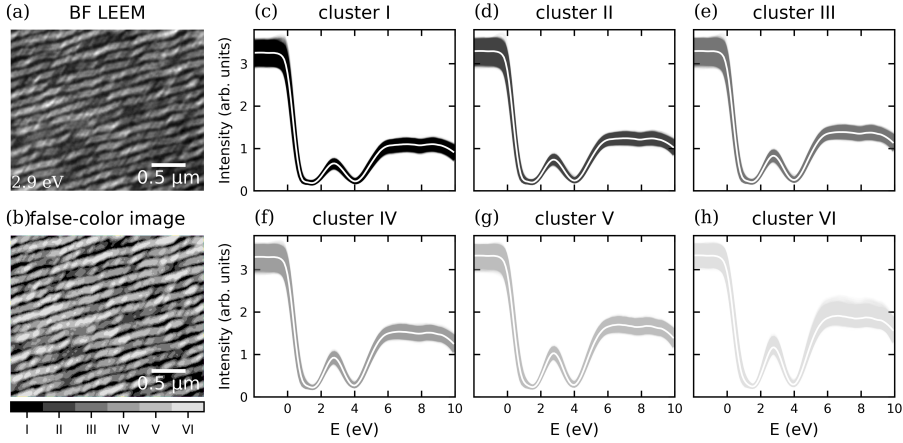


Figure 4.4: Same as Fig. 4.3, but after 6 hours of intercalation. Note that separate color codes were defined for each of the figures.

and LEED pattern obtained after a total of 6 hours of intercalation are shown in Fig. 4.2 (c) and (d), respectively. While the different brightness levels within the terraces are still present in panel (c), the boundaries that were previously parallel to the step edges are no longer visible. The LEED pattern, shown in panel (d), closely resembles the pattern obtained from the "high-T" sample discussed in the previous chapter (Fig. 3.6 "LEED"). That sample was proved to be covered by a 30° twisted bilayer and multilayers graphene. The only notable difference is that the satellite spots around the main spot and  $G-R0^\circ$  spots, which originate from the  $(6\sqrt{3} \times 6\sqrt{3})R30^\circ$  reconstruction of the ZLG, are absent in the LEED pattern shown in Fig. 4.2 (d). This LEED pattern also suggests successful intercalation.

Pixel-by-pixel analysis similar to that performed for the 3-hours intercalation was also executed on LEEM-IV data obtained after 6 hours of intercalation, and the BF-LEEM image of the selected area is presented in Fig. 4.4 (a), with dimensions of approximately  $3.0 \times 2.5 \mu\text{m}^2$  (corresponding to  $300 \times 250$  pixels). The *K-means* based clustering was applied with the *K* value primarily set equal to six. The clustering results are displayed as six distinct spectral bunches in Fig. 4.4 (c-h), with a corresponding spatial representation shown as an FC image in panel (b) using the same color coding as panels (c-h). The results turn out that

### 4.3 Intercalation of the Layers in Three Steps

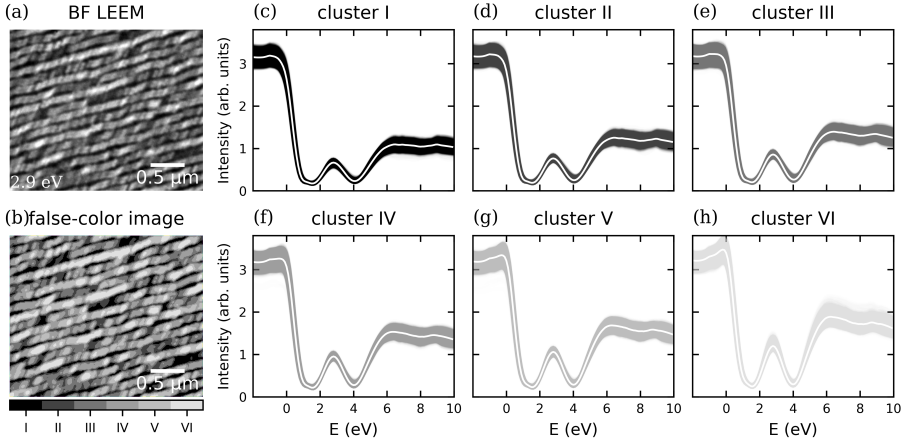


Figure 4.5: Same as Fig. 4.3 and Fig. 4.4, but after 10.5 hours of intercalation. Note that separate color codes were defined for each of the figures.

clustering sorted the curves into six curve bunches that continuously change in their oscillation amplitude (cluster I to VI). All curves generally exhibit two minima at 1.5 eV and 4.0 eV, along with a prominent maximum at 2.9 eV. The two minima in the contour of all *IV* spectra reveal the successful intercalation of the whole investigated area, which was clearly not the case after 3 hours of intercalation. However, the origin of different brightness levels appearing within the terraces shown in Fig. 4.2 (c) and Fig. 4.4 (a) is still an open question. Since this might still be due to an inhomogeneous degree of hydrogen intercalation, we continued the intercalation process up to a total time of 10.5 h.

The BF-LEEM image and LEED pattern of the sample surface after a total of 10.5 hours of intercalation are shown in Fig. 4.2 (e) and (f). Despite the extended intercalation time, brightness differences within terraces are still present, and the LEED pattern remains unchanged. The BF-LEEM image in Fig. 4.2 (e) appears only slightly smoother compared to panel (c). Moreover, the pixel-by-pixel analysis was repeated on the *IV* data obtained after 10.5 hours of intercalation. The results, shown in Fig. 4.5, were comparable to those obtained after 6 hours of intercalation, ruling out the possibility that the brightness contrasts arise from varying degrees of intercalation.

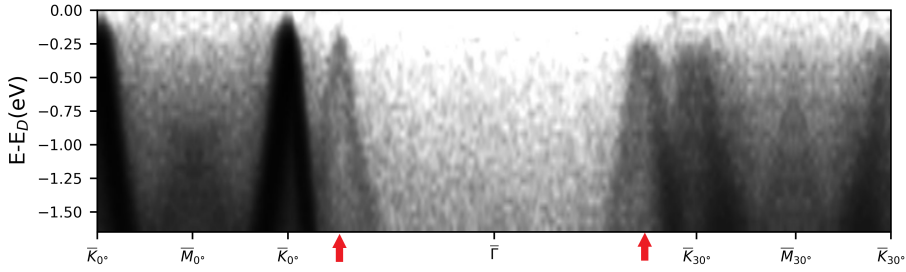


Figure 4.6: Dispersion of the  $\pi$  band measured with ARPES below the Dirac point along with the  $\bar{\Gamma}\bar{K}_0^\circ\bar{K}_0^\circ$  and the  $\bar{\Gamma}\bar{K}_{30}^\circ\bar{K}_{30}^\circ$  directions for the Brillouin zone of hydrogen intercalated 30°-TBG.

The electronic structure of the sample was also investigated. The energy dispersion of the  $\pi$  band along the  $\bar{\Gamma}\bar{K}_0^\circ\bar{K}_0^\circ$  and the  $\bar{\Gamma}\bar{K}_{30}^\circ\bar{K}_{30}^\circ$  directions is shown in Fig. 4.6. A Dirac cone with the highest intensity is found at the  $\bar{K}_0^\circ$  position. The intensity of the Dirac cone at the  $\bar{K}_{30}^\circ$  position is significantly lower, as it originates from the underlying G- $R30^\circ$  layer (previous ZLG- $R30^\circ$ ) that is shielded by the top G- $R0^\circ$  layer. The presence of the Dirac cone at the  $\bar{K}_{30}^\circ$  position also proves the successful decoupling of the ZLG from the substrate and its transformation into G- $R30^\circ$ . Additionally, two new Dirac cones located beside the two at the  $\bar{\Gamma}\bar{K}_0^\circ$  and the  $\bar{\Gamma}\bar{K}_{30}^\circ$  positions show up, marked by two red arrows in Fig. 4.6, which are attributed to mirrored Dirac cones resulting from Umklapp scattering [104]. Both graphene layers exhibit a charge-neutral character, which is expected given their quasi-freestanding nature and the reduced influence of the substrate. The alignment of the two Dirac cones in energy indicates a strong interlayer interaction, suggesting significant charge carrier hybridization between the two graphene sheets.

Therefore, after a total of 10.5 hours of intercalation, the sample is fully intercalated and homogeneously covered by 30°-TBG. The variation in brightness observed in the BF-LEEM image could be attributed to strain within the bilayer or slight differences in the twist angle between the layers. This is supported by the slight elongation of the graphene diffraction spots in the azimuthal direction, as seen in the example LEED pattern in Fig. 4.2 (f).

While we so far discussed the intercalation process, the deintercalation process is also of high interest in terms of the reversibility and understanding its mechanisms. In the following, the deintercalation of a 30°-TBG sample achieved via hydrogen insertion will be discussed.

#### 4.4 Deintercalation of 30°-TBG

The intercalation process to produce large-scale homogeneous 30°-TBG was carried out step by step, rather than monitored in real-time using LEEM. This experimental design was necessary because the hydrogen partial pressure in the chamber during intercalation had to be three magnitudes higher than the critical pressure for LEEM to be operated, in order to achieve a decent intercalation rate. However, the deintercalation process does not present the same issue, allowing it to be monitored in real-time with LEEM.

The deintercalation process was conducted on a different sample, the surface of which was only partially H-intercalated. Beside the H-intercalated bilayer graphene areas (G- $R0^\circ$ /G- $R30^\circ$ /H-saturated SiC), we also found epitaxial bilayer graphene (G- $R0^\circ$ /G- $R30^\circ$ /ZLG), and epitaxial triple-layer graphene (G- $R0^\circ$ /G- $R30^\circ$ /G- $R30^\circ$ /ZLG) areas. Since there are few triple-layer areas on the surface and the hydrogen intercalation mainly results in the formation of bilayer structure, the discussion will primarily focus on the comparison of the two types of bilayer areas.

To prepare this sample, a SiC substrate was annealed slightly above 1350 °C using the surfactant-mediated growth method. This resulted in a surface that was dominantly covered by a mixture of monolayer G- $R0^\circ$  (stacked as G- $R0^\circ$ /ZLG), epitaxial 30°-TBG (stacked as G- $R0^\circ$ /G- $R30^\circ$ /ZLG). After a subsequent hydrogen intercalation for 4 h, the monolayer G- $R0^\circ$  regions were converted into 30°-TBG, referred to as "inter-bilayer" areas. The epitaxial 30°-TBG (stacked as G- $R0^\circ$ /G- $R30^\circ$ /ZLG) and triple-layer regions maintained their structures, with the epitaxial 30°-TBG referred to as "epi-bilayer" in the following discussion. The intercalation results also indicate that surface areas covered by monolayer graphene are much more easily intercalated by hydrogen than bilayer and triple-

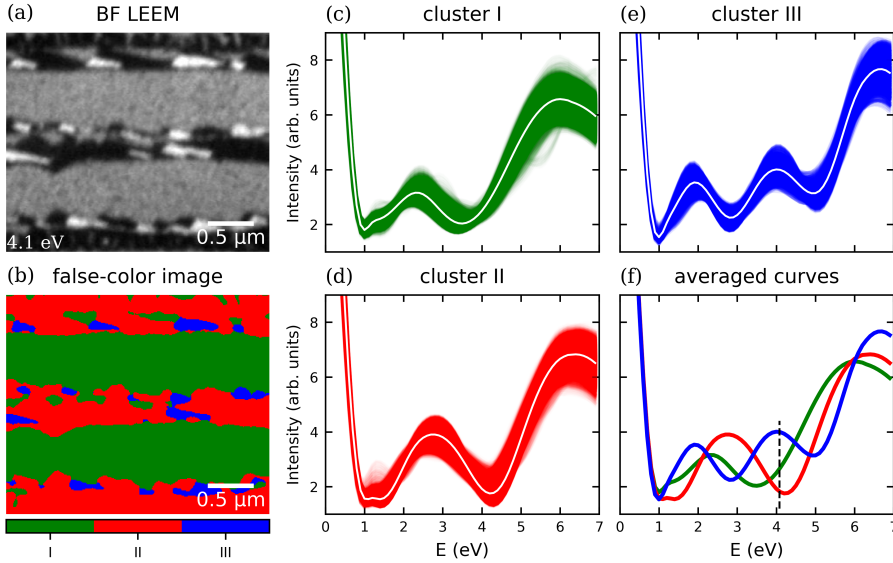


Figure 4.7: (a) BF-LEEM image of a small area on the surface after 4 hours of intercalation, recorded at 4.1 eV with a size  $\approx 3.0 \times 2.5 \mu\text{m}^2$  ( $300 \times 250$  pixels). LEEM-IV data in the energy range from 0 to 7 eV have been recorded for the area and analyzed with the pixel-by-pixel method. (b) False-color presentation of the result of the LEEM-IV analysis. (c-e) Three curve clusters obtained through the pixel-by-pixel analysis. All curves are plotted with a transparency of 0.01, and the white curves in the middle represent the average of all spectra allocated to the respective cluster, and they are plotted in the same graph in (f). Panel (b), (c-e), and (f) share the same color codes.

layer graphene, which is reasonable given the greater difficulty for hydrogen atoms to penetrate beneath the ZLG. The reason for taking a such sample to do deintercalation will be given in the following discussion.

The BF-LEEM image of a small surface region right after the hydrogen intercalation is shown in Fig. 4.7 (a). At the electron energy of 4.1 eV, there are clearly three different brightness levels. Again, we performed a *K-means* based pixel-by-pixel analysis on the LEEM-IV data extracted from the area to figure out the stacking configuration. All spectra are grouped into three clusters according to their number of oscillations and the positions of minima, and plotted forming three curve bunches shown in Fig. 4.7 (c-e). The spatial distribution

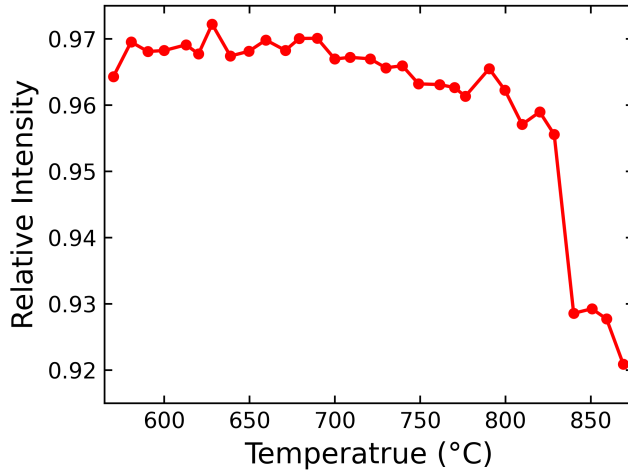


Figure 4.8:  $R_{Intensity}$ , defined as the ratio of the averaged intensity of "inter-bilayer" areas to that of "epi-bilayer" areas, with respect to the annealing temperature during the deintercalation process.

of the clustering results is given as a false-color image in panel (b). Apparently, the  $IV$  spectra with triple-minima in the group labeled as "cluster III", can be assigned to the triple-layer areas. They correspond to the blue-colored areas in the FC image, and the brightest areas in the BF-LEEM image. Spectra in "cluster I" and "cluster II" exhibit similar profiles with two minima, but the position of the second minimum differs, one is around 3.6 eV and the other around 4.2 eV. It is unambiguous that both curve clusters are related to a bilayer stacking configuration on the surface. Based on own reference data and on a comparison with the literature [2, 38, 137, 138], the spectra featuring a second minimum at 4.2 eV are most likely associated with the "epi-bilayer" regions, as this characteristic is distinct and consistent, serving as a reliable fingerprint for epitaxial bilayer graphene. Moreover, spectra with a second minimum near 3.6 eV are likely linked to the "inter-bilayer" regions. The deviation from 4.2 eV is presumably due to factors such as a low hydrogen concentration, given that the sample underwent hydrogen intercalation for only 4 h. This interpretation was further proved by subsequent deintercalation study.

The white lines in the center of each curve bunch represent their averages and



are plotted together in a single graph, shown in panel (f). The color codes match those used for the individual curve bunches. The black dashed line indicates the energy level at which the BF-LEEM image in panel (a) was captured. At 4.1 eV, the blue-colored curve shows the highest intensity, followed by the green-colored curve, and the red-colored curve has the lowest intensity, which is in agreement with the observation of the brightness contrast in the BF-LEEM image.

The sample was slowly annealed from RT to 940 °C with a heating rate of 3 °C/min for the deintercalation to take place, and the whole process was monitored and followed with LEEM in situ. To interpret the changes on the surface, a factor  $R_{Intensity}$ , representing the relative electron reflectivity between different bi-layer areas, is defined as the ratio of the averaged intensity of "inter-bilayer" areas to that of "epi-bilayer" areas. A plot of  $R_{Intensity}$  as a function of the annealing temperature is given in Fig. 4.8, with a temperature step of approximately 10 °C between neighboring data points. A drastic drop of the  $R_{Intensity}$  is observed in the temperature range from 800 °C to 850 °C, which means that the deintercalation took place in this temperature range.

Fig. 4.9 presents a sequence of LEEM images captured during deintercalation in the temperature range from 800 °C to 850 °C, covering an area of approximately  $\approx 10 \times 8.8 \mu\text{m}^2$ . The kinetic energy of electrons was set to 2.3 eV, corresponding to the maximum in the  $IV$  spectra shown in Fig. 4.7 (c). Areas appearing bright in the LEEM images are covered by "epi-bilayer" graphene, while the areas appearing as individual long gray stripes are covered by "inter-bilayer", which is learned from the relative intensity shown in Fig. 4.7 (f).

At around 800 °C, the brightness of the "epi-bilayer" areas is only slightly higher than that of the "inter-bilayer" areas as shown in Fig. 4.9 (a). As the temperature increases, the brightness of the "inter-bilayer" areas uniformly decreases. To interpret the brightness variation of the "inter-bilayer" areas during the deintercalation, colored lines with a length of 20 pixels were drawn crossing an "inter-bilayer" area and perpendicular to the step edges on the surface, as drawn in Fig. 4.9 (a-e). The intensity along with these colored lines ("line scans") are plotted in panel (f). It is evident that the minimum intensity of the curves gradually decreases from the cyan to black colored curve. In other words, the difference

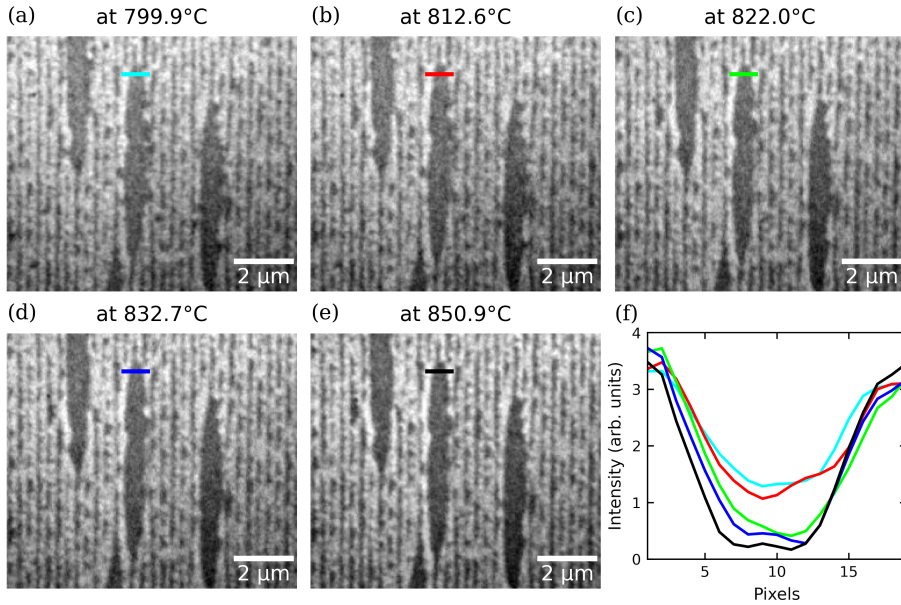


Figure 4.9: (a-e) LEEM image sequence captured during the hydrogen deintercalation process in the temperature range from 800 °C to 850 °C. All the images are obtained at an electron energy of 2.3 eV, at which the "epi-bilayer" areas appear brighter than the "inter-bilayer" areas. All the LEEM images have the same brightness scale. (f) Pixel-intensity-profile plotted along with the colored lines in each LEEM image (a-e), and each colored curve corresponds to the same colored line in the LEEM images.

in brightness between the "inter-bilayer" and "epi-bilayer" areas expands with increasing annealing temperature.

In contrast to the intercalation process, where distinct boundaries were observed between intercalated and non- (or) less-intercalated regions within the terraces, as discussed in the previous section, we observe a homogeneous change in the LEEM intensity in the H-intercalated regions, indicating that hydrogen desorbes homogeneously from the terraces, not only at the step edges. The deintercalation happened in a short time-scale of around 1 min, probably due to the increasing temperature. A similar observation was reported in Ref. [72], and our work provides the direct visualization of the deintercalation process. Annealing at a

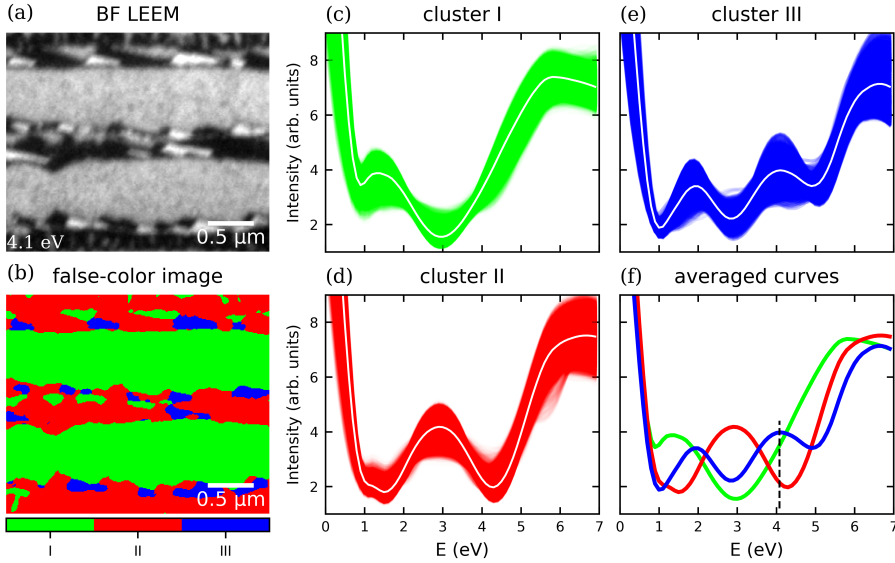


Figure 4.10: Same as Fig. 4.7, but after the deintercalation. (a) BF-LEEM image of the same area on the surface. (b) False-color presentation of the result of the LEEM-IV analysis. (c-e) Three curve clusters obtained through the pixel-by-pixel analysis. Panel (b), (c-e), and (f) share the same color codes.

higher temperature above 820 °C (in contrast to around 660 °C for intercalation) may drastically increase the mobility of hydrogen atoms during the diffusing out of the interface between the graphene layer and substrate, or allow hydrogen atoms to pass through the graphene layer. Alternatively, the elevated annealing temperature could induce greater stress and strain in the graphene, leading to more crystalline defects, which provide pathways for the hydrogen atoms to escape from the surface.

The observation explains why a sample partially covered with "epi-bilayer" and "inter-bilayer" graphene was selected for deintercalation. Since deintercalation occurs uniformly, high-temperature annealing can slightly alter the imaging conditions in LEEM, making it difficult to detect deintercalation on a large, uniform TBG sample. The presence of "epi-bilayer" areas serves as a reference point, as they remain stable and well-defined during annealing.

After cooling down to room temperature, the same surface area discussed in Fig. 4.7 was investigated with BF-LEEM and LEEM-*IV* measurement to determine the current stacking configuration. The BF-LEEM image of the area after the deintercalation is shown in Fig. 4.10 (a), and the clustering results of the *K-means* based pixel-by-pixel LEEM-*IV* analysis is given in panel (b-f). An evident change is the profiles of *IV* spectra extracted from the previous "inter-bilayer" areas turn into typical contour of a monolayer graphene with a single deep minimum at around 3 eV, which is a direct proof for the successful deintercalation. The "epi-bilayer" areas and triple-layer areas remain constant features as previous. Moreover, the monolayer area in Fig. 4.10 (a) appears slightly brighter than that in Fig. 4.7 (a), which is also sensible by comparing the relative intensity at 4.1 eV where the black dashed line intersects the three averaged curves in Fig. 4.10 (f).

## 4.5 Conclusion

Quasi-freestanding 30°-TBG was successfully created through hydrogen intercalation on a 6H-SiC(0001) substrate with 0°-rotated epitaxial monolayer graphene. A pixel-by-pixel analysis of LEEM-*IV* data, performed in the same way as the semi-automatic *K-means* based method described in **Chapter 3**, revealed the bilayer stacking configuration after intercalation, and LEED measurements confirmed the 30° rotation between the layers. ARPES measurements displayed duplicated twelve Dirac cones, indicating strong interlayer coupling between the two graphene sheets and complete decoupling of the ZLG from the substrate. In addition to the twelve pristine Dirac cones of the two layers, twelve replicas were observed near each cone, located between the  $\bar{\Gamma}$  and  $\bar{K}$  points, explained by Umklapp scattering [104].

The hydrogen intercalation and deintercalation processes were studied using LEEM, with intercalation performed stepwise and deintercalation monitored in-situ and in real time. Our experimental results provide valuable insights into the mechanisms of hydrogen intercalation and deintercalation.

Operating intercalation in steps allows for the examination of the surface at in-

## Chapter 4. 30°-TBG via Hydrogen Intercalation

---

intermediate stages. During the intercalation process, sharp boundaries between intercalated and non-intercalated areas are observed, aligned parallel to the step edges. This parallel expansion of the intercalated regions suggests that hydrogen atoms do not penetrate through the graphene layer but instead migrate beneath the ZLG from discontinuities on the surface, such as step edges or defects. Variations in hydrogen concentration under the ZLG lead to gradual changes in the *IV* spectra, transitioning from a single minimum to double minima, indicating different stages of intercalation. Even after the process is complete, as indicated by all pixel-by-pixel *IV* spectra showing double minima, brightness contrasts between areas remain visible, which might be attributed to the strain in the bilayer, or small variations in the twist angle.

The deintercalation process of the graphene sample was monitored in-situ using LEEM, revealing the complete mechanisms and behavior of hydrogen atoms during deintercalation. Before the deintercalation, it was shown that the monolayer areas are much easier to be intercalated compared to the bilayer, and triple layer areas, which is expected given the increased difficulty for hydrogen to reach below the ZLG when multiple graphene layers are present. Annealing at around 820 °C, 200 °C higher than the intercalation temperature, triggers the deintercalation process, which completes in a much shorter timescale, within 1 minute. In contrast to intercalation, this process occurs homogeneously, as indicated by the uniform change in brightness across deintercalated areas. This suggests that at high temperatures, hydrogen atoms might be able to penetrate through the graphene layer, or the increased strain in the graphene layer during annealing may introduce more crystalline defects, allowing the hydrogen to escape.

## 5 [6]-CPP on Cu(111)

To gain a comprehensive understanding of the [6]-CPP on Cu(111) system, we used the LEEM technique both to monitor the deposition and annealing of molecules on the surface, and to execute the subsequent structural characterization after each step, taking advantage of its ability to observe processes in situ and in real-time. The molecules applied in our experiment are synthesized and provided by Dr. Qitang Fan from Prof. Gottfried's group in Philipps-Universität Marburg. At the room condition, they appear as orange-colored powder.

### 5.1 Deposition

The molecules are loaded into a molecule evaporator which is directly attached to the main chamber of the LEEM instrument. The experiment was executed in UHV with a base pressure of  $9.0 \times 10^{-10}$  mbar. During the deposition, the evaporator was heated to 250 °C for sublimating. The substrate is a Cu (111) crystal, which was cooled below –60 °C by a liquid nitrogen flow cryostat. After deposition, the sample was annealed step-wise to different temperatures in order to trigger the different reaction steps as outlined in **Sect. 1.4**.

The deposition and subsequent annealing of molecules on the surface were monitored using LEEM, and the surface at various stages of the experiment was characterized with the LEED technique. The experiment was repeated several times with varying molecule coverages on the surface. In the following

discussion, we will focus on one of these experiments that yielded representative results.

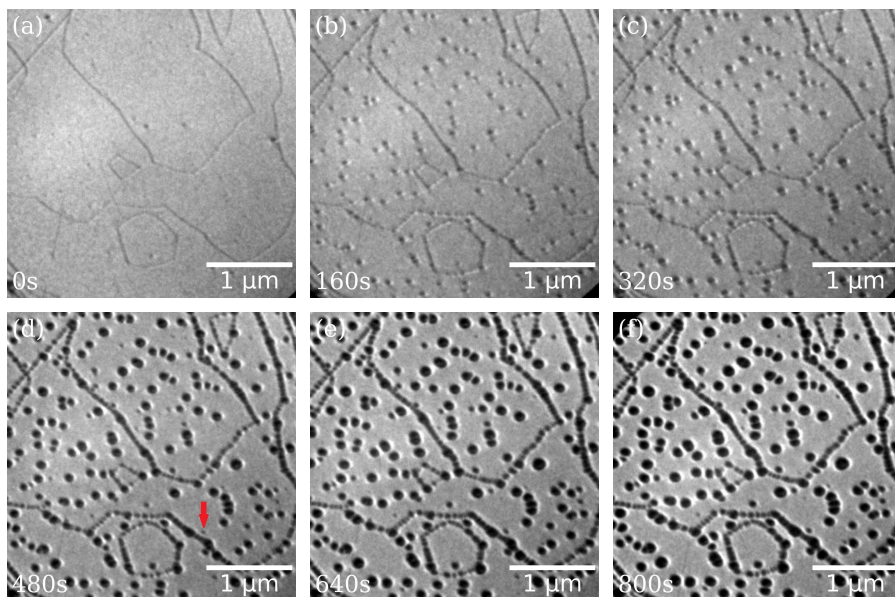


Figure 5.1: LEEM images of the sample surface at different times during the molecule deposition. The label in the bottom-left corner of each panel is the time point with respect to opening of the shutter.

LEEM images recorded at different times during the deposition of molecules are depicted in Fig. 5.1. Fig. 5.1 (a) shows the clean surface before deposition. The gray lines are the step edges of the Cu atomic layers, and some spot-like objects are defects or contaminations, which will act as the nucleation sites for the molecules. Most of the nucleation took place in the first 100 s. Afterwards, the molecules prefer attaching to the existing clusters, which let these clusters grow (quickly). Moreover, a small number of nucleation still occur during the deposition process. An example is the object marked by a red arrow shown in Fig. 5.1 (d), which is invisible in the earlier images but slowly grew up in the later ones. Islands in the center/middle of terraces grow faster in size compared to those attaching to the step edges. Apparently, the step edges can hinder the expansion of the islands in this direction. Note that all the islands on the

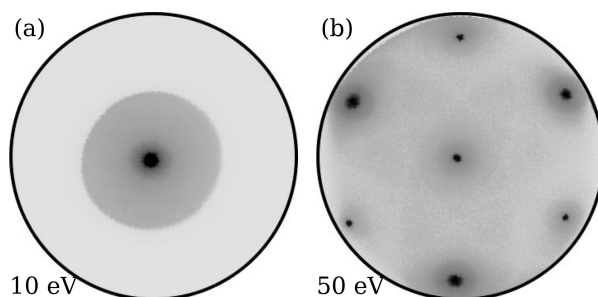


Figure 5.2: LEED patterns obtained right after the deposition. The label in the bottom-left corner of each panel are the kinetic energy of the electrons during the LEED measurement.

surface tend to have a round shape and slightly brighter edges, which is a typical indication for slightly under-focus imaging conditions. This is consistent with the fact, that the step edges of the substrate are less pronounced in the first images of the deposition series, since this indicates that the Cu surface is in focus. Protruding molecular islands are thus higher than the Cu surface, and appear already in slight underfocus in the LEEM images. Hence, focus conditions change very quickly for protruding objects (islands) on the surface, compared to the surface below.

Two LEED patterns obtained right after the deposition are given in Fig. 5.2, which are taken at 10 eV and 50 eV, respectively. Different energy levels have been chosen because it was discovered that the molecules are highly sensitive to beam damage, see discussion below. In both patterns, only the main spot and substrate spots are visible, with no other discernible spots—but only some diffuse intensity. This could be due to the low coverage of the molecules on the surface. Although the coverage was increased in subsequent experiments, the results remained similar, suggesting that the molecules on the surface are likely disordered. Additionally, LEEM-*IV* curves were extracted from the island areas, but these curves exhibited low intensity and a consistently flat shape with no significant oscillations, providing limited information.

Since the deposition took place on a cooled sample, it is possible that the formed objects on the surface are more likely 3D clusters with molecules pilling up,



rather than 2D molecule islands. The pilling-up of molecules could be caused by combined effects. First, the mobility of molecules on the surface is low due to the low temperature of the substrate. Secondly, the  $\pi$ - $\pi$  interactions between molecules are strong. These interactions arise from the overlapping of  $\pi$ -orbitals of the benzene rings, leading to attractive forces between the molecules. This type of interaction is common in aromatic systems and is significant in determining the packing and aggregation behavior [155–160]. The last factor is the weak Van der Waals force between the molecule and the substrate, which might be weaker than the inter-molecule interactions and allows the [6]-CPP molecules to retain their tire-like shapes at low temperatures, despite the Cu (111) surface being highly active. Subsequently, the substrate was gradually annealed in stages to observe the changes on the surface with increasing temperature.

### 5.2 Warming-up to RT (25 °C)

After the deposition, the sample was slowly warmed up to room temperature (RT) around 25 °C with a rate of 3 °C/min by shutting down the liquid nitrogen flow. Then, the sample was kept at 25 °C for three days to stabilize the movement of molecules on the surface. The following LEED measurement confirmed the formation of some ordered structure on the surface, as discussed below. Also further annealing to a higher temperature was applied to trigger the opening of rings.

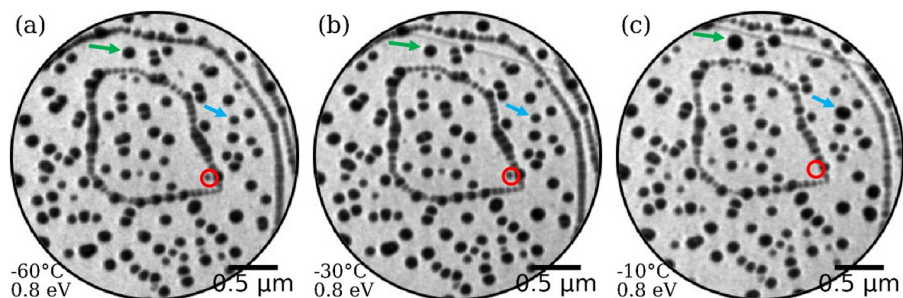


Figure 5.3: LEEM images captured during the annealing from  $-60\text{ }^{\circ}\text{C}$  to RT. Sample temperature and kinetic energy of the electrons are given in the lower left of the images.

## 5.2 Warming-up to RT (25 °C)

The warming-up of the sample to RT was monitored using low energy electron microscopy (LEEM). Three LEEM images captured during this process are shown in Fig. 5.3. The labels in the bottom-left corner of each panel indicate the temperature at which each image was taken. Redistribution of molecules on the surface was observed, evidenced by the changes in the sizes of certain molecule clusters. Specifically, the cluster circled in red in Fig. 5.3 disappears after the warming-up. Additionally, the clusters marked with blue and green arrows increase in sizes, as seen by comparing panels (a) and (c). It is remarkable that at these relatively low temperatures, the molecules are very mobile on the surface resulting in significant changes in surface morphology over a short period. The LEED measurement taken immediately after annealing reveals that the surface structures remain disordered, as no new LEED spots appear. This indicates that the molecules are moving between clusters without forming an ordered structure. Stabilizing the molecules on the surface, for example, by keeping the sample at RT for a period, may be necessary to achieve the desired ordered structures.

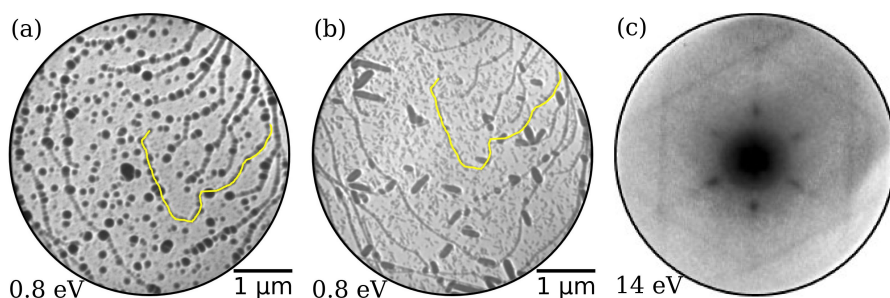


Figure 5.4: LEEM images of the surface taken (a) before and (b) after keeping the sample at 25 °C for three days. Both images are captured with an electron energy of 0.8 eV. The yellow curves in both images mark the same step edges. (c) LEED pattern taken with an electron energy of 14 eV at the end of the three days.

The sample was kept at RT around 25 °C for three days in the UHV, resulting in noticeable changes to the surface morphology. Figure 5.4 presents two LEEM images captured before (a) and after (b) the three-day stabilization period. The yellow curves in both images delineate the same step edges of the substrate,

confirming that the LEEM imaging occurred in the identical area of the surface. The redistribution of molecules caused most of the circular-shaped molecule clusters visible in Fig. 5.4 (a) to dissolve. After stabilization, two distinct types of objects emerged on the surface, as shown in Fig. 5.4 (b). First, there are large objects with elongated contours, generally larger than those observed immediately after deposition. These elongated objects exhibit bright contours in the LEEM image, indicating that their height is significantly greater than that of the substrate.  $\mu$ -LEED measurements on those elongated dark objects indicates that those areas have no crystalline order. Secondly, there are small, slightly brighter objects with various shapes that are randomly distributed across the surface. These objects are too small for  $\mu$ -LEED, but overall LEED measurements show a diffraction pattern, as shown in Fig. 5.4 (c), and hence confirm the formation of ordered structures on the surface. The LEED pattern was obtained at a low energy level of 14 eV, making the substrate's LEED spots invisible. Six spots appear around the (00) main spot, indicating some two dimensional order on the surface. Additionally, several straight lines traverse the LEED pattern, forming a hexagon around the spots in the image. The appearance of these straight lines indicates the formation of low-dimensional ordered structures, such as long chains. This suggests that ring-opening of the molecules and polymerization into long chains may have occurred during warming-up to RT and stabilization.

Fig. 5.4 (b) shows the surface after three days of keeping at RT. However, a single static image cannot fully convey the actual state of the surface. During annealing from  $-60^{\circ}\text{C}$  to RT, the molecules are known to re-distribute on the surface. While some of them have formed ordered structures on the surface, others still possess certain mobility. Fig. 5.5 displays six LEEM images at a smaller FoV of the surface recorded after the three days in 10 s interval. Colored arrows consistently mark the same areas across the panels. By comparing these areas, changes on the surface can be observed. For example, an object appears and disappears in the region marked by the red arrow in different images. Interpreting the surface changes from just the six images is challenging, and when scrolling through the image sequence, one can more easily sense them. The movement of molecules or small molecule clusters locally changed the electron intensity of the gray areas

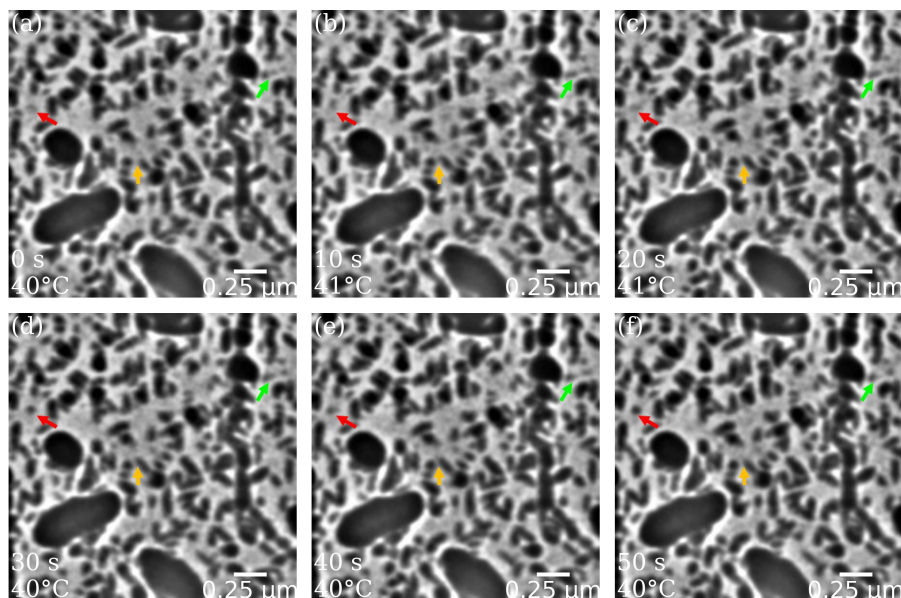


Figure 5.5: (a) to (f) LEEM images captured after keeping at RT for three days. The labels in the bottom-left corner of each panel give the temperature and relative time with respect to image (a). The colored arrows in (a) to (f) mark the same area in each panel, respectively. All the LEEM images were captured with an electron energy of 1 eV.

shown in Fig. 5.5. It can be inferred from this that the molecules are still mobile and diffusing between islands, and might need more time to settle down, which means that the attractive interaction between the molecules and the substrate is weak. There is also other possibility that the molecule coverage on the surface is already too high to accommodate them.

It needs to be noted that the intensity of the six new spots is quite low comparing to that of the (00) main spot in Fig. 5.4 (c), and imaging quality of the LEED pattern is unsatisfactory, which could be due to the low coverage of molecules. In an other experiment, the molecule coverage was increased by about three times and the same stabilization procedure has been executed. The LEED measurements were conducted starting at a low energy of 4 eV and gradually increased to 50 eV. This approach was taken due to the extreme sensitivity of

the molecules to beam damage. The resulting LEED patterns are displayed in Fig. 5.6. In panel (a), taken at 4 eV, six sharp LEED spots are clearly visible and are located close to the (00) spot. As the energy increases, more diffraction spots appear in the field of view (FoV) due to the increasing diameter of the Ewald sphere. The second-order diffraction spots emerge in the Fig. 5.6 (b) which was taken at 10 eV, and two of them are marked by red arrows. Interestingly, the six diffraction spots in Fig. 5.6 (a) gradually fade as the electron energy increases, as shown from images (a) to (e). By the time the energy reaches 50 eV in image (e), these spots are completely invisible, and the substrate spots become apparent. After completing the LEED measurement at 50 eV, a subsequent measurement at 4 eV was performed, again. However, the six spots around the (00) beam no longer appeared, indicating beam damage. Among the LEED patterns shown in Fig. 5.6, lines crossing the spots suggest the formation of low-dimensional ordered structures on the surface at RT, likely due to the ring-opening and polymerization forming long polyparaphenylene (PPP) chains.

During the experiment, particularly during the LEED measurement, beam damage was found to be a significant issue for the [6]-CPP molecules. This effect becomes concretized in LEEM mode. Fig. 5.7 shows two LEEM images of a surface area: one taken right after deposition and another after annealing to 180 °C. In Fig. 5.7 (a), the molecule clusters exhibit pimple-like shapes. Subsequently, several  $\mu$ -LEED images were taken with the electron energy up to 50 eV. The bright circular area is where the electron beam illuminated the surface, its shape originates from the illumination aperture of the instrument, which blocks most of the electron intensity. After annealing the sample to 180 °C, most molecule clusters have dissolved, except for those that were illuminated before, which indicates a severe beam damage of the molecules. After several experiments, it has been uncovered that the beam damage becomes significant when the electron energy exceeds 10 eV, and the longer the molecules are illuminated, the greater the extent of beam damage. Moreover, it is worthy to mention that our LEEM instrument, which can be operated at low electron energies and perform LEED at extremely low energies below 10 eV, is an ideal tool for studying the [6]-CPP/Cu(111) system in terms of minimizing the damage to the molecules.

LEED is a proper tool for revealing the crystalline orientation of superstructures

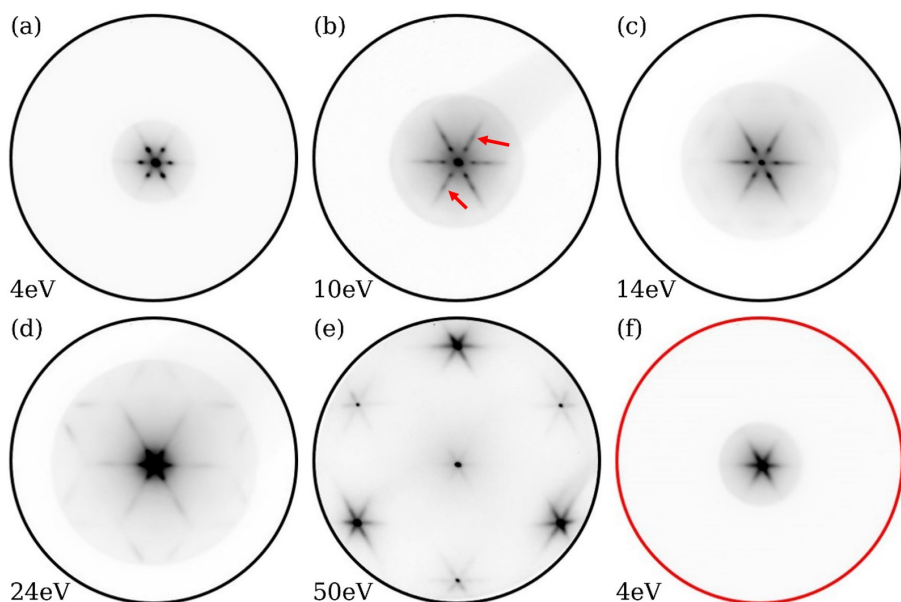


Figure 5.6: LEED patterns obtained from the surface with a coverage that is three times higher than that of the experiment shown in Fig. 5.4(b). LEED pattern (f) is obtained with an electron energy of 4 eV, but after the LEED measurement at 50 eV.

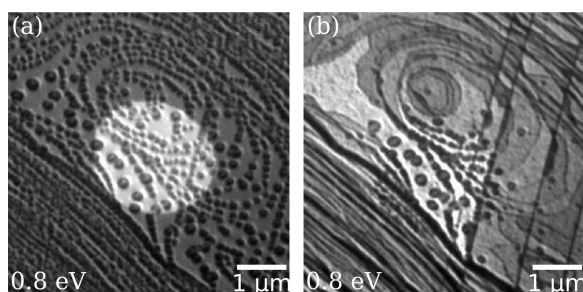


Figure 5.7: LEEM images of a surface area (a) right after deposition at a low temperature, and (b) after annealing to 180 °C. The bright circle in image (a) marks the area that was illuminated by the electron beam during the LEED measurement. Both images were captured with an electron energy of 0.8 eV.

on a surface. However, in the [6]-CPP/Cu(111) system, the LEED spots of the superstructures and the substrate cannot be recorded in a single LEED pattern due to beam damage at high energies. To address this, LEED composite images were created by overlapping LEED patterns obtained at 4 eV and 50 eV. Fig. 5.8 displays three LEED composite images from measurements taken during different experiments. In these images, LEED spots from the 4 eV pattern are colored red, while spots from the 50 eV pattern (specifically, the substrate spots) are green. It should be clarified that Fig. 5.8 (a) is made by overlapping Fig. 5.6 (a) and (e), and Fig. 5.8 (b) and (c) are from the LEED measurements of other two experiments. Each panel displays six substrate spots with varying brightness: three spots are brighter than the others due to the symmetry of the Cu(111) substrate. Interestingly, two different orientations of the superstructure spots were observed as shown in Fig. 5.8 (a) and (b). Apparently, the superstructure spots in Fig. 5.8 (a) are 30 degree rotated with respect to the substrate spots, while those in Fig. 5.8 (b) are aligned to the substrate spots, indicating two possible crystalline orientations for the superstructures on the Cu(111) surface. This discovery also explains the acquisition of the LEED pattern in Fig. 5.8 (c), in which a dodecagram is observed around the (00) main spot. Although clear and sharp diffraction spots are absent—likely due to the full opening of molecular rings—the lines typically intersect and align with the spots. Thus, the formation of the dodecagram pattern could result from the coexistence of two differently oriented domains within the area illuminated by the LEED electron beam.

In this section, we looked at the deposition of molecules on a cooled substrate and the behavior of molecules on the surface at RT via LEEM and LEED technique. To facilitate the polymerization, the sample was annealed to around 180 °C in the next step.

### 5.3 Annealing to 180°C

As previously discussed, the molecules require some time to form an ordered structure on the surface, indicating they possess a certain degree of mobility on the surface at room temperature. The annealing process to 180 °C was carried out in two steps. In the first step, the sample was heated from 25 °C to 90 °C,

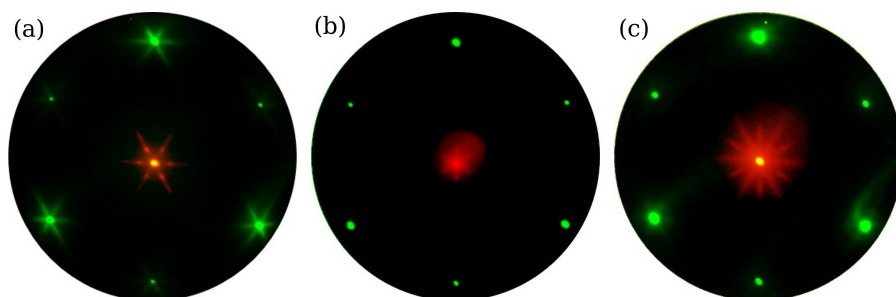


Figure 5.8: LEED composite images of LEED patterns obtained at 4 eV and 50 eV. LEED patterns at 4 eV are colored in red, while those at 50 eV in green. (a) the color composite image of Fig. 5.6 (a) and (e). (b) and (c) composite images are made from the LEED measurements of other experiments.

followed by cooling to  $-20^{\circ}\text{C}$ . Subsequently, the sample was directly annealed to  $180^{\circ}\text{C}$  in the second step. This experiment was designed to compare and investigate the interaction between the substrate and the large, elongated disordered objects, as well as the interaction between the substrate and the smaller, less gray objects, which most probably contribute to the formation of the LEED spots in Fig. 5.6 (a-c).

Fig. 5.9 shows a sequence of LEEM images, which were taken at different times during the annealing to  $90^{\circ}\text{C}$ . Generally, the molecules on the surface can be activated by a warmer substrate, which means that the mobility of molecules becomes higher. During the annealing from RT to around  $70^{\circ}\text{C}$ , we observed quite active movements of the small gray objects on the surface. A more vivid description about them is that those small objects behave like bugs moving around within a small nearby area. Their movement is hard to show up with only three images in Fig. 5.9 (a) to (c), some changes on the surface are marked by differently colored arrows. Although their shapes change all the time, their overall sizes remain constant. Moreover, one should have in mind that the visible objects on the surface are molecule clusters rather than single molecule, since single molecule can not be resolved in LEEM. When the temperature reached  $80^{\circ}\text{C}$ , an evident reduction of their sizes was observed. An example is the large dark object marked by red circles shown in Fig. 5.9 (d) to (f). With further



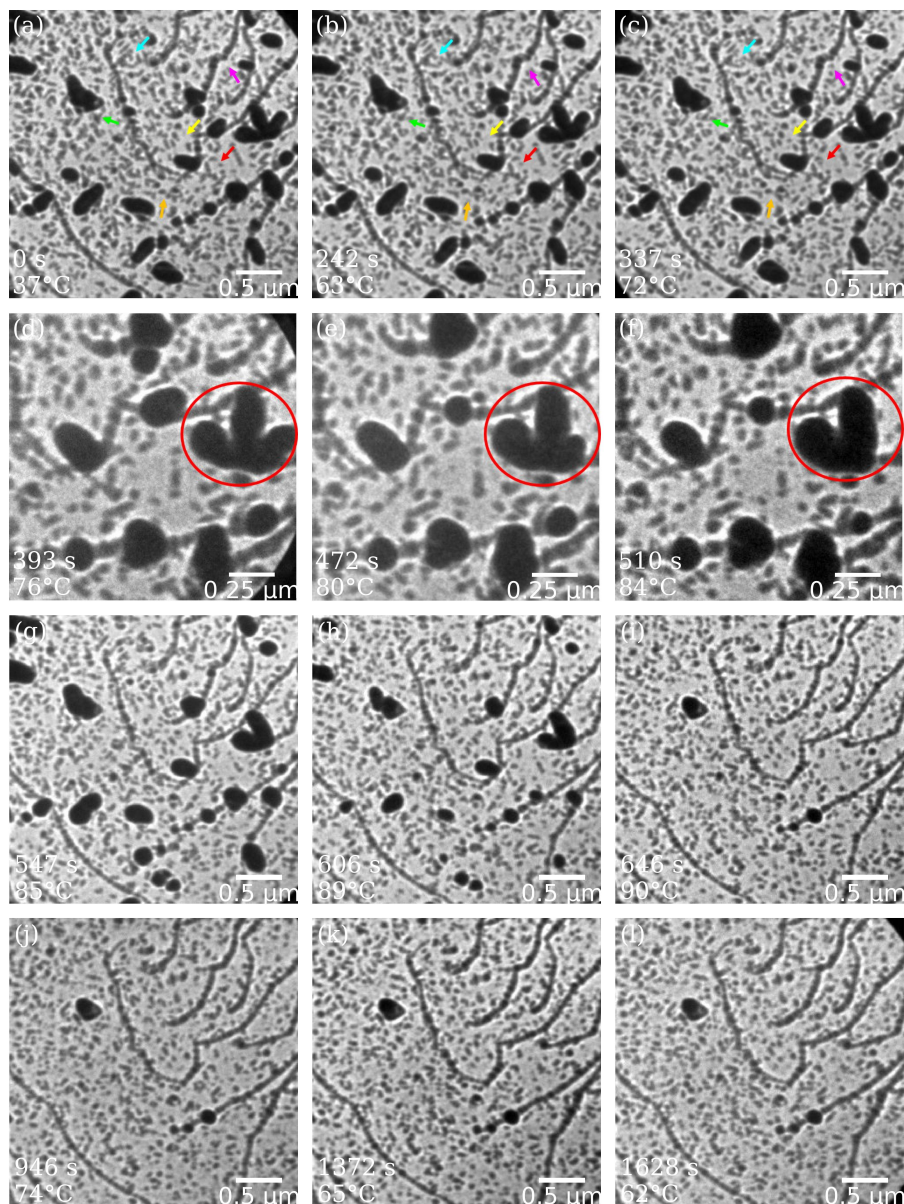


Figure 5.9: (a) to (l) LEEM images captured during the annealing to 90 °C. The labels in the bottom-left corner of each panel give the temperature and relative time with respect to image (a). The colored arrows in (a) to (c) mark the same area in each panel, respectively. All the LEEM images were captured with an electron energy of 0.8 eV.

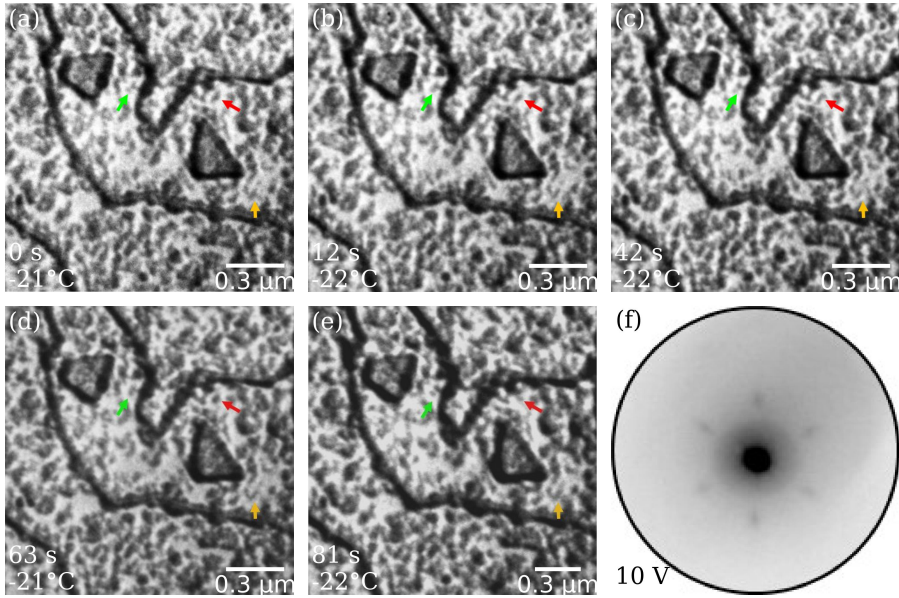


Figure 5.10: (a) to (e) LEEM images captured when the sample was cooled at around  $-20^{\circ}\text{C}$ . The labels in the bottom-left corner of each panel give the temperature and relative time with respect to image (a). The colored arrows in (a) to (e) mark the same area in each panel, respectively. All the LEEM images were captured with an electron energy of 0.8 eV. (f) LEED pattern obtained from the surface, and it was obtained with an electron energy of 10 eV.

increasing temperature to around  $90^{\circ}\text{C}$ , those large dark objects becomes even smaller. On the other hand, the overall sizes of the small gray objects show less changes, and are almost identical in this process. Fig. 5.9 (j) to (l) are three LEEM images taken during the cooling from  $90^{\circ}\text{C}$  to  $-20^{\circ}\text{C}$ , there are barely changes observed.

Even at around  $-20^{\circ}\text{C}$ , the small gray objects still exhibited high activity. Fig. 5.10 presents five LEEM images, panels (a) to (e), captured at different times. By comparing the small areas marked by differently colored arrows in each panel, changes on the surface can be identified. Only five single LEEM images from the image sequence are shown here, making it hard to follow the movement of the small gray objects. However, in the movie created from the image sequence, the

movement of these objects is clearly visible. Subsequent LEED measurements confirmed the presence of the ordered structure on the surface. The obtained LEED pattern is shown in Fig. 5.10 (f), where six diffraction spots around the (00) main spot remain, though with weaker intensity.

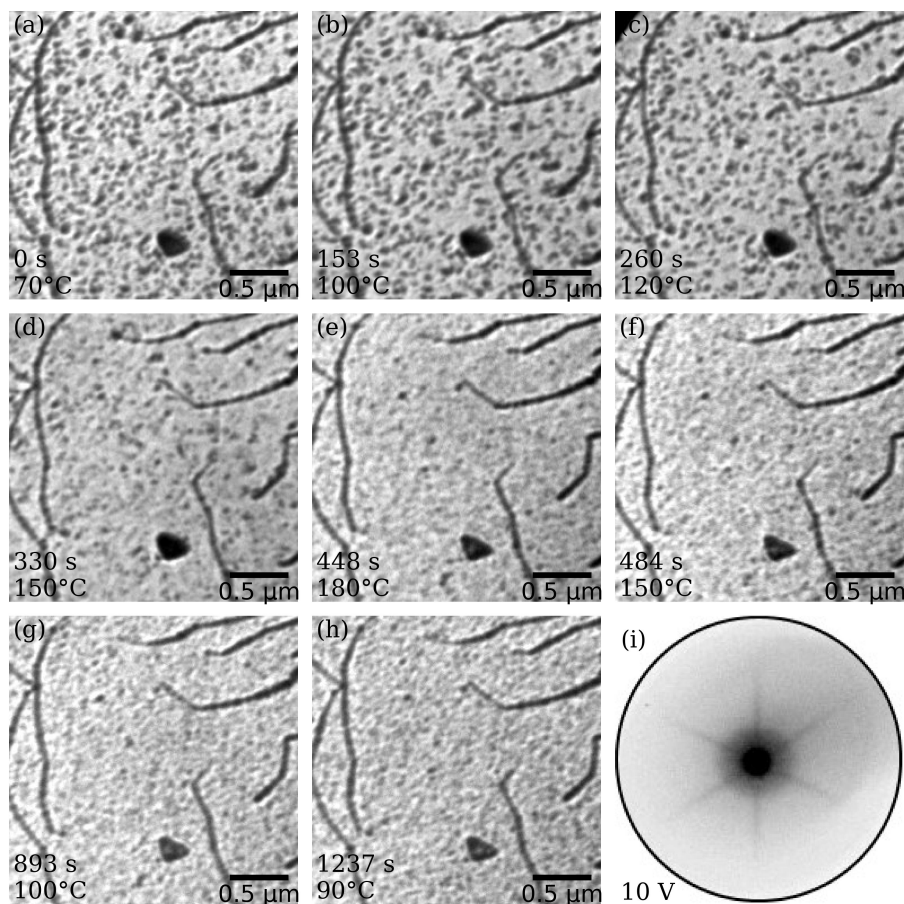


Figure 5.11: (a) to (h) LEEM images captured during the annealing to 180 °C. The labels in the bottom-left corner of each panel give the temperature and relative time with respect to image (a). All the LEEM images were captured with an electron energy of 1 eV. (i) LEED pattern obtained after cooling down to RT with an electron energy of 10 eV.

An explanation for the observation discussed above is that most of the molecules on the surface exist in a disordered state, even after the sample has been kept at room temperature for three days. These molecules aggregate into disordered 3D clusters, which appear as large dark objects in the LEEM images. Due to the weak attractive interactions between these molecules and the substrate, they easily evaporate into the vacuum as the substrate temperature increases. However, some molecules are arranged in an ordered manner, seen as small gray objects, and have a relatively strong interaction with the substrate. As a result, they remain on the surface even when the temperature is raised to 90 °C. The obtained LEED pattern after annealing to 90 °C also proves that those small gray objects consist of ordered arrangement of molecules.

To enable the opening of molecules, the sample was annealed to 180 °C and then cooled to room temperature (RT). LEEM images captured during this process are shown in Fig. 5.11. As the temperature exceeds 100 °C, even the small gray objects begin to dissolve, as evidenced by the significant reduction in their quantity from Fig. 5.11 (a) to (e). Most of the molecules that previously formed ordered structures also evaporate into the vacuum, inferred from the LEED pattern observed after heating, which shows only straight lines crossing the (00) main spot, with the six diffraction spots around the main spot no longer present, as shown in panel (i). Fig. 5.11 (f) to (h) display LEEM images taken during the cooling phase. As the temperature decreases, the surface appears rougher and more gray, comparing panel (h) to (e). This change indicates that during annealing, some molecules were activated by the high temperature and likely transitioned into the gas phase on the surface. Although some molecules may have escaped into the vacuum, some re-condensed onto the surface once the substrate temperature decreased. Therefore, only a little amount of molecules can be really catalyzed by the substrate, and open their rings. Moreover, in other experiments with higher coverage of molecules, we even observed the re-condensation of those large molecule clusters when the sample was cooling down from 180 °C to RT, as some large dark objects re-emerge during the cooling. A further annealing to higher temperature was not executed, since it appears not to be very useful due to the small amount of remaining clusters of molecules on the surface.

### 5.4 Summary

The deposition of [6]-CPP on Cu(111) was monitored using the LEEM technique, revealing rather high mobility of the molecules on the surface at RT. When the substrate temperature was lowered below  $-20^{\circ}\text{C}$ , the deposited molecules tended to form 3D clusters rather than 2D islands. This behavior is attributed to the low interaction between the molecules and the substrate, coupled with strong intermolecular interactions. The resulting clusters exhibited heights significantly greater than the atomic steps of the substrate and were in a disordered state, as evidenced by the absence of clear LEED patterns.

For the molecules to arrange in an ordered structure, a period of time for molecules to settle down was required, which in our case took three days at RT. Annealing the substrate to around  $25^{\circ}\text{C}$  facilitated the redistribution process, but this also introduced a potential issue, as ring-opening reactions could occur at this temperature. Although stabilization on a cold substrate may prevent such reactions, it significantly increases the time needed for the process.

The successful acquisition of proper LEED patterns from the surface demonstrated the formation of ordered structures. LEED measurements could only be conducted at a low energy range below 14 eV due to the extreme sensitivity of the [6]-CPP molecules to electron illumination. Beam damage was observed starting at 10 eV, with higher electron energies causing faster molecular degradation. Six first-order diffraction spots are located close to the central (00) spot in the obtained LEED pattern. Under certain conditions, second-order diffraction spots were also visible, however, due to the electron energy limitation, additional spots could not be observed. The LEED patterns suggest two possible orientations of the crystalline structures: either aligned with the substrate or rotated by  $30^{\circ}$ . Moreover, we observed some straight lines going across the LEED spots, and they are aligned with respect to the diffraction spots. Given the fact the molecules evaporate into the vacuum during annealing, the concentration of molecules on the surface decreases. This reduction can lead to enlarged unit cells, with sizes that differ and vary continuously.

When the substrate is annealed, the molecules become more mobile on the

surface. The molecules that are in disordered state, which appear as large dark objects, will first dissolve and go into the vacuum. The molecules that arranged within the ordered structures seem to be more stable, since the diffraction spots of ordered structure are still visible after the sample was annealed to 90 °C, while the big disordered objects on the surface disappear. Annealing to a higher temperature like 180 °C lets the ordered structures on the surface disappear completely. Due to the high mobility of molecules, we speculate that the most molecules will remain intact with their ring shape, and evaporate into the vacuum, with only a small number being catalyzed by the substrate to form long chains. Consequently, the diffraction spots of the superstructure vanish, and only some lines crossing the central (00) spot are visible in the LEED pattern after annealing to 180 °C.

The combination of [6]-CPP and Cu(111) forms a meta-stable system. While molecules can arrange in an ordered manner on the surface, a prolonged period is required for them to redistribute. The system's equilibrium is fragile and can be easily disrupted by temperature changes, causing the molecules to readily escape from the surface into the vacuum due to the weak interaction between them and the substrate. The ring-opening and polymerization at a high temperature is an attractive investigations, however, further investigation with the LEEM technique appears to be difficult due to the high desorption rate of the molecules.



## 6 Summary and Outlook

In this study, we employed a combination of LEEM and other investigation techniques to examine the properties of three different systems: The first, reported in **Chapter 3**, is the surface morphology of epitaxially grown  $0^\circ$ -rotated monolayer graphene and  $30^\circ$ -twisted multilayer graphene on a SiC substrate. In the second, we elucidated the hydrogen intercalation (and deintercalation) process involved in the formation of  $30^\circ$ -twisted bilayer graphene (TBG), see **Chapter 4**. And finally, in **Chapter 5**, we characterized the deposition and degradation behavior of a carbon-based cyclic molecule, [6]-CPP on a Cu(111) surface.

**Chapter 3** and **4** represent a continuation of the ongoing efforts to achieve a  $30^\circ$ -twist bilayer graphene (TBG). At first (**Chapter 3**), we examined the morphology of  $0^\circ$ -rotated monolayer graphene. This unusually oriented graphene layer was produced on a wafer scale with high quality through the surfactant-mediated epitaxial growth method on a 6H-SiC(0001) substrate [6]. The study demonstrates the impact of annealing temperature on the resulting surface morphology: Two samples were studied, which were annealed at temperatures that were only slightly different (by  $50^\circ\text{C}$ ), but showed very different results. The higher growth temperature ( $1380^\circ\text{C}$ ) caused the formation of graphene multilayers (in the conventional  $30^\circ$  orientation) underneath a topmost  $0^\circ$ -rotated graphene layer. At the lower temperature of  $1330^\circ\text{C}$ , the growth of the G- $R0^\circ$  layer is self-limiting, resulting in the formation of only one G- $R0^\circ$  layer located on the zeroth-layer graphene on SiC(0001). This structure presents a potential avenue for achieving  $30^\circ$ -TBG when the ZLG is decoupled from the substrate by



## Chapter 6. Summary and Outlook

---

intercalation. A remarkable result of the study on this sample is that we were able to observe the initial growth of  $30^\circ$ -TBG at the step edges within a lateral range of approximately 150 nm, already at a temperature of 1330 °C. The remaining majority of the surface is high-quality G- $R0^\circ$ /ZLG- $R30^\circ$  stack, exhibiting only a low density of point defects.

Not unexpectedly, the growth of the underlying G- $R30^\circ$  layers is promoted by higher temperatures, but already an increase of only 50 °C leads to uncontrollable multilayer growth. The sample surface turns into an inhomogeneous carpet of multilayer domains with different numbers of layers. To interpret the various graphene domains with distinct stacking layers, a comprehensive, pixel-by-pixel analysis of LEEM-*IV* data was performed: LEEM-*IV* spectra were extracted pixel-by-pixel and analyzed regarding their curve profiles. This allows for counting the graphene layers on the surface, since the *IV* spectra reflect the inherent electronic band structures of the graphene stacks. This procedure yields the distribution of the domains with different layer numbers, at a spatial resolution down to 10 nm.

The investigation on this sample revealed that a homogeneous TBG sample cannot be obtained by temperature-induced decoupling of the ZLG, but that inhomogeneous multilayer-growth occurs. This is the reason for selecting intercalation as an alternative mean of achieving the desired TBG. In **Chapter 4**, we hence addressed the intercalation of hydrogen in a  $0^\circ$ -rotated epitaxial monolayer of graphene, with the goal of attaining a  $30^\circ$ -twisted bilayer graphene (TBG) configuration. To address the ongoing debate regarding the mechanisms of hydrogen intercalation, the process was conducted stepwise, thereby allowing for the examination of the intermediate stages. The intercalated and non-intercalated regions exhibited sharp boundaries that ran parallel to the step edges. This indicates that the hydrogen atoms infiltrate the graphene layer at discontinuities in the graphene layer, in particular at step edges of the substrate, and diffuse far into the terraces. The parallel movement of these boundaries across the terrace is observable due to the high quality of the top graphene layer produced via "surfactant-mediated growth", since only few discontinuities were present within the terraces.

---

After a total intercalation time of more than 10 hours, the presence of the TBG was confirmed through the extracted  $IV$  spectra, proving the bilayer stacking configuration all over the surface. However, we also found a persisting brightness contrast on all surface terraces, that was clearly not associated with the stacking configuration. In light of the elongation of the graphene diffraction spots in the azimuthal direction observed in the LEED pattern, a potential explanation for the brightness contrast may be attributed to slight deviations in the twist angles between the two graphene layers, which deviate from  $30^\circ$ .

The observation of the deintercalation process was conducted on another sample, the surface of which was initially partially covered by a monolayer of graphene ( $G-R0^\circ/ZLG-R30^\circ$ ) and by bilayer of graphene ( $G-R0^\circ/G-R30^\circ/ZLG-R30^\circ$ ). Some smaller regions were even exhibiting triple layers. For this sample, the hydrogen intercalation resulted in the decoupling of the ZLG from the substrate, specifically beneath the regions of monolayer graphene, leading to the creation of a  $30^\circ$ -TBG configuration. In contrast, the bilayer and triple-layer areas retained their original stacking configurations, i.e., no intercalation took place for these regions. This indicates that areas with a lower number of graphene layers are more susceptible to intercalation, which is consistent with the intuitive expectation that it is more challenging for hydrogen to go underneath the ZLG on a surface with multiple coverage of graphene layers. Hydrogen intercalation occurs at approximately  $640^\circ\text{C}$ , and annealing at temperatures exceeding  $200^\circ\text{C}$  can result in the reversal of the process. The process of deintercalation varies greatly from the intercalation process: It occurred rapidly, within approximately one minute, and uniformly as indicated by a homogeneous change of the LEEM brightness, simultaneous on the entire surface. This happens at temperatures exceeding  $800^\circ\text{C}$ , which may facilitate the motion of carbon atoms within the graphene layer, thereby allowing for the penetration of hydrogen atoms through the graphene layers. Furthermore, the annealing-induced strain in the graphene layer may result in the formation of additional crystalline defects, thereby providing additional pathways for hydrogen atom to escape. However, this cannot be proven unambiguously, a strongly increased diffusion velocity of Hydrogen atoms underneath the graphene layers might lead to similar observations.

We also note that the homogeneous and simultaneous change in surface bright-

## Chapter 6. Summary and Outlook

---

ness during deintercalation makes it difficult to observe this process, since no reference points are available on homogeneous surfaces. Areas with different stacking, like the bilayer (stacked as  $G-R0^\circ/G-R30^\circ/ZLG-R30^\circ$ ) and triple layer regions on our sample are therefore crucial for observing the process, as they remain unchanged throughout the deintercalation process and hence provide the reference points.

In conclusion, we believe that this work has enhanced the understanding of the intercalation and deintercalation mechanism of the ZLG on SiC, and possibly for the first time, produced a large-scaled epitaxial  $30^\circ$ -TBG. Furthermore, a very homogeneous unconventionally  $0^\circ$ -rotated monolayer graphene (EMLG) could be studied in detail. This demonstrates the efficiency of LEEM in probing the epitaxial graphene on SiC system. In the future, in collaboration with our colleagues in Regensburg, we will examine the ultrafast dynamics of lateral electrical currents at various graphene/SiC interfaces. The TBG will play a prominent role in this context. The objective is to identify and quantify the electron scattering processes that ultimately restrict the performance of cutting-edge electronic devices based on interface electronic states or two-dimensional semiconductors. The graphene/SiC interfaces do not facilitate electrical conductivity; instead, they act as inevitable scattering points that result in current decay. Epitaxial graphene on SiC represents a promising system for this study, given the well-defined and controllable nature of its interface, which can be precisely tuned through the application of different preparation parameters in UHV. The investigation will be conducted utilizing the THz angle-resolved photoemission spectroscopy (THz-ARPES) technique, which employs a robust terahertz electric field coupled with a high-harmonic laser source for ARPES. The fundamental premise entails the illumination of electrons situated within the  $\pi$  band, which are situated above the  $K$  points of the graphene Dirac cones. A strong THz electric field subsequently propels the electrons in question back and forth at high speed, while high-resolution ARPES tracks their scattering and decay behavior, thus providing valuable insight into the non-equilibrium dynamics of electrons.

In the last part of the thesis (**Chapter 5**), we report a study on the deposition of [6]-Cycloparaphenylene ([6]-CPP) molecules on a Cu(111) substrate. In

---

contrast with the anticipated formation of an ordered two-dimensional (2D) layer in a herringbone pattern, these molecules demonstrated a tendency for agglomerating into three-dimensional (3D) clusters as they reached the surface. It was observed that the 3D molecular clusters are higher than the atomic layers of the substrate, and do not show any crystalline order, since no LEED pattern was observed. The molecules on the surface exhibit high mobility, as evidenced by the redistribution of molecules between clusters. This phenomenon was observed even when the surface was cooled to  $-60^{\circ}\text{C}$ . Some clusters grew in size while others shrank. This suggests that the interaction between the molecules and the substrate may be weaker than the attractive interactions between the  $\pi$  systems of the molecules themselves.

Following a stabilization period of three days at room temperature ( $25^{\circ}\text{C}$ ), two distinct crystalline orientations were observed: one aligned with the substrate lattice and another rotated by  $30^{\circ}$ . Nevertheless, despite a three-day stabilization period at room temperature, the majority of the molecules persisted in their disordered state, while only a small number of the molecules exhibited an ordered arrangement. Additionally, it was observed that [6]-CPP molecules are susceptible to beam-induced damage. When the electron energy exceeds 10 eV, substantial molecular degradation occurs.

Furthermore, we observed that upon annealing the system to approximately  $90^{\circ}\text{C}$ , the disordered molecular clusters evaporated into the vacuum, while the ordered structures remained on the surface. The ordered structures only disappear upon annealing at a higher temperature ( $180^{\circ}\text{C}$ ), and it can be assumed that they also evaporate from the surface. The observed behavior indicates that in the ordered structure the molecules are more strongly bonded to the substrate than in the disordered arrangement. This may be due to a surface-induced "opening" of the molecular ring, i.e., the transformation of the ring-like molecule into a long PPP chain, which was suggested from earlier STM measurements. However, the amount of molecules undergoing this transformation was not sufficiently high for any further investigation with the LEEM instrument, since no (sub-) molecular resolution can be reached. For following up on this project, more deposition experiments, and maybe also alternative experimental techniques have to be applied, which allow a more homogeneous deposition of (mono)

## Chapter 6. Summary and Outlook

---

layers of [6]-CPP, and an imaging method providing molecular resolution.

## A *K-means* Codes for the Pixel-by-Pixel Analysis

In this work, we implemented a pixel-by-pixel method for LEEM-*IV* data analysis, utilizing both user-defined manual clustering and semi-automatic algorithm-based clustering through *K-means*. Both approaches rely on Python-based scripts. In this appendix, the codes applied to generate the Fig. 4.7 are given as an example to introduce the necessary packages and procedures for performing *K-means* based analysis.

To generate plots and present the clustering results in a visually appealing way, the use of **matplotlib** is essential. The raw LEEM-*IV* data is an image sequence consisting of  $(x \times y \times z)$  data points, where  $(x \times y)$  represents the pixel dimensions of each image, and  $(z)$  is the number of images in the sequence. These images are captured and stored in **DAT files (.dat)**. ImageJ can open the images, perform shift correction, cut out areas, and save them to an image sequence file in a format of **(.tif)**. To read these files in python, the **tifffile** package is required. The data format needs to be transformed from individual intensity values in a 3D array to 1D or 2D arrays, where each component contains a sequence of intensity values (similar to a curve). To store the extracted data from the image sequence, empty 1D or 2D arrays must first be created, which is done using the **numpy** library.

The **Image** module, from Python's **Pillow (PIL)** library, is used for image processing, allowing the opening of image files in formats like **(.jpg)** and **(.png)**. The **savgol\_filter** and **find\_peaks** modules from the **scipy.signal** library are used for

## Appendix A. *K-means* Codes for the Pixel-by-Pixel Analysis

---

curve processing, such as smoothing noise in the data and identifying peaks in the smoothed curves. The **AnchoredSizeBar** module is applied to define the position of the scale bar when displaying LEEM images or false color composite images in plots. The **KMeans** module, a core component of the code described here, is imported from the **sklearn.cluster** library for clustering analysis. Finally, **ListedColormap** is used to create custom color maps for differentiating data groups and interpreting clustering results.

```
1 import matplotlib.pyplot as plt
2 import tiff file
3 import numpy as np
4 from PIL import Image
5 from scipy.signal import savgol_filter, find_peaks
6 from mpl_toolkits.axes_grid1.anchored_artists import AnchoredSizeBar
7 from sklearn.cluster import KMeans
8 from matplotlib.colors import ListedColormap
```

The following codes open the data files.

```
1 path = 'C:/Users/h.yin/Desktop/PhD Thesis/images/Chapter Hydrogen
         Intercalation/Deintercalation/'
2 im = tiff file.imread(path + 'Before deinter.tif') # Open the (tif)
         file containing the image sequence
3 im_63 = Image.open(path + 'Before LEEM 4,2 eV.jpg') # Open an image
```

The following codes define the curves length, curve ranges for the following *K-means* clustering, and displayed energy range in the final plot. It is not necessary to use the full-length curves for *K-means* clustering. It is recommended to restrict the curves to a specific energy range for clustering, as this can significantly reduce computational resources and processing time.

```
1 E_st = 26 # Define the starting point of the curve for K-means
         processing, from the 27th data point of the curve
2 E_end = 70 # Define the ending point of the curve for K-means
         processing, end at the 71th data point of the curve
3 energy_k = np.arange(E_st/10, E_st/10+(E_end-E_st)*0.1, 0.1) # Define
         the array of energy range for K-means processing, 0.1 is the energy
         step of 0.1 eV
4 energy = np.arange(-1, 7, 0.1) # Define the energy range that will be
         displayed in the final plot
```

The following codes read out the size of data, and define new arrays to contain

extracted data.

```
1 array_shap = np.shape(im) # Read out the size of the row data 'im'
2 result_array = np.zeros(array_shap[1]*array_shap[2]) # Create a 1D
  array to contained extracted single curves
3 result_image = np.zeros((array_shap[1],array_shap[2])) # Create a 2D
  array, each cell will be numbered according to the clustering
  results, and will be used to generate the false-color image
4 new_TD_array = np.zeros((array_shap[1]*array_shap[2], E_end-E_st)) #
  Create a 2D array to contain the cut out curves
5 TD_array = np.zeros((array_shap[1]*array_shap[2], 80)) # Create a 2D
  array to contain the curves that will be displayed in the final
  plot
```

The following codes define the custom color-codes.

```
1 colorcodes = ['#008000', 'red', '#0000FF']
```

Before obtaining the final clustering results, it is essential to perform a test clustering to determine the appropriate  $K$  value. The following code demonstrates how to conduct test clustering and save the results.

```
1 k = int(input('Enter the K value: \n')) # Give a K value
2
3 a=0
4
5 for pos_x in range(array_shap[1]):
6     for pos_y in range(array_shap[2]):
7         iv = im[E_st:E_end, pos_x, pos_y]
8         iv_savgol = savgol_filter(iv, window_length=13, polyorder=3,
          deriv=0)
9         new_TD_array[a] = iv_savgol
10        a += 1
11 # Extract the $IV$ curve in the range from E_st to E_end, smooth the
  extracted curves and store them in to the predefined array (
  new_TD_array)
12
13 kmeans = KMeans(n_clusters= k, init='random', n_init=10, random_state
  =0)
14 kmeans.fit(new_TD_array)
15 # Call the KMeans module, and apply the module to process the
  extracted curve array, which generates a codebook where each curve
  is assigned a unique label. Curves belonging to the same cluster
  will share the same label number
16
17 np.save("kmeans_label.npy", kmeans.labels_)
18 # Save the codebook for later call.
```



## Appendix A. *K-means* Codes for the Pixel-by-Pixel Analysis

```
19
20 for j in range(k):
21     fig, axe = plt.subplots(figsize = (2.1,1.7), layout = '
        constrained')
22     for i in range(array_shap[1]*array_shap[2]):
23         if kmeans.labels_[i] == j:
24             axe.plot(energy[E_st:E_end], new_TD_array[i], '-', color
                = colorcodes[0], alpha = 0.01)
25     axe.set_ylim(0,800)
26     axe.tick_params(axis='both', labels=7)
27     axe.set_ylabel('Intensity (a.u.)',size=9)
28     axe.set_xlabel('E (eV)',size=9)
29     fig.savefig(f'K={k}, class{j}.png', dpi = 600)
30 # Save the test clustering results as K numbers of plots for further
    clustering
```

Generally, *K-means* does not achieve fully automatic clustering with perfect results, particularly for data containing various curve profiles. It is employed to streamline the clustering process and save time by initially sorting the curves into  $K$  sub-clusters that exhibit high similarity within each group. However, manual assignment is still necessary, but with significantly fewer objects. In the code presented in the appendix,  $K = 30$  was determined to be an appropriate value. Through manual assignment, these 30 sub-clusters are further grouped into three distinct clusters.

```
1 kmeans_labels_ = np.load('kmeans_label.npy')
2 # Load the saved codebook
3
4 list_1 = [2, 5, 6, 7, 10, 14, 15, 17, 19, 22, 25, 26]
5 list_2 = [1, 4, 8, 9, 11, 12, 13, 18, 20, 21, 23, 27, 28, 29]
6 list_3 = [0, 3, 16, 24]
7 # Define the three lists according to the manual assignment
8
9 b=0
10 c=0
11
12 m=0
13 n=0
14 o=0
15
16 list_1_average = np.zeros(80)
17 list_2_average = np.zeros(80)
18 list_3_average = np.zeros(80)
19 # Define three empty arrays to contained the sum of curves in each
    list for calculating the averaged curve of each list
```

---

```

20
21 for pos_x in range(array_shap[1]):
22     for pos_y in range(array_shap[2]):
23         new_iv = im[10:90, pos_x, pos_y]
24         new_iv_savgol = savgol_filter(new_iv, window_length=13,
25                                     polyorder=2, deriv=0)
26         TD_array[b] = new_iv_savgol
27         b += 1
28 # Extract the $IV$ curves in the energy range that will be displayed
29 # in the final plot

```

The size and format of the final plot need to be defined, therefore, all curves, and curve average can be plotted in different panels.

```

1 fig, axs = plt.subplots(2,3,figsize = (6.4,4.3), layout = '
2     constrained')
3 # Define the size and format of the final plot
4
5 for i in range(array_shap[1]*array_shap[2]):
6     if kmeans_labels_[i] in list_1:
7         axs[0,1].plot(energy[0:80], TD_array[i], '--', color =
8             colorcodes[0], alpha = 0.01)
9         result_array[i]=1 # Re-number single curves into three
10            clusters
11         list_1_average += TD_array[i]
12         m += 1
13     if kmeans_labels_[i] in list_2:
14         axs[0,2].plot(energy[0:80], TD_array[i], '--', color =
15             colorcodes[1], alpha = 0.01)
16         result_array[i]=2 # Re-number single curves into three
17            clusters
18         list_2_average += TD_array[i]
19         n += 1
20     if kmeans_labels_[i] in list_3:
21         axs[1,1].plot(energy[0:80], TD_array[i], '--', color =
22             colorcodes[2], alpha = 0.01)
23         result_array[i]=3 # Re-number single curves into three
24            clusters
25         list_3_average += TD_array[i]
26         o += 1
27 # Plot all the curves in three panels
28
29 for pos_x in range(array_shap[1]):
30     for pos_y in range(array_shap[2]):
31         result_image[pos_x, pos_y] = result_array[c]
32         c += 1
33 # Convert a 1D array to a 2D array for false-color image

```

## Appendix A. *K-means* Codes for the Pixel-by-Pixel Analysis

---

```
28 list_1_average /= m
29 axs[0,1].plot(energy[0:80], list_1_average, linewidth=1, color = '
    white')
30 axs[1,2].plot(energy[0:80], list_1_average, linewidth=2, color =
    colorcodes[0])
31
32 list_2_average /= n
33 axs[0,2].plot(energy[0:80], list_2_average, linewidth=1, color = '
    white')
34 axs[1,2].plot(energy[0:80], list_2_average, linewidth=2, color =
    colorcodes[1])
35
36 list_3_average /= o
37 axs[1,1].plot(energy[0:80], list_3_average, linewidth=1, color = '
    white')
38 axs[1,2].plot(energy[0:80], list_3_average, linewidth=2, color =
    colorcodes[2])
39 # Calculate the average curve of each cluster, and plot them
40
41 axs[0,1].set_title('cluster I',size=10)
42 axs[0,1].set_ylim(100, 900)
43 axs[0,1].set_xlim(0, 7)
44 axs[0,1].set_xticks([0, 1, 2, 3, 4, 5, 6, 7])
45 axs[0,1].tick_params(axis='both', direction = 'out', top = False,
    labels=7)
46 axs[0,1].set_xticklabels([])
47 axs[0,1].set_xticks([])
48 axs[0,1].set_ylabel('Intensity (a.u.)',size=9)
49 axs[0,1].text(0, 928, '(c)', color='k', fontsize=10, va='bottom',
    fontfamily='serif')
50
51 axs[0,2].set_title('cluster II',size=10)
52 axs[0,2].set_ylim(100, 900)
53 axs[0,2].set_xlim(0, 7)
54 axs[0,2].set_xticks([0, 1, 2, 3, 4, 5, 6, 7])
55 axs[0,2].set_yticks([])
56 axs[0,2].set_xticks([])
57 axs[0,2].tick_params(axis='both', direction = 'out', top = False,
    labels=7)
58 axs[0,2].set_xticklabels([])
59 axs[0,2].text(0, 928, '(d)', color='k', fontsize=10, va='bottom',
    fontfamily='serif')
60
61 axs[1,1].set_title('cluster III',size=10)
62 axs[1,1].set_ylim(100, 900)
63 axs[1,1].set_xlim(0, 7)
64 axs[1,1].set_xlabel('E (eV)',size=9)
65 axs[1,1].set_xticks([0, 1, 2, 3, 4, 5, 6, 7])
```

---

```

66  axs[1,1].tick_params(axis='both', direction = 'out', top = False,
    labelsiz=7)
67  axs[1,1].set_ylabel('Intensity (a.u.)',size=9)
68  axs[1,1].text(0, 928, '(e)', color='k', fontsize=10, va='bottom',
    fontfamily='serif')
69
70  axs[1,2].set_title('averaged curves',size=10)
71  axs[1,2].set_ylim(100, 900)
72  axs[1,2].set_xlim(0, 7)
73  axs[1,2].set_xlabel('E (eV)',size=9)
74  axs[1,2].set_xticks([0, 1, 2, 3, 4, 5, 6, 7])
75  axs[1,2].set_yticks([])
76  axs[1,2].plot((4.08,4.08),(120,440), 'k', linestyle= '--',linewidth
    =1)
77  axs[1,2].tick_params(axis='both', direction = 'out', top = False,
    labelsiz=7)
78  axs[1,2].text(0, 928, '(f)', color='k', fontsize=10, va='bottom',
    fontfamily='serif')
79
80
81  axs[0,0].imshow(im_63, cmap='gray')
82  axs[0,0].set_xticks([])
83  axs[0,0].set_yticks([])
84  axs[0,0].set_axis_off()
85  axs[0,0].set_title('BF LEEM', size=10)
86  scalebar = AnchoredSizeBar(axs[0,0].transData,50, '0.5 \u03bcm', '
    lower right',pad=0.1,color='white',frameon=False, size_vertical=3)
87  axs[0,0].add_artist(scalebar)
88  axs[0,0].text(0, -13.0, '(a)', color='k', fontsize=10, va='bottom',
    fontfamily='serif')
89  axs[0,0].text(0, 250, '4.1 eV', color='white', fontsize=9, va='bottom
    ', fontfamily='serif')
90
91  custom_cmap = ListedColormap(colorcodes)
92  axs[1,0].imshow(result_image, cmap=custom_cmap, interpolation='
    nearest')
93  axs[1,0].set_xticks([])
94  axs[1,0].set_yticks([])
95  axs[1,0].set_axis_off()
96  axs[1,0].set_title('FC image', size=10)
97  co = axs[1,0].imshow(result_image, cmap=custom_cmap, interpolation='
    nearest')
98  bounds = [0.5, 1.5, 2.5]
99  cbr = fig.colorbar(co, ax=axs[1,0], ticks = bounds, location = 'bottom
    ', orientation='horizontal', fraction=0.06, pad=0.001)
100  cbr.ax.set_xticklabels(['I', 'II', 'III'], fontsize=7)
101  scalebar = AnchoredSizeBar(axs[1,0].transData,50, '0.5 \u03bcm', '
    lower right',pad=0.1,color='white',frameon=False, size_vertical=3)

```

## Appendix A. *K-means* Codes for the Pixel-by-Pixel Analysis

---

```
102  axs[1,0].add_artist(scalebar)
103  axs[1,0].text(0, -13.0, '(b)', color='k', fontsize=10, va='bottom',
104      fontfamily='serif')
105  # Define the details of the of the final plot
106  fig.savefig('Figure Before_Deintercalation.png', dpi = 600)
107  # Save the final plot
```

## Bibliography

- [1] U. Starke and C. Riedl, J. Phys.: Condens. Matter **21**, 134016 (2009).
- [2] C. Riedl, C. Coletti, T. Iwasaki, A. Zakharov, and U. Starke, Phys. Rev. Lett. **103** (2009).
- [3] J. L. Miller, Physics Today **71**, 15 (2018).
- [4] J.-L. Xia and R. Jasti, Angew. Chem. Int. Ed. **51**, 2474 (2012).
- [5] S. N. Spisak, Z. Wei, E. Darzi, R. Jasti, and M. A. Petrukhina, Chem. Commun. **54**, 7818 (2018).
- [6] F. C. Bocquet, Y.-R. Lin, M. Franke, N. Samiseresht, S. Parhizkar, S. Soubatch, T.-L. Lee, C. Kumpf, and F. S. Tautz, Phys. Rev. Lett. **125**, 106102 (2020).
- [7] C. Davisson and L. H. Germer, Phys. Rev. **30**, 705 (1927).
- [8] E. Bauer, Ultramicroscopy **17**, 51 (1985), ISSN 0304-3991.
- [9] B. Stadtmüller, J. Seidel, N. Haag, L. Grad, C. Tusche, G. v. Straaten, M. Franke, J. Kirschner, C. Kumpf, M. Cinchetti, et al., Phys. Rev. Lett. **117** (2016).
- [10] C. Henneke, J. Felter, D. Schwarz, F. S. Tautz, and C. Kumpf, Nat. Mater. **16**, 628 (2017).
- [11] J. Felter, M. Franke, J. Wolters, C. Henneke, and C. Kumpf, Nanoscale **11**, 1798 (2019).

## Bibliography

---

- [12] D. Schwarz, C. Henneke, and C. Kumpf, *New J. Phys.* **18**, 023034 (2016).
- [13] J. Felter, M. Raths, M. Franke, and C. Kumpf, *2D Mater.* **6** (2019).
- [14] M. Raths, C. Schott, J. Knippertz, M. Franke, Y. Lin, A. Haags, M. Aeschli-  
mann, C. Kumpf, and B. Stadtmüller, *Phys. Rev. Materials* **5** (2021).
- [15] C. Herrmann, K. L. Kavanagh, M. Raths, and C. Kumpf, *Sur. Sci.* **721**,  
122080 (2022).
- [16] H. W. Kroto, J. R. Heath, S. O'Brien, R. F. Curl, and R. E. Smalley, *Nature*  
**318**, 162 (1985).
- [17] S. Iijima, *Nature* **354**, 56 (1991).
- [18] F. Durola, *Angew. Chem. Int. Ed.* **51**, 6820 (2012).
- [19] K. S. Novoselov, A. K. Geim, S. V. Morozov, D. Jiang, Y. Zhang, S. V. Dubonos,  
I. V. Grigorieva, and A. A. Firsov, *Science* **306**, 666–669 (2004).
- [20] K. S. Novoselov, D. Jiang, F. Schedin, T. J. Booth, V. V. Khotkevich, S. V.  
Morozov, and A. K. Geim, *Proc Natl Acad Sci USA.* **102**, 10451 (2005).
- [21] K. S. Novoselov, A. K. Geim, S. V. Morozov, D. Jiang, M. I. Katsnelson, I. V.  
Grigorieva, S. V. Dubonos, and A. A. Firsov, *Nature* **438**, 197–200 (2005),  
ISSN 1476-4687.
- [22] Y.-B. Zhang, Y.-W. Tan, H. L. Stormer, and P. Kim, *Nature* **438**, 201–204  
(2005), ISSN 1476-4687.
- [23] S. Stankovich, D. A. Dikin, G. H. Dommett, K. M. Kohlhaas, E. J. Zimney,  
E. A. Stach, R. D. Piner, S. T. Nguyen, and R. S. Ruoff, *Nature* **442**, 282–286  
(2006).
- [24] J. C. Meyer, A. K. Geim, M. I. Katsnelson, K. S. Novoselov, T. J. Booth, and  
S. Roth, *Nature* **446**, 60–63 (2007), ISSN 1476-4687.
- [25] A. K. Geim and K. S. Novoselov, *Nat. Mater.* **6**, 183 (2007).
- [26] A. K. Worku and D. W. Ayele, *Results in Chemistry* **5**, 100971 (2023), ISSN  
2211-7156.

- [27] B. Partoens and F. M. Peeters, *Phys. Rev. B* **74**, 075404 (2006).
- [28] C. Virojanadara, M. Syväjarvi, R. Yakimova, L. I. Johansson, A. A. Zakharov, and T. Balasubramanian, *Phys. Rev. B* **78**, 245403 (2008).
- [29] C. Riedl, C. Coletti, and U. Starke, *J. Phys. D: Appl. Phys.* **43**, 374009 (2010).
- [30] P. Sutter, J. Sadowski, and E. Sutter, *Phys. Rev. B* **80**, 245411 (2009).
- [31] W. Yao, E. Wang, K. Deng, S. Yang, W. Wu, A. V. Fedorov, S. Mo, E. F. Schwier, M. Zheng, Y. Kojima, et al., *Phys. Rev. B* **92**, 115421 (2015).
- [32] I. Pletikosić, M. Kralj, P. Pervan, R. Brako, J. Coraux, A. T. N'Diaye, C. Busse, and T. Michely, *Phys. Rev. Lett.* **102** (2009), ISSN 1079-7114.
- [33] W. Liu, H. Li, C. Xu, Y. Khatami, and K. Banerjee, *Carbon* **49**, 4122 (2011).
- [34] T. H. Bointon, M. D. Barnes, S. Russo, and M. F. Craciun, *Adv. Mater.* **27**, 4200–4206 (2015), ISSN 1521-4095.
- [35] M. Saeed, Y. Alshammari, S. A. Majeed, and E. Al-Nasrallah, *Molecules* **25**, 3856 (2020).
- [36] Y. Gogotsi and V. Presser, CRC Press (2013).
- [37] K. V. Emtsev, A. Bostwick, K. Horn, J. Jobst, G. L. Kellogg, L. Ley, J. L. McChesney, T. Ohta, S. A. Reshanov, J. Röhrhl, et al., *Nat. Mater.* **8**, 203 (2009).
- [38] S. N. Luxmi, R. M. Feenstra, and P. J. Fisher, *J. Vac. Sci. Technol. B* **28**, C5C1–C5C7 (2010).
- [39] M. Kruskopf, D. M. Pakdehi, K. Pierz, S. Wundrack, R. Stosch, T. Dziomba, M. Götz, J. Baringhaus, J. Aprojanz, C. Tegenkamp, et al., *2D Mater.* **3**, 041002 (2016).
- [40] D. M. Pakdehi, J. Aprojanz, A. Susloparova, K. Pierz, M. Kruskopf, P. Willke, J. Baringhaus, J. P. Stöckmann, G. A. Traeger, F. Hohls, et al., *ACS Appl. Mater. Interfaces* **10**, 6039 (2018).



## Bibliography

---

- [41] D. Momeni Pakdehi, P. Schädlich, T. T. N. Nguyen, A. A. Zakharov, S. Wundrack, E. Najafidehaghani, F. Speck, K. Pierz, T. Seyller, C. Tegenkamp, et al., *Adv. Func. Mater.* **30**, 2004695 (2020).
- [42] A. Chatterjee, M. Kruskopf, S. Wundrack, P. Hinze, K. Pierz, R. Stosch, and H. Scherer, *ACS Appl. Electron. Mater.* **4**, 5317 (2022).
- [43] J. Schardt, J. Bernhardt, U. Starke, and K. Heinz, *Phys. Rev. B* **62**, 10335 (2000).
- [44] K. Heinz, J. Bernhardt, J. Schardt, and U. Starke, *J. Phys.: Condens. Matter* **16**, S1705 (2004).
- [45] C. Berger, Z. Song, T. Li, X. Li, A. Ogbazghi, R. Feng, Z. Dai, A. Marchenkov, E. H. Conrad, P. N. First, et al., *J. Phys. Chem. B* **108**, 19912 (2004).
- [46] C. Berger, Z. Song, X. Li, X. Wu, N. Brown, C. Naud, D. Mayou, T. Li, J. Hass, A. Marchenkov, et al., *Science* **312**, 1191 (2006).
- [47] T. Ohta, A. Bostwick, T. Seyller, K. Horn, and E. Rotenberg, *Science* **313**, 951 (2006).
- [48] P. Mallet, F. Varchon, C. Naud, L. Magaud, C. Berger, and J. Veuillen, *Phys. Rev. B* **76** (2007).
- [49] C. Riedl, U. Starke, J. Bernhardt, M. Franke, and K. Heinz, *Phys. Rev. B* **76** (2007).
- [50] C. Riedl, A. Zakharov, and U. Starke, *Appl. Phys. Lett.* **93** (2008).
- [51] J. Jobst, D. Waldmann, F. Speck, R. Hirner, D. K. Maude, T. Seyller, and H. B. Weber, *Phys. Rev. B* **81** (2010).
- [52] F. Speck, J. Jobst, F. Fromm, M. Ostler, D. Waldmann, M. Hundhausen, H. B. Weber, and T. Seyller, *Appl. Phys. Lett.* **99** (2011).
- [53] S. Ji, J. B. Hannon, R. M. Tromp, V. Perebeinos, J. Tersoff, and F. M. Ross, *Nat. Mater.* **11**, 114 (2011).

- [54] P. Willke, M. A. Schneider, and M. Wenderoth, *Ann. Phys.* **529**, 1700003 (2017).
- [55] K. Clark, X. Zhang, I. Vlassiouk, G. He, R. M. Feenstra, and A. Li, *ACS Nano* **7**, 7956 (2013).
- [56] P. Willke, T. Druga, R. G. Ulbrich, M. A. Schneider, and M. Wenderoth, *Nat. Commun.* **6** (2015).
- [57] A. Sinterhauf, G. A. Traeger, D. M. Pakdehi, P. Schädlich, P. Willke, F. Speck, T. Seyller, C. Tegenkamp, K. Pierz, H. W. Schumacher, et al., *Nat. Commun.* **11** (2020).
- [58] A. Mattausch and O. Pankratov, *Phys. Rev. Lett.* **99** (2007).
- [59] K. V. Emtsev, F. Speck, T. Seyller, L. Ley, and J. Riley, *Phys. Rev. B* **77** (2008).
- [60] I. Gierz, T. Suzuki, R. T. Weitz, D. S. Lee, B. Krauß, C. Riedl, U. Starke, H. Höchst, J. H. Smet, C. R. Ast, et al., *Phys. Rev. B* **81** (2010).
- [61] K. V. Emtsev, A. Zakharov, C. Coletti, S. Forti, and U. Starke, *Phys. Rev. B* **84** (2011).
- [62] G. Profeta, M. Calandra, and F. Mauri, *Nat. Phys.* **8**, 131 (2012).
- [63] C. Xia, S. Watcharinyanon, A. Zakharov, R. Yakimova, L. Hultman, L. I. Johansson, and C. Virojanadara, *Phys. Rev. B* **85** (2012).
- [64] S. Forti, A. Stöhr, A. Zakharov, C. Coletti, K. V. Emtsev, and U. Starke, *2D Mater.* **3**, 035003 (2016).
- [65] A. Yurtsever, J. Onoda, T. Iimori, K. Niki, T. Miyamachi, M. Abe, S. Mizuno, S. Tanaka, F. Komori, and Y. Sugimoto, *Small* **12**, 3956 (2016).
- [66] S. Chen, P. A. Thiel, E. H. Conrad, and M. C. Tringides, *Phys. Rev. Materials* **4** (2020).
- [67] Y. Sohn, S. W. Jung, F. Göhler, W. J. Shin, S. Cha, T. Seyller, and K. Kh, *J. Korean Phys. Soc.* **78**, 157 (2021).

## Bibliography

---

- [68] Y. Lin, S. Wolff, P. Schädlich, M. Hutter, S. Soubatch, T. Lee, F. S. Tautz, T. Seyller, C. Kumpf, and F. C. Bocquet, *Phys. Rev. B* **106** (2022).
- [69] S. Ichinokura, K. Sugawara, A. Takayama, T. Takahashi, and S. Hasegawa, *ACS Nano* **10**, 2761 (2016).
- [70] J. Sforzini, L. Nemec, T. Denig, B. Stadtmüller, T. Lee, C. Kumpf, S. Soubatch, U. Starke, P. Rinke, V. Blüm, et al., *Phys. Rev. Lett.* **114** (2015).
- [71] S. Hertel, D. Waldmann, J. Jobst, A. Albert, M. Albrecht, S. A. Reshanov, A. Schöner, M. Krieger, and H. B. Weber, *Nat. Commun.* **3** (2012).
- [72] S. Forti, K. V. Emtsev, C. Coletti, A. Zakharov, C. Riedl, and U. Starke, *Phys. Rev. B* **84** (2011).
- [73] F. C. Bocquet, R. Bisson, J. Themlin, J. M. Layet, and T. Angot, *Phys. Rev. B* **85** (2012).
- [74] Y. Murata, T. Cavallucci, V. Tozzini, N. Pavliček, L. Groß, G. Meyer, M. Takamura, H. Hibino, F. Beltram, and S. Heun, *Nano Res.* **11**, 864 (2017).
- [75] R. Balog, B. Jørgensen, J. W. Wells, E. Lægsgaard, P. Hofmann, F. Besenbacher, and L. Hornekær, *J. AM. CHEM. SOC.* **131**, 8744 (2009).
- [76] A. Bostwick, J. L. McChesney, K. V. Emtsev, T. Seyller, K. Horn, S. D. Kevan, and E. Rotenberg, *Phys. Rev. Lett.* **103** (2009).
- [77] C. Virojanadara, R. Yakimova, A. Zakharov, and L. I. Johansson, *J. Phys. D: Appl. Phys.* **43**, 374010 (2010).
- [78] J. Kunc, M. Rejhon, and P. Hlídek, *AIP Advances* **8** (2018).
- [79] I. Shtepliuk, I. G. Ivanov, T. Iakimov, R. Yakimova, A. Kakanakova-Georgieva, P. Fiorenza, and F. Giannazzo, *Mat. Sci. Semicon. Proc.* **96**, 145 (2019).
- [80] M. J. Szary, S. El-Ahmar, and T. Ciuk, *Appl. Surf. Sci.* **541**, 148668 (2021).
- [81] R. Sakakibara and W. Norimatsu, *Phys. Rev. B* **105** (2022).

- [82] S. Watcharinyanon, C. Virojanadara, J. Osiecki, A. Zakharov, R. Yakimova, R. I. G. Uhrberg, and L. I. Johansson, *Sur. Sci.* **605**, 1662 (2011).
- [83] B. Lee, S. Han, and Y. Kim, *Phys. Rev. B* **81** (2010).
- [84] A. Markevich, R. Jones, S. Öberg, M. Rayson, J. Goss, and P. Briddon, *Phys. Rev. B* **86** (2012).
- [85] C. Virojanadara, A. Zakharov, R. Yakimova, and L. I. Johansson, *Sur. Sci.* **604**, L4 (2010).
- [86] J. M. B. Lopes dos Santos, N. M. R. Peres, and A. H. Castro Neto, *Phys. Rev. Lett.* **99** (2007).
- [87] S. Shallcross, S. Sharma, E. Kandelaki, and O. A. Pankratov, *Phys. Rev. B* **81**, 165105 (2010).
- [88] R. Bistritzer and A. H. MacDonald, *Phys. Rev. B* **81**, 245412 (2010).
- [89] R. Bistritzer and A. H. MacDonald, *PNAS* **108**, 12233 (2011).
- [90] Y. Cao, J. Y. Luo, V. Fatemi, S. Fang, J. D. Sanchez-Yamagishi, K. Watanabe, T. Taniguchi, E. Kaxiras, and P. Jarillo-Herrero, *Phys. Rev. Lett.* **117**, 116804 (2016).
- [91] K. Kim, A. DaSilva, S. Huang, B. Fallahazad, S. Larentis, T. Taniguchi, K. Watanabe, B. J. LeRoy, A. H. MacDonald, and E. Tutuc, *PNAS* **114**, 3364 (2017).
- [92] L. Rademaker, I. V. Protopopov, and D. A. Abanin, *Phys. Rev. Res.* **2**, 033150 (2020).
- [93] S. Chen, M. He, Y. Zhang, V. Hsieh, Z. Fei, K. Watanabe, T. Taniguchi, D. Cobden, X. Xu, C. Dean, et al., *Nat. Phys.* **17**, 374 (2020).
- [94] P. J. Ledwith, G. Tarnopolsky, E. Khalaf, and A. Vishwanath, *Phys. Rev. Res.* **2**, 023237 (2020).
- [95] C. Repellin and T. Senthil, *Phys. Rev. Res.* **2**, 023238 (2020).

## Bibliography

---

- [96] E. S. Morell, J. Correa, P. Vargas, M. Pacheco, and Z. Barticevic, *Phys. Rev. B* **82** (2010).
- [97] Y. Cao, V. Fatemi, S. Fang, K. Watanabe, T. Taniguchi, E. Kaxiras, and P. Jarillo-Herrero, *Nature* **556**, 43 (2018).
- [98] W. Yao, E.-Y. Wang, C.-H. Bao, Y.-O. Zhang, K.-N. Zhang, K.-J. Bao, C.-K. Chan, C.-Y. Chen, J. Avila, M. C. Asensio, et al., *Proc Natl Acad Sci USA*. **115**, 6928–6933 (2018), ISSN 1091-6490.
- [99] X.-B. Lu, P. Stepanov, W. Yang, M. Xie, M. A. Aamir, I. Das, C. Urgell, K. Watanabe, T. Taniguchi, G.-Y. Zhang, et al., *Nature* **574**, 653–657 (2019), ISSN 1476-4687.
- [100] M. J. Park, Y. Kim, G. Y. Cho, and S. Lee, *Phys. Rev. Lett.* **123** (2019).
- [101] E. Codecido, Q. Wang, R. Koester, S. Che, H. Tian, R. Lv, S. Tran, K. Watanabe, T. Taniguchi, F. Zhang, et al., *Sci. Adv.* **5** (2019).
- [102] M. Yankowitz, S. Chen, H. Polshyn, Y. Zhang, K. Watanabe, T. Taniguchi, D. Graf, A. Young, and C. Dean, *Science* **363**, 1059 (2019).
- [103] P. Stampfli, *Helvetica Physica Acta* **59**, 1260 (1986).
- [104] S. J. Ahn, P. Moon, T. Kim, H. W. Kim, H. Shin, E. H. Kim, H. Cha, S. Kahng, P. Kim, M. Koshino, et al., *Science* **361**, 782 (2018).
- [105] P. Moon, M. Koshino, and Y. Son, *Phys. Rev. B* **99** (2019).
- [106] J. Halle, A. Mehler, and N. Néel, *Phys. Chem. Chem. Phys.* **21**, 3140 (2019).
- [107] A. Reina, S. Thiele, X. Jia, S. Bhaviripudi, M. S. Dresselhaus, J. Schaefer, and J. Kong, *Nano Res.* **2**, 509 (2009).
- [108] Z. Yan, Y. Liu, L. Ju, Z. Peng, J. Lin, G. Wang, H. Zhou, C. Xiang, E. L. G. Samuel, C. Kittrell, et al., *Angew. Chem. Int. Ed.* **53**, 1565 (2014).
- [109] Y.-N. Song, J.-N. Zhuang, M. Song, S.-Q. Yin, Y. Cheng, X.-W. Zhang, M. Wang, R. Xiang, Y. Xia, S. Maruyama, et al., *Nanoscale* **8**, 20001 (2016).
- [110] Y. Qian and D. J. Kang, *ACS Appl. Mater. Interfaces* **10**, 29069 (2018).

- [111] S. Pezzini, V. Mišeikis, G. Piccinini, S. Forti, S. Pace, R. Engelke, F. Rossella, K. Watanabe, T. Taniguchi, P. Kim, et al., *Nano Lett.* **20**, 3313 (2020).
- [112] Y. Takesaki, K. Kawahara, H. Hibino, S. Okada, M. Tsuji, and H. Ago, *Chem. Mater.* **28**, 4583 (2016).
- [113] Z. Gao, Q. Zhang, C. H. Naylor, Y. Kim, I. H. Abidi, J. Ping, P. Ducos, J. Zauberman, M. Zhao, A. M. Rappe, et al., *ACS Nano* **12**, 2275 (2018).
- [114] H. Y. Cho, Y. Park, S. Kim, T. Ahn, T. Kim, and H. C. Choi, *NPJ 2D Mater. and Appl.* **4** (2020).
- [115] P. Ma, A. Zhang, H. Zhen, Z. Jiang, Y. Yang, J. Ding, Z. Liu, J. Liu, D. Shen, Q. Yu, et al., *Chinese Phys. B* **33**, 066101 (2024).
- [116] K. Tahara and Y. Tobe, *Chem. Rev.* **106**, 5274 (2006).
- [117] R. Jasti, J. Bhattacharjee, J. B. Neaton, and C. R. Bertozzi, *J. AM. CHEM. SOC.* **130**, 17646 (2008).
- [118] H. Takaba, H. Omachi, Y. Yamamoto, J. Bouffard, and K. Itami, *Angew. Chem. Int. Ed.* **48**, 6112 (2009).
- [119] Y. Segawa, H. Omachi, and K. Itami, *Organic Lett.* **12**, 2262 (2010).
- [120] S. Yamago, Y. Watanabe, and T. Iwamoto, *Angew. Chem. Int. Ed.* **49**, 757 (2010).
- [121] T. Iwamoto, Y. Watanabe, Y. Sakamoto, T. Suzuki, and S. Yamago, *J. AM. CHEM. SOC.* **133**, 8354 (2011).
- [122] P. Evans, E. Darzi, and R. Jasti, *Nat. Chem.* **6**, 404–408 (2014).
- [123] Y.-M. Li, Y. Segawa, A. Yagi, and K. Itami, *J. AM. CHEM. SOC.* **142**, 12850 (2020).
- [124] Y.-X. Lv, J.-F. Lin, K. Song, X.-W. Song, H.-J. Zang, Y.-P. Zang, and D.-B. Zhu, *Sci. Adv.* **7**, eabk3095 (2021).
- [125] F. Bernt and H. A. Wegner, *Chem. Eur. J.* **29**, e202301001 (2023).

## Bibliography

---

- [126] Y. Narita, N. and Kurita, K. Osakada, T. Ide, H. Kawai, and Y. Tsuchido, *Nat. Commun.* **14** (2023).
- [127] T. Terabayashi, E. Kayahara, Y.-C. Zhang, Y. Mizuhata, N. Tokitoh, T. Nishinaga, T. Kato, and S. Yamago, *Angew. Chem. Int. Ed.* **62**, e202214960 (2023).
- [128] M. Fujitsuka, D. W. Cho, T. Iwamoto, S. Yamago, and T. Majima, *Phys. Chem. Chem. Phys.* **14**, 14585 (2012).
- [129] E. Bauer, *Science of Microscopy* pp. 605–656 (2007).
- [130] W. Chung and M. S. Altman, *Ultramicroscopy* **74**, 237 (1998).
- [131] H. Over, H. Huang, S. Y. Tong, W. C. Fan, and A. Ignatiev, *Phys. Rev. B* **48**, 15353 (1993).
- [132] H. Over, M. Gierer, H. Bludau, G. Ertl, and S. Y. Tong, *Sur. Sci.* **314**, 243 (1994).
- [133] A. K. Schmid, W. Swiech, C. Rastomjee, B. Rausenberger, W. Engel, E. Zeitler, and A. M. Bradshaw, *Sur. Sci.* **331-333**, 225 (1995).
- [134] J. I. Flege and E. E. Krasovskii, *Phys. Status Solidi RRL* **8**, 463 (2014).
- [135] M. Jugovac, T. O. Menteş, F. Genuzio, J. Lachnitt, V. Feyer, J. I. Flege, and A. Locatelli, *Appl. Surf. Sci.* **566**, 150656 (2021).
- [136] A. Kundu, L. Buß, and M. Ewert, *Frontiers in Physics* **9** (2021).
- [137] T. Ohta, F. E. Gabaly, A. Bostwick, J. L. McChesney, K. V. Emtsev, A. K. Schmid, T. Seyller, K. Horn, and E. Rotenberg, *New J. Phys.* **10**, 023034 (2008).
- [138] H. Hibino, H. Kageshima, F. Maeda, M. Nagase, Y. Kobayashi, and H. Yamaguchi, *Phys. Rev. B* **77** (2008).
- [139] T. A. De Jong, D. Kok, A. Van der Torren, H. Schopmans, R. Tromp, S. Van der Molen, and J. Jobst, *Ultramicroscopy* **213**, 112913 (2020), ISSN 0304-3991.

- [140] F. Masia, W. W. Langbein, S. Fischer, J. Krisponeit, and J. Falta, *Journal of Microscopy* **289**, 91 (2022).
- [141] F. Pedregosa, G. Varoquaux, A. Gramfort, V. Michel, B. Thirion, O. Grisel, M. Blondel, P. Prettenhofer, R. Weiss, V. Dubourg, et al., *JMLR* **12**, 2825 (2011).
- [142] S. J. Nanda, I. Gulati, R. Chauhan, R. Modi, and U. Dhaked, *Applied Artificial Intelligence* **33**, 152 (2018).
- [143] N. G. Duron, O. Gutierrez-Vargas, and S. C. Ake, *Mathematics* **9**, 879 (2021).
- [144] E. Nandapala and K. Jayasena, *ICIIS* pp. 344–349 (2020).
- [145] A. M. Ikotun, A. E. Ezugwu, L. Abualigah, B. Abuhaija, and H. Jia, *Information Sciences* **622**, 178 (2023).
- [146] P. Woodruff, Cambridge University Press (2016).
- [147] M. Chelvayohan and C. H. B. Mee, *J. Phys. C: Solid State Phys.* **15**, 2305 (1982).
- [148] G. G. Fuentes and M. Knupfer, *Appl. Phys. A* **84**, 329 (2006).
- [149] S. Duhm, A. Gerlach, I. Salzmann, B. Bröker, R. L. Johnson, F. Schreiber, and N. Koch, *Organic Electronics* **9**, 111 (2008).
- [150] J. Felter, J. Wolters, F. C. Bocquet, F. S. Tautz, and C. Kumpf, *J. Phys.: Condens. Matter* **31**, 114003 (2019).
- [151] A. Nakajima, H. Yokoya, Y. Furukawa, and H. Yonezu, *J. Appl. Phys.* **97**, 104919 (2005).
- [152] V. Borovikov and A. Zangwill, *Phys. Rev. B* **79**, 245413 (2009).
- [153] P. Mende, J. Li, and R. M. Feenstra, *Appl. Phys. Lett.* **113** (2018).
- [154] W. Jin and R. M. Osgood, *Adv. Phys. X* **4**, 1688187 (2019).
- [155] S. M. Butterfield, P. R. Patel, and M. L. Waters, *J. AM. CHEM. SOC.* **124**, 9751 (2002).



## Bibliography

---

- [156] E. C. Lee, D. Kim, P. Jurečka, P. Tarakeshwar, P. Hobza, and K. S. Kim, J. Phys. Chem. A **111**, 3446 (2007).
- [157] S. Grimme, Angew. Chem. Int. Ed. **47**, 3430 (2008).
- [158] J. Šponer, K. E. Riley, and P. Hobza, Phys. Chem. Chem. Phys. **10**, 2595 (2008).
- [159] T. Chen, M.-X. Li, and J.-Q. Liu, Cryst. Growth Des. **18**, 2765 (2018).
- [160] D. B. Ninković, J. P. Blagojević F, M. B. Hall, E. N. Brothers, and S. D. Zarić, ACS Cent. Sci. **6**, 420 (2020).

## List of Figures

- 1.1 LEED patterns obtained from a 6H-SiC(0001) surface with Si-rich (a)  $(3 \times 3)$  and (b)  $(\sqrt{3} \times \sqrt{3}) R30^\circ$  reconstruction. The LEED energy is 100 eV, and the diffraction spots of the substrate are marked by red circles. . . . . 8
- 1.2 (a) Schematic representation of the atomic arrangement in a carbon buffer layer (ZLG) on a 6H-SiC(0001) surface, adapted from an STM image with a bias voltage of 0.2 V [1]. The colored dots represent resolvable charge densities, which are considered to represent the atomic positions. The red dots that arrange in a diamond shape mark the clearest contrast, and are repeated only with  $(6\sqrt{3} \times 6\sqrt{3}) R30^\circ$  periodicity. (b) Measured LEED pattern from a ZLG graphene sample. The LEED energy is 100 eV. The unit cell vectors of the substrate SiC and epitaxial graphene are marked by black and red colored arrows, respectively. (c) Sketched side view model of the  $(6\sqrt{3} \times 6\sqrt{3}) R30^\circ$  reconstructed ZLG [2]. . . . . 9
- 1.3 (a) Measured and (b) Sketched LEED patterns of an epitaxial monolayer graphene sample. The LEED energy is 100 eV. The unit cell vectors of the substrate SiC and epitaxial graphene are marked by black and red colored arrows, respectively. In (b), the  $6\sqrt{3}$  grid is represented by hollow spots. The substrate SiC spots are highlighted with black color, G- $R30^\circ$  with red color, visible  $(6 \times 6)$  with green color, and visible  $6\sqrt{3}$  spots with blue color. (c) Sketched side view model of the epitaxial monolayer graphene [2]. . . . . 10

## List of Figures

---

1.4	Moiré pattern formed by overlapping and rotating two honeycomb lattices [3]. Highlighted in yellow are the repeating regions where the hexagons in the two sheets nearly align. . . . .	14
1.5	[6]-CPP, the shortest-possible subunit of a (6,6) CNT [4]. . . . .	19
1.6	Packing structure of [6]-CPPs in the crystalline state, which is condensed from a dichloromethane solution [4]. . . . .	20
1.7	Space-filling model for the herringbone-shaped packing of molecules, along with the side view of two inserted [6]-CPP molecules [5]. .	21
1.8	Polymerization of biphenylene ribbons (BPRs) with [6]-CPP molecules as precursors on a Cu(111) surface. STM images are from Prof. Dr. Gottfried's group, Marburg. . . . .	22
2.1	Elmitec AC-SPELEEM 3 in our lab. . . . .	24
2.2	Schematic representation of the pumping system of the AC-SPELEEM.	25
2.3	Schematic representation of electron optics of the AC-SPELEEM. The green and red lines represent the electron pathway. The electromagnetic lenses are depicted in blue convex icons. . . . .	26
2.4	Electron beam pathway in bright field mode (a) and dark field mode (b). Gray arrow represents the incident beams. Red, black and blue lines represent the pathway of diffracted electrons. . .	30
2.5	Schematic interpretation of the clustering principle of <i>K-means</i> .	32
2.6	Elbow method for determining the <i>K</i> value of <i>K-means</i> , in which WCSS with respect to the number of clusters <i>K</i> is plotted. . . . .	33
2.7	Construction of an Ewald sphere in reciprocal space. $\vec{b}_1$ is the translation vector of a 2D reciprocal lattice. Momentum transfer $q = \vec{K}'_{hk} - \vec{K}$ , with $\vec{K}'_{hk}$ the emerging wave vector, and $\vec{K}$ the incident wave vector. . . . .	36

3.1	Schematic interpretation of the sample preparation via the surfactant-mediated growth method [6]. . . . .	41
3.2	(a) BF-LEEM image captured from the low-T sample at the electron energy of 1.66 eV with a FoV of 30 $\mu\text{m}$ . (b) and (c) ARPES energy distribution maps (EDM) measured from the low-T sample along the $\bar{\Gamma}\bar{K}$ direction close to the $\bar{K}$ point of G- $R0^\circ$ and G- $R30^\circ$ , respectively. (d-f) Same as the (a-c) but for the high-T sample. The band intensity in (c) and (f) is enhanced by a factor of 15. . . . .	42
3.3	LEED pattern of the low-T sample, and corresponding bright-field (BF) LEEM image, labeled (00), and dark field (DF) LEEM images, labeled <i>a</i> , <i>c</i> , <i>e</i> , and <i>f</i> . The labels of the LEEM images correspond to the diffraction spots marked in the LEED pattern. All LEEM images were obtained at an electron energy (start energy) of 55 eV. . . .	44
3.4	(a) Bright-field (BF) LEEM image of the low-T sample, recorded at 2.5 eV. LEEM- <i>IV</i> data (0 to 5.9 eV) have been recorded for this surface area (300 $\times$ 250 pixels) pixel-by-pixel and analyzed using the <i>K-means</i> algorithm (with $K = 3$ ) described in the text. (b) False-color image representing the result of clustering the LEEM- <i>IV</i> data. (c-e) All LEEM- <i>IV</i> spectra belonging to each of the three clusters. Individual spectra are plotted with a transparency of 0.01. The white curves represent the average of all spectra in the respective cluster. (f) For clarity, the average curves from panels (c-e) are plotted in one diagram in their corresponding color. The dashed black line marks the energy at which the BF-LEEM image in panel (a) was recorded. . . . .	46

## List of Figures

---

- 3.5 (a) Bright-field (BF) LEEM image of the same area as shown in Fig. 3.4 (a), but recorded at 3.2 eV; at this start energy, the contrast between step edges and terraces is more pronounced. (b) Magnified part of the image in panel (a), marked by a white rectangle in (a), showing a vertical step edge. The image size is  $360 \times 300 \text{ nm}^2$  ( $12 \times 10$  pixels). The colored dots mark nine columns (each containing 10 pixels) oriented parallel to the step edge. Red and green bars at the bottom of the image indicate to which cluster the pixels in the corresponding column have been assigned in the *K-means* analysis; vertical dashed white lines mark the borders between cluster I (red) and II (green). (c) Averaged LEEM-*IV* intensities from the marked columns in panel (b). Neighboring spectra are vertically displaced by 0.3. The color coding corresponds to the colored dots in panel (b). . . . . 49
- 3.6 LEED pattern of the high-T sample, and corresponding bright-field (BF) LEEM image, labeled *(00)*, and dark field (DF) LEEM images, labeled *a* and *c*. The labels of the LEEM images correspond to the diffraction spots marked in the LEED pattern. All LEEM images were obtained at an electron energy (start energy) of 55 eV. . . . 52
- 3.7 (a) Bright-field (BF) LEEM image of the high-T sample ( $\approx 3.0 \times 2.5 \mu\text{m}^2$ ,  $300 \times 250$  pixels, 2.9 eV). The white rectangle marks the area that is magnified in Fig. 3.10. (b) All LEEM-*IV* spectra that were recorded on the surface area imaged in panel (a). The color coding in panel (b) is arbitrary. In Fig. 3.8, these LEEM-*IV* spectra are clustered. . . . . 54

3.8	Results of the clustering of LEEM- <i>IV</i> spectra recorded on the high-T sample for (a,c) the semi-automatic analysis based on the <i>K-means</i> algorithm, and (b,d) an analytic classification based on <i>a priori</i> defined criteria. For more details, see main text. (a,b) Clusters of spectra for six different classes, originating from graphene stacks consisting of one, two, three, four, five and more than five layers. Individual spectra are plotted with a transparency of 0.01. The white curves represent the average of all spectra in the respective cluster. (c,d) False-color images representing the result of clustering the LEEM- <i>IV</i> data. The corresponding bright-field (BF) LEEM image is shown in Fig. 3.7 (a). . . . .	56
3.9	Results of the clustering of LEEM- <i>IV</i> spectra of the high-T sample for the semi-automatic (black) and the analytic method of data analysis (gray). (a) Histogram of the LEEM intensity of the four-layer clusters at a start energy of 2.9 eV, as marked by red dashed lines in Fig. 3.8 (a) and (b). The bin size on the intensity axis was 0.03. The histogram was normalized to a total area of 1. In the dark gray area the histograms of both methods overlap. (b) Proportion of the different regions (1, 2, ..., 5 layers, more than 5 layers (flat) and unidentified) of the total surface area, according to Fig. 3.8 (c) and (d). . . . .	57
3.10	Results of the clustering (using the analytic approach) of LEEM- <i>IV</i> spectra recorded on the high-T sample: (a) Averaged spectra for each of the classes in Fig. 3.8 (b). (b) Magnification of the marked section (white rectangle) in the bright field (BF) LEEM image in Fig. 3.7 (a). (c) False-color image representing the result of the clustering of LEEM- <i>IV</i> spectra for the sample area shown in (b), also the magnified image of the region marked by a white rectangle in Fig. 3.8 (d). . . . .	58

## List of Figures

---

- 3.11 LEEM-*IV* spectra and false-color images of the "unidentified" regions found in the semi-automatic (*K-means*) analysis of the high-T sample (compare with Fig. 3.8). (a) All *IV* curves of the unidentified regions, plotted in gray with a transparency of 0.01. The unidentified regions can be divided in four clusters, as shown in (c-f), according to the shape of their *IV* curves. (b) Same as (a), but all curves plotted in their respective false-color as defined in (c-f). (g) and (h): Areas on the surface corresponding to unidentified regions, plotted as gray and false-colored areas, respectively. The shown surface area corresponds to Fig. 3.8 (c). . . . . 60
- 4.1 (a) LEEM image captured at 0.66 eV from the surface before intercalation. (b) LEED pattern obtained at an electron energy of 60 eV. (c) BF-LEEM image of a small area on the surface, recorded at 2.9 eV with a size  $\approx 3.0 \times 2.5 \mu\text{m}^2$  ( $300 \times 250$  pixels). LEEM-*IV* data in the energy range from  $-2$  to 10 eV have been recorded for the area and analyzed with the pixel-by-pixel method. (d) False-color presentation of the result of the LEEM-*IV* analysis. (e,f) Two curve clusters obtained through the pixel-by-pixel analysis. All curves are plotted with a transparency of 0.01, and the white curves in the middle represent the average of all spectra allocated to the respective cluster. Panel (b), and (c,f) share the same color codes. 65
- 4.2 BF-LEEM images, and LEED patterns measured from the sample surface at different stages of the hydrogen intercalation, with (a,b) being after 3 hours, (c,d) being after 6 hours, and (e,f) being after 10.5 hours. All BF-LEEM images were taken at an electron energy of 2.9 eV, and all LEED patterns of 60 eV. . . . . 67

4.3	(a) BF-LEEM image of a small area on the surface after 3 hours of intercalation, recorded at 2.9 eV with a size $\approx 3.0 \times 2.5 \mu\text{m}^2$ (300 $\times$ 250 pixels). LEEM- <i>IV</i> data in the energy range from $-2$ to 10 eV have been recorded for the area and analyzed with the pixel-by-pixel method. (b) False-color presentation of the result of the LEEM- <i>IV</i> analysis. (c-h) Six curve clusters obtained through the pixel-by-pixel analysis. All curves are plotted with a transparency of 0.01, and the white curves in the middle represent the average of all spectra allocated to the respective cluster. Panel (b), and (c-h) share the same color codes. . . . .	68
4.4	Same as Fig. 4.3, but after 6 hours of intercalation. Note that separate color codes were defined for each of the figures. . . . .	70
4.5	Same as Fig. 4.3 and Fig. 4.4, but after 10.5 hours of intercalation. Note that separate color codes were defined for each of the figures. . . . .	71
4.6	Dispersion of the $\pi$ band measured with ARPES below the Dirac point along with the $\bar{\Gamma}\bar{K}_{0^\circ}\bar{K}_{0^\circ}$ and the $\bar{\Gamma}\bar{K}_{30^\circ}\bar{K}_{30^\circ}$ directions for the Brillouin zone of hydrogen intercalated $30^\circ$ -TBG. . . . .	72
4.7	(a) BF-LEEM image of a small area on the surface after 4 hours of intercalation, recorded at 4.1 eV with a size $\approx 3.0 \times 2.5 \mu\text{m}^2$ (300 $\times$ 250 pixels). LEEM- <i>IV</i> data in the energy range from 0 to 7 eV have been recorded for the area and analyzed with the pixel-by-pixel method. (b) False-color presentation of the result of the LEEM- <i>IV</i> analysis. (c-e) Three curve clusters obtained through the pixel-by-pixel analysis. All curves are plotted with a transparency of 0.01, and the white curves in the middle represent the average of all spectra allocated to the respective cluster, and they are plotted in the same graph in (f). Panel (b), (c-e), and (f) share the same color codes. . . . .	74
4.8	$R_{Intensity}$ , defined as the ratio of the averaged intensity of "inter-bilayer" areas to that of "epi-bilayer" areas, with respect to the annealing temperature during the deintercalation process. . . . .	75



## List of Figures

---

- 4.9 (a-e) LEEM image sequence captured during the hydrogen deintercalation process in the temperature range from 800 °C to 850 °C. All the images are obtained at an electron energy of 2.3 eV, at which the "epi-bilayer" areas appear brighter than the "inter-bilayer" areas. All the LEEM images have the same brightness scale. (f) Pixel-intensity-profile plotted along with the colored lines in each LEEM image (a-e), and each colored curve corresponds to the same colored line in the LEEM images. . . . . 77
- 4.10 Same as Fig. 4.7, but after the deintercalation. (a) BF-LEEM image of the same area on the surface. (b) False-color presentation of the result of the LEEM-*IV* analysis. (c-e) Three curve clusters obtained through the pixel-by-pixel analysis. Panel (b), (c-e), and (f) share the same color codes. . . . . 78
- 5.1 LEEM images of the sample surface at different times during the molecule deposition. The label in the bottom-left corner of each panel is the time point with respect to opening of the shutter. . . 82
- 5.2 LEED patterns obtained right after the deposition. The label in the bottom-left corner of each panel are the kinetic energy of the electrons during the LEED measurement. . . . . 83
- 5.3 LEEM images captured during the annealing from -60 °C to RT. Sample temperature and kinetic energy of the electrons are given in the lower left of the images. . . . . 84
- 5.4 LEEM images of the surface taken (a) before and (b) after keeping the sample at 25 °C for three days. Both images are captured with an electron energy of 0.8 eV. The yellow curves in both images mark the same step edges. (c) LEED pattern taken with an electron energy of 14 eV at the end of the three days. . . . . 85

- 5.5 (a) to (f) LEEM images captured after keeping at RT for three days. The labels in the bottom-left corner of each panel give the temperature and relative time with respect to image (a). The colored arrows in (a) to (f) mark the same area in each panel, respectively. All the LEEM images were captured with an electron energy of 1 eV. 87
  
- 5.6 LEED patterns obtained from the surface with a coverage that is three times higher than that of the experiment shown in Fig. 5.4(b). LEED pattern (f) is obtained with an electron energy of 4 eV, but after the LEED measurement at 50 eV. . . . . 89
  
- 5.7 LEEM images of a surface area (a) right after deposition at a low temperature, and (b) after annealing to 180 °C. The bright circle in image (a) marks the area that was illuminated by the electron beam during the LEED measurement. Both images were captured with an electron energy of 0.8 eV. . . . . 89
  
- 5.8 LEED composite images of LEED patterns obtained at 4 eV and 50 eV. LEED patterns at 4 eV are colored in red, while those at 50 eV in green. (a) the color composite image of Fig. 5.6 (a) and (e). (b) and (c) composite images are made from the LEED measurements of other experiments. . . . . 91
  
- 5.9 (a) to (l) LEEM images captured during the annealing to 90 °C. The labels in the bottom-left corner of each panel give the temperature and relative time with respect to image (a). The colored arrows in (a) to (c) mark the same area in each panel, respectively. All the LEEM images were captured with an electron energy of 0.8 eV. . 92
  
- 5.10 (a) to (e) LEEM images captured when the sample was cooled at around -20 °C. The labels in the bottom-left corner of each panel give the temperature and relative time with respect to image (a). The colored arrows in (a) to (e) mark the same area in each panel, respectively. All the LEEM images were captured with an electron energy of 0.8 eV. (f) LEED pattern obtained from the surface, and it was obtained with an electron energy of 10 eV. . . . . 93

## List of Figures

---

- 5.11 (a) to (h) LEEM images captured during the annealing to 180 °C. The labels in the bottom-left corner of each panel give the temperature and relative time with respect to image (a). All the LEEM images were captured with an electron energy of 1 eV. (i) LEED pattern obtained after cooling down to RT with an electron energy of 10 eV. . . . . 94



## Acknowledgements

There are many people I would like to thank for their help during my PhD study and their contribution to this work.

First, I would like to express my great gratitude to Prof. Dr. Christian Kumpf, who supervised and encouraged my work throughout both my Master's and PhD studies. His patience and continuous guidance over the past years have always made me feel supported and reassured.

Dr. François C. Bocquet directly supervised me on several projects, and I could always count on his advice and solutions for the challenges I faced. I wouldn't have been able to complete these projects so quickly without his help. Thank you, François!

I would like to acknowledge Prof. Dr. Joachim Mayer for taking the time to be my second supervisor and for co-refereeing my thesis.

My thanks also go to Miriam Rath for her supervision during my Master's studies. My knowledge and skills in UHV and LEEM techniques stem from her hands-on teaching and daily guidance. She particularly helped me develop a habit of approaching problems rigorously. Thanks to her support, I have grown significantly both academically and personally.

## Acknowledgements

---

I thank Mark Hutter for his assistance with our collaborative project and for his friendship. There were many hard and discouraging times when I hit bottlenecks in my work, and he was always there to listen to my complaints and offer help.

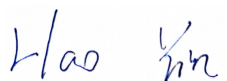
I acknowledge Prof. Dr. Michael Gottfried and his student, Dr. Qitang Fan, for providing us with experimental topics and molecules.

I am also grateful to all my colleagues at the Peter Grünberg Institute (PGI-3), Forschungszentrum Jülich, for creating such a friendly and warm atmosphere at the institute.

I am grateful for the silent dedication and support of my parents and family.

To my friends who have accompanied me over the past three years: people come and go, but I cherish our encounters and warmly wish you well.

Finally, I would like to express my appreciation for the financial support from the Peter Grünberg Institute (PGI-3) and for the funding provided by the DFG through the SFB 1083 project.

A handwritten signature in blue ink, appearing to read 'Hao Yin'.

*July 10, 2025*

*Jülich*



Name Hao Yin

Birthday 21/07/1995

Wiesenstraße.5a 52428, Jülich

+(86) 15689138010 / +(49) 15236648265

h.yin@fz-juelich.de

hao.yin@rwth-aachen.de



## Education

07.2021 -- now	Forschungszentrum Jülich Ph.D. Studies
01.2019 -- 04.2021	Forschungszentrum Jülich Project's and Master's Thesis
04.2018 -- 04.2021	RWTH Aachen University Master Studies
07.2017 -- 03.2018	Alapos Language School, Berlin
10.2013 -- 06.2017	China University of Petroleum (Huadong) Bachelor Studies
10.2010 -- 06.2013	The First High Middle School of Guangrao
10.2001 -- 06.2010	The Central School of Xiliuqiao



## Internship

07.2016 -- 08.2016	Qingdao Quanchen Advertising Media Co., Ltd Job Content: Welding of Billboard
08.2015 -- 09.2015	Weichai Power Co., Ltd Mechanical Hot-working Practice
07.2014 -- 09.2014	Shtar Science & Technology Group Metalworking Practice



## Others Knowledge

Software Categories:	CAD, Solidworks, Image J, Photoshop, Gwyddion, Python, and C/C++ Language
Certificates:	Intermediate Welder Certificate, Boshen Scholarship Certificate
Languages:	English fluently read, write and speak German DSH-2 Chinese native language



Band / Volume 102

**Analysis and quantitative comparison of neural network dynamics on a neuron-wise and population level**

R. Gutzen (2024), xii, 252 pp

ISBN: 978-3-95806-738-7

Band / Volume 103

**3D Scaffolds with Integrated Electrodes for Neuronal Cell Culture**

J. Abu Shihada (2024), vii, 163 pp

ISBN: 978-3-95806-756-1

Band / Volume 104

**Advances in Photoemission Orbital Tomography**

A. Haags (2024), ix, 254 pp

ISBN: 978-3-95806-766-0

Band / Volume 105

**Quantitative investigation of point defects and their dynamics in focused ion beam-prepared group III-nitride lamellas by off-axis electron holography**

K. Ji (2024), 164 pp

ISBN: 978-3-95806-782-0

Band / Volume 106

**NeuCoNS and Stacked-Net: Facilitating the Communication for Accelerated Neuroscientific Simulations**

R. Kleijnen (2024), xx, 110, xxi-xxxiv pp

ISBN: 978-3-95806-788-2

Band / Volume 107

**Construction of a Spiking Network Model of Macaque Primary Visual Cortex: Towards Digital Twins**

A. Kurth (2024), xvi, 207 pp

ISBN: 978-3-95806-800-1

Band / Volume 108

**Spin selectivity of chiral molecules on surfaces**

M.R. Safari (2025), xiv, 165 pp

ISBN: 978-3-95806-810-0

Band / Volume 109

**Redox-based Random Access Memory Arrays for Computing-In-Memory and Neuromorphic Computing**

H. Chen (2025), x, 154 pp

ISBN: 978-3-95806-814-8



Band / Volume 110

**Mechanics of deep neural networks beyond the Gaussian limit**

K. Fischer (2025), xvi, 138 pp

ISBN: 978-3-95806-815-5

Band / Volume 111

**Characteristics of plastically deformed *fcc* and *bcc* High-Entropy Alloys**

T. Meenen (2025), x, 115 pp

ISBN: 978-3-95806-820-9

Band / Volume 112

**Software-Configurable Analog-To-Digital Converters for Configurable Pulse Detection**

L. Krystofiak (2025), xvii, 113 pp, xxix

ISBN: 978-3-95806-826-1

Band / Volume 113

**Development of Superparamagnetic Based Biological Sensor for the Detection of Brucella DNA Using Frequency Mixing Magnetic Detection**

A. Abuawad (2025), X, 129 pp

ISBN: 978-3-95806-836-0

Band / Volume 114

**A System for the Cryogenic Power Management of Quantum Computing Electronics: Development, Integration, and Test**

A. R. Cabrera Galicia (2025), xxv, 110, lviii pp

ISBN: 978-3-95806-844-5

Band / Volume 115

**Investigation of 2D Materials using Low Energy Electron Microscopy (LEEM)**

H. Yin (2025), viii, 137 pp

ISBN: 978-3-95806-848-3

Weitere **Schriften des Verlags im Forschungszentrum Jülich** unter  
<http://www.zb1.fz-juelich.de/verlagextern1/index.asp>



Information  
Band / Volume 115  
ISBN 978-3-95806-848-3